


# **SAF for Land Surface Analysis (LSA SAF)**

## **VALIDATION REPORT FRP**

Reference Number:	SAF/LAND/IM/VR_FRP/V_10
Issue/Revision Index:	Issue I/2010
FRP Pixel Algorithm Version:	1.4
FRP Grid Algorithm Version:	0.4
Last Change:	19/03/2010

<div>በፋይናንስ ዘመናዊ ፍጥነት ፍጥነት</div> <div> <b>LSA SAF</b> Investment Bank</div>	Land SAF VR-LST	Doc: SAF/LAND/IM/VR_FRP/V_10 Issue: Version I/2010 Date: 19/03/2010
--	-----------------	---


	Land SAF VR-LST	Doc: SAF/LAND/IM/VR_FRP/V_10 Issue: Version I/2010 Date: 19/03/2010
---	-----------------	---

## DOCUMENT SIGNATURE TABLE

	Name	Date	Signature
<b>Prepared by :</b>	Land SAF Project Team		
<b>Approved by :</b>	Land SAF Project Manager (IM)		

## DOCUMENTATION CHANGE RECORD

Issue / Revision	Date	Release	Description:
Version I/2008	25/03/2008	0.8	Version to be presented to ORR3
Version II/2008	20/05/2008	0.9	Version containing the modifications requested by ORR3.
Version III/2009	20/06/2009	1.1	Version containing the modifications requested by ORR3 and additional validation of FRP Pixel v1.1 product
Version IV/2009	14/09/2009	1.3	Version referring to the FRP Pixel v1.3 product
Version V/2009	18/10/2009	1.4	Version incorporating updates to FRP_Grid 0.4
Version I/2010	19/03/2010	1.4	Version containing the modifications requested by LSA 32 FRP Grid ORR.

	Land SAF VR-LST	Doc: SAF/LAND/IM/VR_FRP/V_10 Issue: Version I/2010 Date: 19/03/2010
---	-----------------	---

## DISTRIBUTION LIST

Internal Consortium Distribution		
Organisation	Name	No. Copies
IM	Pedro Viterbo	
IM	Luís Pessanha	
IM	Isabel Trigo	
IDL	Carlos da Camara	
IM	Isabel Monteiro	
IM	Sandra Coelho	
IM	Carla Barroso	
IM	Pedro Diegues	
IM	Teresa Calado	
IM	Benvinda Barbosa	
IM	Ana Veloso	
IMK	Folke-S. Olesen	
IMK	Frank Goettsche	
IMK	Ewa Kabsch	
MF	Jean-Louis Roujean	
MF	Olivier Hautecoeu	
MF	Dominique Carrer	
RMI	Françoise Meulenberghs	
RMI	Arboleda Alirio	
RMI	Nicolas Ghilain	
FMI	Niilo Siljamo	
UV	Joaquin Melia	
UV	F. Javier García Haro	
UV/EOLAB	Fernando Camacho	
UV	Aleixander Verger	

	Land SAF VR-LST	Doc: SAF/LAND/IM/VR_FRP/V_10 Issue: Version I/2010 Date: 19/03/2010
---	-----------------	---

External Distribution		
Organisation	Name	No. Copies
EUMETSAT	Frédéric Gasiglia	
EUMETSAT	Dominique Faucher	
EUMETSAT	Lorenzo Sarlo	
EUMETSAT	Lothar Schueller	
EDISOFT	Teresa Cardoso	
EDISOFT	Carlos Vicente	
EDISOFT	Cleber Balan	
SKYSOFT	Rui Alves	
SKYSOFT	João Canário	

	Land SAF VR-LST	Doc: SAF/LAND/IM/VR_FRP/V_10 Issue: Version I/2010 Date: 19/03/2010
---	-----------------	---

Steering Group Distribution		
Nominated by:	Name	No. Copies
IM	Carlos Direitinho Tavares	
EUMETSAT	Lorenzo Sarlo	
EUMETSAT	Yves Govaerts	
EUMETSAT	François Montagner	
STG/AFG (USAM)	Luigi de Leonibus	
MF	François Bouyssel	
RMI	Alexandre Joukoff	
FMI	Tapio Tuomi	



## List of Acronyms

ASTER	Advanced Spaceborne Thermal Emission and Reflection Radiometer
ATBD	Algorithm Theoretical Basis Document
CASA	Carnegie-Ames-Stanford Approach
CPTEC	Centro de Previsão de Tempo e Estudos Climáticos
ECMWF	European Centre for Medium-range Weather Forecasts
EUMETSAT	European Organisation for the Exploitation of Meteorological Satellites
FAS	Fire Assimilation System (at FMI)
FIR	Finitive impulse response
FMI	Finnish Meteorological Institute
HRV	High Resolution Visible
FRE	Fire Radiative Energy
FREEVAL	Fire Radiative Energy Evaluation
FRP	Fire Radiative Power
FTA	Fire Thermal Anomaly
GAS	GMES Atmospheric Service
GCM	Global Circulation Model
GEMS	Global and regional Earth-system (Atmosphere) Monitoring using Satellite and in-situ data (EU 6 <sup>th</sup> framework Integrated Project)
GMES	Global Monitoring for Environmental Security, European initiative for the implementation of information services dealing with environment and security
GFED	Global Fire Emissions Database (GFED) (van der Werf et al. 2006)
IFS	Integrated Forecast System
INPE	Instituto Nacional de Pesquisas Espaciais
KCL	King's College London
NRT	Near Real Time
MACC	Monitoring of Atmospheric Composition and Climate
MIR	Middle InfraRed
MODIS	Moderate Resolution Imaging Spectroradiometer
MOPITT	Measurements of Pollution in the Troposphere
MPEF	Meteorological Product Extraction Facility at EUMETSAT
NOAA	National Oceanic and Atmospheric Administration
ORR	Operation Readiness Review
PM	Particulate Matter
RAO	Research Announcement of Opportunity
SAF	Satellite Applications Facility
SEVIRI	Spinning Enhanced Visible and InfraRed Imager
TA	Thermal Anomaly [K]
TIR	Thermal InfraRed

## Table of Contents

<b>EXECUTIVE SUMMARY .....</b>	<b>15</b>
<b>1 INTRODUCTION.....</b>	<b>18</b>
1.1 FRP PRODUCT BACKGROUND .....	18
1.2 DOCUMENT STRUCTURE .....	19
1.3 FRP PRODUCT CONCEPT .....	19
1.4 THEORY OF THE FRP ALGORITHM .....	21
1.5 FACTORS LIMITING FRP PRODUCT ACCURACY .....	23
1.6 VALIDATION STRATEGY .....	27
<b>2 FRP REQUIREMENT DEFINITION .....</b>	<b>31</b>
2.1 IDENTIFICATION OF POTENTIAL OPERATIONAL USERS .....	31
2.1.1 Chemical Weather Forecasting/Monitoring .....	31
2.1.2 Validation of Prognostic Fire Models and Visibility Forecasts .....	31
2.1.3 Public Information and Safety Aspects .....	33
2.1.4 Scientific Studies .....	33
2.2 REQUIREMENTS ANALYSIS .....	35
2.3 REQUIREMENT SUMMARY .....	37
<b>3 VALIDATION DATASET DESCRIPTION .....</b>	<b>39</b>
3.1 THE MODIS MOD14 DATA SET .....	39
3.2 DATASET USED TO INVESTIGATE ALGORITHM ASSUMPTIONS .....	41
3.3 DATASET USED TO INVESTIGATE PER-FIRE COMPARISONS .....	41
3.4 DATASET USED TO INVESTIGATE EFFECTS OF SPATIAL RESOLUTION .....	41
3.5 DATASET USED TO INVESTIGATE EFFECT OF SEVIRI SENSOR CHARACTERISTICS AND LEVEL 1 TO 1.5 PRE-PROCESSING OPERATIONS.....	42
3.6 DATASETS USED IN IMPACT STUDIES .....	43
3.6.1 Global Fire Emissions Database (GFED).....	43
3.6.2 Global GEMS Model .....	44
3.6.3 SILAM Dispersion Model and Fire Assimilation System at FMI.....	44
3.6.4 MOPITT Atmospheric Carbon Monoxide Concentration Data .....	45
<b>4 SPECIFIC VALIDATION METHODOLOGY .....</b>	<b>46</b>
4.1 ALGORITHM PERFORMANCE ANALYSIS .....	46
4.2 SEVIRI PRODUCT PERFORMANCE ANALYSIS .....	47
4.2.1 Per-Fire Comparisons .....	47
4.2.2 Effect of Spatial Resolution - Area Based Comparisons.....	48
4.2.3 Analysis of Ecosystem-Specific Biases.....	57
4.2.4 Effects of Viewing Geometry.....	58
4.2.5 Effects of Saturation.....	58
4.2.6 Effects of SEVIRI sensor characteristics and Level 1.0 to 1.5 pre-processing operations .....	58
4.3 LANDSAF PRODUCT VALIDATIONS .....	59
4.3.1 Comparison to KCL product.....	59
4.3.2 Comparison to MODIS .....	59
4.4 VALIDATION BASED ON IMPACT STUDIES .....	59
4.4.1 Impacts of Temporal Resolution .....	59
4.4.2 Impact of FRP versus Hot Spot Detection .....	61
4.4.3 Impact on Estimating Fire Emissions .....	61
4.4.4 End-to-end Use (Greek Fires Case Study).....	62
<b>5 VALIDATION RESULTS.....</b>	<b>63</b>



 	Land SAF VR-LST	Doc: SAF/LAND/IM/VR_FRP/V_10 Issue: Version I/2010 Date: 19/03/2010
---	-----------------	---

5.1	RESULTS OF THE ALGORITHM PERFORMANCE ANALYSIS.....	63
5.2	RESULTS OF THE SEVIRI PRODUCT PERFORMANCE ANALYSIS .....	75
5.2.1	<i>Per-Fire Comparisons</i> .....	75
5.2.2	<i>Effect of Spatial Resolution – Area Based Comparisons</i> .....	85
5.2.3	<i>Analysis of Ecosystem-Specific Biases</i> .....	98
5.2.4	<i>Effects of Viewing Geometry</i> .....	99
5.2.5	<i>Effects of Saturation</i> .....	100
5.2.6	<i>Effect of SEVIRI Image Processing Chain</i> .....	101
5.3	RESULTS OF LAND SAF PRODUCT VALIDATIONS.....	108
5.3.1	<i>Comparison to KCL Product</i> .....	108
5.3.2	<i>Comparison to MODIS</i> .....	109
5.4	RESULTS OF VALIDATION BASED ON THE IMPACT STUDIES .....	113
5.4.1	<i>Impacts of Temporal Resolution-Study of Sensitivity to Temporal Resolution of Emissions: Global Carbon Dioxide Modelling of 2004</i> .....	114
5.4.2	<i>Impact on Estimating Fire Emissions</i> .....	119
5.4.3	<i>End-to-end Use Case Study: Modelling the Greece Fire Plumes of August 2007</i> .....	121
5.5	Analysis of Error Budget in LSA SAF FRP Pixel Product .....	128
<b>6</b>	<b>CONCLUSIONS .....</b>	<b>131</b>
6.1	PRODUCT VALIDATION SUMMARY .....	131
6.2	DEMONSTRATED USEFULNESS OF PRODUCT .....	132
6.3	DEFINITION OF ACCURACY REQUIREMENTS.....	133
	<b>APPENDIX 1 – IMPACT OF EUMETSAT RADIANCE DEFINITION CHANGE.....</b>	<b>135</b>
	<b>ACKNOWLEDGMENTS .....</b>	<b>137</b>
	<b>REFERENCES .....</b>	<b>138</b>

## List of Figures

### SECTION 1 (PAGES 15 – 31)

Figure 0.1: SEVIRI Imagery of southern Africa on 4 September 2003, in which numerous active fires are burning.

### SECTION 2 (PAGES 31 – 39)

Figure 0.2: Example of a comparison of the correlation of monthly burned area derived from the fire model Had\_FIRE (using HadCM3 or ERA 40 climate data) with burned area derived from the GFED (Guido van der Werf et al. 2006) and from SEVIRI (FREEVAL).

Figure 0.3: Differences in FRP for fires related to flashover events and those that pass within 10 km of the transmission line but which do not result in a flashover.

Figure 0.4: Estimates of SEVIRI FRP-derived biomass combustion as compared to the pre-burn fuel load for eighteen fires in southern African grasslands and woodlands.

### SECTION 3 (PAGES 39 – 46)

Figure 0.5: Estimated detection probabilities of a 1 km MODIS active fire pixel, calculated as a function of the number of 30 m ASTER active fire pixels it contains, and the spatial distribution of those ASTER active fire pixels (as expressed by Moran's I). Taken from Morisette et al. (2005).

### SECTION 4 (PAGES 46 – 63)

Figure 0.6: Estimated FRP range detectable for various fire temperatures using SEVIRI at the sub-satellite point.

Figure 0.7: Frequency-magnitude of per-pixel FRP derived from SEVIRI active fire detections, binned into 10 MW intervals.

Figure 0.8: Temporal profile of FRP measured by SEVIRI and MODIS over two consecutive days.

Figure 0.9: Frequency-magnitude distributions for all contemporaneous SEVIRI and MODIS fire pixels detected across Africa in Feb 2004-Jan 2005 (i.e. the training dataset discussed herein).

Figure 4.5: Graphical representation of the procedure used to generate the 2008 training and validation datasets. Fire pixels were subset from the “MOD14” and “MYD14” fire products between May 2008 and April 2009 using six 5.0° grid cells centred on the MODIS swath, as illustrated in (a).

Figure 4.6: SEVIRI-to-MODIS ratios of FRP plotted as a function of the hourly average of FRP measured by SEVIRI in 5.0° grid cells in both the NAfr and SAfr regions.

### SECTION 5 (PAGES 63 – 131)

Figure 0.10: Ratio (R) between the Fire Radiative Power estimate derived from MIR radiance method ( $FRP_{MIR}$ ), and the true FRP derived from the Stefan-Boltzmann Law ( $FRP_{TRUE}$ ).

*Figure 0.11: Fire emitter temperatures retrieved from analysis of Airborne Visible Infrared Imaging Spectrometer (AVIRIS) hyperspectral data of the 2003 Simi Fire in Southern California, USA by Dennison et al. (2006).*

*Figure 0.12: Departure of estimated FRP from true FRP for blackbody fires of temperature 650, 800 and 1000 K and fractional areas 0.1 to 0.0001 (denoted by the labels) as a function of the level of disagreement between the assumed background radiance signal and its true value (i.e. the value expressed by  $L_{\text{error},\text{MIR}}$  in Equation ).*

*Figure 0.13: As Figure 5.3. but now expressing the departure of the estimated FRP from the true FRP for blackbody fires of temperature 800 K and fractional areas 0.1 to 0.0001 (denoted by the labels) as a function of the level of disagreement between the assumed background radiance signal and its true value (i.e. the value expressed by  $L_{\text{error},\text{MIR}}$  in Equation ) and for different errors in the assumed MIR atmospheric transmission.*

*Figure 0.14: The central pixel brightness temperature of a 5×5 pixel window plotted over the full 24 hr cycle for southern Africa locations.*

*Figure 0.15: The x-axis reports the recorded FRP estimated by SEVIRI, whilst the y-axis reports the potential range of true FRP that could have given rise to that SEVIRI-derived FRP estimate.*

*Figure 0.16: Percentage uncertainty in FRP for 2000 observed fire pixels across southern Africa.*

*Figure 0.17: Effect of the inability of SEVIRI to detect low FRP fire pixels that MODIS can detect, illustrated by SEVIRI and MODIS fire detections collected over Central African Republic and surroundings in February 1-14 2004.*


*Figure 5.9: Results of the proximity analyses performed on the full (circle) and contemporaneous (square) datasets containing fire pixels detected in the region of CAR between 01 and 13 Feb 2004.*

*Figure 5.10: Results of the temporal analysis performed using the collocated SEVIRI and MODIS fire pixels detected in the region of CAR between 01 and 13 Feb 2004. Figure 0.11: Frequency distribution of SEVIRI fire pixel detection confidence for all falsely detected fire pixels in February, May and August 2004, as compared to that of all fire pixels.*

*Figure 0.12: Two examples where MODIS fire detection appears less sensitive than that of SEVIRI.*

*Figure 0.13: A comparison of per-fire FRP derived from SEVIRI and MODIS observations of 289 fires observed near-simultaneously by each sensor in February, May and August 2004.*

*Figure 0.14: Relationship between regional-scale inter-scene FRP derived from all spatially matched, contemporaneous SEVIRI and MODIS observations for, from top left clockwise, February, May, and August 2004.*

 <b>LSA SAF</b> Land Surface Analysis Satellite Application Facility	Land SAF VR-FRP	Doc: SAF/LAND/IM/VR_FRP/V_09 Issue: Version V/2009 Date: 18/10/2009
---	-----------------	---

*Figure 0.15: Temporal profiles in the ratios between SEVIRI and MODIS of fire pixel count and FRP.*

*Figure 0.16: Ratios of SEVIRI to MODIS FRP, as a function of the FRP measured by SEVIRI and MODIS.*

*Figure 0.17: Yearly sum of  $FRP_{SEVIRI}$  at  $1^\circ$  grid cell resolution and yearly ratios of  $FRP_{SEVIRI}$  to  $FRP_{MODIS}$  evaluated at  $5.0$ ,  $1.0$  and  $0.25^\circ$  grid cell resolutions.*

*Figure 5.18: Relationship between the FRP measured by SEVIRI and MODIS for the southern hemisphere of Africa.*

*Figure 5.19: Training relationships between the FRP measured by SEVIRI and MODIS for all four LSA SAF regions.*

*Figure 5.20: Performance of the WLS estimates during the validation exercise. The FRP measured by SEVIRI was adjusted using the WLS coefficients for each region to provide the predicted FRP potentially measured by MODIS.*

*Figure 5.21: Performance of the WLS models at the weekly/regional scale. In all four LSA SAF regions the predicted sum of FRP underestimates the measured sum of FRP.*

*Figure 0.22: GLC 2000 land cover classification and relative frequency of fire detection in each land cover type for MODIS and SEVIRI data.*

*Figure 0.23. Data from the SEVIRI ‘special operations mode’ experiment conducted on 4 September 2007, when the Meteosat 8 SEVIRI instrument was put into low-gain mode.*

*Figure 0.24. Data from the SEVIRI ‘special operations mode’ experiment conducted on 4 September 2007, when the FIR filter was removed from the Meteosat 8 SEVIRI instrument but kept on the Meteosat 9 SEVIRI instrument that observed the same area almost simultaneously. The figure shows the MIR brightness temperatures recorded over the same fire by both*


*Figure 0.25. The major steps involved in simulating SEVIRI active fire observations using a spatially invariant background temperature of 300 K.*

*Figure 0.26: The SEVIRI point spread function (E-W) and the finite impulse response filter, together with a SEVIRI observation of an active fire modelled with these as compared to a real SEVIRI active fire observation.*

*Figure 0.27: The effect of the SEVIRI observation process on the retrieval of FRP for fires of different effective temperatures and pixel proportions.*

*Figure 0.28: Simulated SEVIRI active fire TIR and MIR channel data, derived from higher spatial BIRD imagery to provide the ambient background measurements, and with a modelled fire spectral radiance signal superimposed.*

*Figure 0.29: Degree of underestimation induced by the SEVIRI observation process on simulated fires of the sort depicted in Figure 5.28 and which have been modelled with a*

	Land SAF VR-FRP	Doc: SAF/LAND/IM/VR_FRP/V_09 Issue: Version V/2009 Date: 18/10/2009
---	-----------------	---

*varying ambient background temperature (taken from BIRD imagery) and a spatially invariant ‘flat’ background temperature.*

*Figure 0.30. Comparison of Meteosat-8 and Meteosat-9 per-scene FRP data recorded simultaneously over southern Africa during the Meteosat-8 ‘special operations mode’ experiment.*

*Figure 0.31: FRP comparison between the Land SAF FRP product and that generated at KCL from EUMETCAST-received SEVIRI data of the same imaging slots.*

*Figure 0.32: A comparison of per-fire FRP derived from SEVIRI and MODIS observations of fires observed near-simultaneously by each sensor for a one week duration in each LSA SAF region.*

*Figure 0.33: Relationship between regional-scale inter-scene FRP derived from all spatially matched, contemporaneous SEVIRI and MODIS observations for the North African region 1-7 December 2009, where the MODIS swath is taken as the observation area and the Land SAF per-pixel FRP product was used as the SEVIRI record.*

*Figure 0.34: Location of all SEVIRI fire detections in Europe between 9 and 17 August 2008 – coloured red in this rendition and derived from the LSA SAF FRP Product*

*Figure 0.35: Total column CO<sub>2</sub> for simulation without (top) and with (bottom) fire emissions.*

*Figure 0.36: Fire emission contribution to total column CO<sub>2</sub> for emission with 1-hour (top) and 8-days (bottom) emission time resolution.*

*Figure 0.37: Differences in fire contribution to total column CO<sub>2</sub> for emissions with different time resolutions: 1h - 8d (top), 1d - 8d (middle), 1h - 1d (bottom).*

*Figure 0.38: Vertical distribution of difference in fire contribution to the CO<sub>2</sub> mixing ratio for emissions with different time resolutions of 1-hour and 8-days.*


*Figure 0.39: Relative difference of total column CO<sub>2</sub> for different time resolutions. (1-hourly – 8-daily fires [ppm]) / (1-hourly – no fires + 1 ppm).*

*Figure 0.40: Comparison of monthly SEVIRI based carbon emissions with Global Fire Emissions Database (GFED) versions 2 and preliminary version 3 for Africa north of the equator (top panel) and Africa south of the equator (bottom panel).*

*Figure 0.41: Annual variation of mean monthly MOPITT CO mixing ratios retrieved for five pressure levels over land between February 2004 and January 2005 in comparison to total FRP (left) and mean per-pixel FRP (right) for southern hemisphere Africa.*

*Figure 0.42: Number of active fires (hotspots) detected by MODIS (left) and by SEVIRI (right) on August 25, 2007 over the Mediterranean region.*

*Figure 0.43: Modelled organic matter plus black carbon AOD [-] (left, blue) and MODIS visual images (right) for an Aqua overpass on 25 August, 1205UTC, (top) and a Terra*

	Land SAF VR-FRP	Doc: SAF/LAND/IM/VR_FRP/V_09 Issue: Version V/2009 Date: 18/10/2009
---	-----------------	---

*overpass on 26 August, 0935UTC (bottom). Overlaid with SEVIRI FRP [W/m<sup>2</sup>] interpolated to model resolution (left, orange) and MODIS hot spots in (right, red).*

*Figure 0.44: Modelled smoke AOD [-] (left) and observed MODIS AOD [-] product (right) for Aqua overpasses on 25 August, 1205UTC (top). AOD scatter plots for the entire are and a box on the fire Greek plume (bottom).*

*Figure 0.45: Modelled smoke AOD [-] (left) and observed MODIS AOD [-] product (right) for Aqua overpasses on 26 August, 1110UTC (top). AOD scatter plots for the entire are and a box on the fire Greek plume (bottom).*

*Figure 0.46: Modelled smoke AOD [-] (left) and observed MODIS AOD [-] product (right) for Aqua overpasses on 27 August, 1155UTC (top). AOD scatter plots for the entire are and a box on the fire Greek plume (bottom).*



*Figure 0.47: Modelled organic matter plus black carbon AOD [-] (bluish) on 30 August 2007, 1430UTC, overlaid with observed SEVIRI FRP [W/m<sup>2</sup>] interpolated to model resolution (reddish). The University of Lecce AERONET station is indicated by a white circle.*

*Figure 0.48: Observed and modelled AOD time series over Lecce, Southern Italy.*

*Figure 0.49: Frequency distribution of FRP uncertainty contributions for all fire pixels identified in the North African LSA SAF region, 1-8 December 2009.*

*Figure 5.50: Temporal variation of the mean and mean $\pm$ standard deviation of the four individual components of the error budget discussed in Section 3.7 of the product ATBD are shown, along with the total.*



 	Land SAF VR-FRP	Doc: SAF/LAND/IM/VR_FRP/V_09 Issue: Version V/2009 Date: 18/10/2009
---	-----------------	---

## Executive Summary



It has been demonstrated in small-scale experiments that the amount of radiant energy liberated per unit time during a vegetation fire (the so-called Fire Radiative Power) is related to the rate at which the fuel biomass is being consumed (e.g. Wooster et al., 2005). This is a direct result of the combustion process, whereby carbon-based fuel is oxidised (burnt) with the release of a certain ‘heat yield’. Measuring this FRP and integrating it over the lifetime of the fire therefore provides a measure of the total Fire Radiative Energy (FRE), which should be proportional to the total fuel mass combusted (M). The possibility to derive this FRP product from SEVIRI observations with an accuracy similar to that of MODIS for fires capable of being detected by SEVIRI has been demonstrated in the context of a MSG RAO project (Roberts et al., 2005).

The fire detection algorithm implemented for use with SEVIRI is thus an evolution of that first described in Roberts et al. (2005), and is based largely on the principles used to generate active fire detections within the MODIS fire products. The implemented algorithm described herein is very close to the enhanced geostationary fire detection algorithm fully detailed in Roberts and Wooster (2008), and works mainly on statistics derived from the 3.9  $\mu\text{m}$  and 11.0  $\mu\text{m}$  brightness temperatures, and their differences. Data from other channels are used primarily for false alarm identification. An operational version of this algorithm was prototyped at EUMETSAT in 2006 (Govaerts et al., 2007) and its accuracy verified against the original KCL version (Lattanzio 2006) using both Meteosat-8 and -9. This operational algorithm has subsequently been implemented in the Land SAF system in the framework of a direct technical collaboration between EUMETSAT and the Land SAF.

This validation report is based on the outcome of the FREEVAL study (EUM/CO/06/4600000277/YG) which concluded that two products are necessary to exploit the full potential of SEVIRI FRP data in (quasi) operational applications:

- (i) a pixel product containing observed FRP for each individual fire pixel together with ancillary data on the per-pixel FRP uncertainties at the full SEVIRI temporal and spatial resolution (referred to as FRP\_PIXEL);
- (ii) a gridded product, ie, level 3, at a  $1^\circ \times 1^\circ$  resolution containing area integrated FRP totals averaged over one hour time period and empirical corrections for undetected low FRP fires and partial cloudiness at the grid-cell scale (referred to as FRP\_GRIDDED). This product is currently only in “development” status but the validation results are however already presented here as they provide relevant information on the product accuracy.

The derivation of these products is described in the Algorithm Theoretical Basis Document (Govaerts et al., 2007). The core work of this validation report evaluates the efficacy of a retrieval algorithm used to identify actively burning fires and

 	Land SAF VR-FRP	Doc: SAF/LAND/IM/VR_FRP/V_09 Issue: Version V/2009 Date: 18/10/2009
---	-----------------	---

estimate their fire radiative power from SEVIRI observations of fire-affected regions, and determines the effectiveness of the retrieved observations. The assessment of algorithm retrieval accuracy covered several aspects and was tailored to provide sufficient information so that an operational readiness review (ORR) can be issued and the data product can be generated with full specifications.



Validation of the SEVIRI fire radiative power (FRP) product considered four main aspects:

- 1) An evaluation of the theoretical performance of the FRP algorithm;
- 2) An assessment of the accuracy and performance limitations due to the SEVIRI instrument and to the level 1.5 data characteristics from which all SEVIRI geophysical products are currently derived;
- 3) The verification of the performance of the specific FRP algorithm implementation at the Land Surface Analysis Satellite Applications Facility (Land-SAF);
- 4) The impact of the FRP product in operational applications such as aerosol and gas emission due to fires.

Validation was performed through radiative transfer modelling, through product analysis and cross-comparison at the pixel, fire, and grid-cell (*e.g.*,  $1^\circ \times 1^\circ$ ) and regional basis, including comparisons with independent data products. In many cases, data from the EOS Terra and Aqua Moderate Resolution Imaging Spectroradiometer (MODIS) were used as the comparison dataset, since FRP can also be derived from the measurements of this sensor, but the analysis also included data from other sensors and platforms.



Due to the foreseen delay in substantial data products being available from the prototype operational processing chain implemented at EUMETSAT and the LandSAF, it was necessary to make use of different FRP dataset versions with largely similar but not identical characteristics during the FREEVAL study. Hence, much of the fundamental validation work was carried out with a full one year duration (Feb 2004 – Jan 2005) FRP dataset produced by running the first operational (non-commissioning phase) Meteosat-8 SEVIRI data through an enhanced version of the original fire detection and FRP algorithm developed at KCL in the Interactive Data Language environment (Wooster et al., 2003, 2005; Roberts et al., 2005, 2008). In parallel with this activity, a version of this enhanced algorithm was being implemented in C at EUMETSAT as the prototype processing chain, and was later ported to the Land SAF processing facility at the IM in Lisbon. Minor modifications were required to adjust the KCL code to the intricacies of the operational environment, and the details of this implementation are described in the algorithm theoretical basis document (Govaerts et al., 2007). Data from the Land SAF processing chain was made available later during the FREEVAL study, and the performance of this Land SAF product is here compared to that produced by the KCL processing chain. Some perturbations to performance are also expected due to unresolved differences between the calibration of the Meteosat-8 and Meteosat-9



 	Land SAF VR-FRP	Doc: SAF/LAND/IM/VR_FRP/V_09 Issue: Version V/2009 Date: 18/10/2009
---	-----------------	---

imaging radiometers, particularly at higher signals such as are obtained over fires in the 3.9  $\mu\text{m}$  spectral band.

A second important aspect of the FREEVAL project was the identification of potential users of the FRP product and the specification of user needs, which were then gauged against the product characteristics. The main users, who were identified prior to the project and were actively engaged in FREEVAL with discussions and sensitivity modelling studies, were national and European weather centres (UK Met Office and ECMWF). These centres are developing a range of applications requiring knowledge of atmospheric composition and emissions, including those from open vegetation burning. They expressed a strong need for an accurate and rapidly available data product helping them to quantify trace compound emissions from fires with good spatial and temporal resolution. The conclusions of this report reflect the consortium's view as to how well the SEVIRI FRP product can match user requirements. We also provide some recommendations how future developments could further enhance the existing capabilities for global and regional earth observation and monitoring of emissions from such fires.

 	<p>Land SAF VR-FRP</p>	<p>Doc: SAF/LAND/IM/VR_FRP/V_09 Issue: Version V/2009 Date: 18/10/2009</p>
---	------------------------	--

# 1. INTRODUCTION

## 1.1 FRP Product Background



“Forest fire” has been agreed as a MSG day-2/priority3 product during STG 37. Since “forest fire” encompasses many different types of products and associated applications, a better definition of a SEVIRI-based fire product was necessary. Several studies have been dedicated to that purposes (Pereira and Govaerts, 2001, Flasse 2004) which identified the Fire Radiative Power (FRP) as the most appropriate product that can be derived from SEVIRI observations, with relevant applications related to the science community interested in modelling of the carbon cycle. The development of such product has been endorsed in September 2005 by SWG-19 following a presentation given by Prof. M. Wooster who demonstrated, in the context of a MSG RAO project (Roberts *et al.*, 2005), the possibility to derive this product from SEVIRI observations with an accuracy similar to that of MODIS for fires capable of being detected by SEVIRI. This “proof-of-concept” work undertaken under the MSG RAO led by Prof. M. Wooster (hereafter referred to as the KCL algorithm) has been used as a starting point for the development of an operational version.

Such an operational version of this algorithm was prototyped at EUMETSAT in 2006 (Govaerts *et al.*, 2007) and its accuracy verified against the original KCL version using both Meteosat-8 and -9 (Lattanzio 2006). During this exercise, a discrepancy between SEVIRI band 3.9 onboard Meteosat-8 and -9 occurring at high temperature has been identified (Lattanzio and Govaerts, 2006). This operational algorithm has subsequently been implemented in the Land SAF system in the framework of a direct technical collaboration between EUMETSAT and the Land SAF. During its 5th meeting held in Brussels on 22 February 2007, the Land SAF IOP Steering Group welcomes this initiative and recommends the next SG (CDOP) to endorse this activity.

Late 2006, an external study (EUM/CO/06/4600000277/YG), referred to as the FREEVAL study (Schultz *et al.*, 2008), has been initiated at EUMETSAT aiming at (i) evaluate the FRP product currently prototyped at EUMETSAT and (ii) define user’s requirements for Fire Radiative Power derived from Meteosat-8/9 data at EUMETSAT that would support operational applications. This validation report is based on the outcome of the FREEVAL study.

This study concluded that two products are necessary to exploit the full potential of SEVIRI FRP data in (quasi) operational applications:

- (i) a pixel product containing observed FRP for each individual fire pixel together with ancillary data on the per-pixel FRP uncertainties at the full SEVIRI temporal and spatial resolution (referred to as FRP\_PIXEL);
- (ii) a gridded product, ie, level 3, at a  $1^\circ \times 1^\circ$  resolution containing area integrated FRP totals averaged over one hour time period and empirical

 	Land SAF VR-FRP	Doc: SAF/LAND/IM/VR_FRP/V_09 Issue: Version V/2009 Date: 18/10/2009
---	-----------------	---

corrections for undetected low FRP fires and partial cloudiness at the grid-cell scale (referred to as FRP\_GRIDDED). This product is currently only in “development” status but the validation results are however already presented here as they provide relevant information on the product accuracy.

The derivation of these products is described in the Algorithm Theoretical Basis Document (Govaerts et al., 2007). Except when specifically mentioned, this validation report essentially focuses on the validation of the FRP\_PIXEL product generated with the FRP\_PIXEL algorithm **version 0.8** in the Land SAF system.

## 1.2 Document structure

The use of the FRP product for the fire emission estimation is a rather new concept which is explained in Section (0). Its derivation from space observations is briefly described in Section (0). Section (0) lists the technical limitations associated with FRP extraction from SEVIRI observations. The overall strategy of the validation is explained in Section (0).



As the FRP product is based on novel concepts, no well-established user requirements can be found in the literature. Hence, Section (2) is entirely dedicated to the analysis of potential FRP applications and associated requirements.

Detailed descriptions of the reference datasets, the validation methodology and validation results are provided in Sections (3), (4) and (5), respectively. The validation efforts reported on here also include tests of the implementation of the SEVIRI FRP product for fire emissions and atmospheric transport modelling (case studies), also reported in Section (5). Major outcome of this first FRP validation effort are summarised in Section (0).

## 1.3 FRP Product Concept

Open vegetation fires are an important disturbance agent of the terrestrial biosphere, and represent a ubiquitous, highly variable emission source for many key greenhouse gases, air pollutants, and aerosols. Even though natural fires (ignited by lightning or volcanoes) have occurred throughout Earth’s vegetated history, today the vast majority are initiated by humans. Fire is commonly used for land clearance and management, pest control and soil fertilization. Fires are most frequent in tropical and subtropical regions, with Africa usually regarded the continent with the most wide-spread fire occurrence. Emissions from vegetation fires are increasingly recognized as an important parameter in atmospheric modelling, and their accurate description is a fundamental pre-requisite for the installation of operational services to monitor and predict atmospheric composition and the long-range transport of air pollutants, and for the monitoring of compliance with international treaties on greenhouse gas and air pollutant emission ceilings.

The observation of open fires from space has greatly advanced our understanding of the global dimension of this phenomenon and of the spatial and temporal patterns of

 	Land SAF VR-FRP	Doc: SAF/LAND/IM/VR_FRP/V_09 Issue: Version V/2009 Date: 18/10/2009
---	-----------------	---

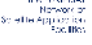

fire occurrence. Nevertheless, it has proven very difficult to use the remote sensing of active fires or the mapping of burned areas for accurate, temporally and spatially consistent estimates of emissions from these fires, and to provide these data in timeframes useful for atmospheric forecasting. This has to do on the one hand with great uncertainties in the estimates of fuel load and combustion behaviour (which have typically been required to convert observations of active fires or burned area into emission fluxes), and on the other hand with the non-ideal nature of the available EO systems for this application (*e.g.*, limited imaging frequency and inappropriate sensor characteristics). The lack of a near real-time data delivery of fire products from such systems has also hampered such efforts.

Fire observation has rarely been a primary mission objective for the design of satellite instruments. As a consequence, almost all sensors that can be used for fire detection and fire characterisation suffer from instrument saturation effects, relatively limited spatial and/or temporal resolution, and other limiting factors. Specifically, the temporal sampling from low earth orbit instruments is often inadequate for capturing the high temporal variability of fire occurrence and fire strength, and for fully resolving the fire diurnal cycle (which is known to be extreme in some areas). The data delivery of ‘fire products’ from such systems has in the main not been viewed as an ‘operational’ near-real time service, but rather a service to the science community, but the former is required if the data are to support timely applications such as those involving forecasting of trace gas/aerosol concentrations, air quality and visibility.

Active fire data provided by the SEVIRI instrument on board Meteosat 8/9 promised significant advancements in the current state-of-the-art of fire monitoring and emission quantification systems in two ways.

Firstly, its main observable, the Fire Radiative Power (FRP) of each detected active fire pixel, is expected to be directly related to the rate of combustion of biomass and thus the release of smoke emissions from the identified fires (Wooster et al., 2005). The FRP provides information on the measured radiant heat output of detected fires (in units of megawatts). Its integration over the lifetime of a fire, the fire radiative energy (FRE), should therefore be directly proportional to the accumulated emissions released by the fire. This has been verified in a number of small-scale field experiments, but needs further proof on regional to continental scales. Quantifying emissions based on FRE eliminates the need to separately assess burned area, fuel loads, and combustion rates as is done currently in most emissions assessment methods, and therefore removes a whole series of uncertainties due to our often rather limited knowledge of these variables.

Secondly, since SEVIRI is employed on a geostationary platform, it can sample a large footprint with high (15 min) frequency, and can therefore deliver important information on the temporal variability of fires. A limitation is that the relatively coarse spatial resolution of the measurements (3 km sampling distance at the sub-satellite point) lowers the detection probability of the smaller/less intense fires, and such fires therefore remain unaccounted for (*i.e.* undetected) in the raw output product. By definition each such fire may each be releasing relatively small amounts of pollutants, but the total number of these smaller fires may make their cumulative

 	Land SAF VR-FRP	Doc: SAF/LAND/IM/VR_FRP/V_09 Issue: Version V/2009 Date: 18/10/2009
---	-----------------	---

emissions significant, and so statistical adjustment of the product to deal with this bias maybe warranted.

## 1.4 Theory of the FRP Algorithm

The MIR radiance method of FRP estimation was first presented in Wooster et al. (2003) and is based on simple approximations to the physical laws governing the emission of thermal radiation from fires. The MIR radiance method exhibits two potential advantages over dual-wavelength methods such as those originally presented in Dozier (1981). Firstly it relies only on quantification of the fire pixel in a single spectral channel, removing problems related to interchannel spatial mis-registration that potentially impact such dual spectral band approaches (Shephard and Kennelly, 2003), and secondly it relies only on quantification of the fire signal in the MIR spectral band only, where spectral radiative emission from wildfires is maximised and thus where the signal increase of the fire pixel over the ambient background window signal is at its greatest (*i.e.*, the S/N is optimised). For these reasons, the method used to derive FRP in the official MODIS fire products also uses measurements in the MIR spectral band (Kaufman *et al.*, 1998a), though in that case expressed in terms of brightness temperatures rather than radiances. The MIR radiance method of FRP derivation is defined by:

$$FRP_{MIR} = \left( \frac{\sigma \varepsilon_f}{a \varepsilon_{f,MIR}} \right) L_{f,MIR} \quad [Wm^{-2}]$$

### Equation 1.1

where  $\sigma$  is the Stefan-Boltzmann constant ( $5.67 \times 10^{-8} W m^{-2} K^{-4}$ ),  $\varepsilon_f$  is the emissivity of the fire over all wavelengths, and  $\varepsilon_{f,MIR}$  is the emissivity over the MIR spectral band. In the absence of data to the contrary gray body behaviours is assumed ( $\varepsilon_f = \varepsilon_{f,MIR}$ ), and this is understood to be a realistic approximation for vegetation fires (Langaas, 1995).

$a$  ( $W m^{-2} sr^{-1} \mu m^{-1} K^{-4}$ ) is a constant determined from the empirical best-fit relationship between the fourth power of the blackbody emitter temperature,  $T$  and the emitted spectral radiance,  $B(\lambda_{MIR}, T)$ , in the MIR spectral band [*i.e.*  $B(\lambda_{MIR}, T) = aT^4$ ], made over the range of emitter temperatures appropriate to actively burning fires. Since the Stefan-Boltzman Law states that the true fire radiative power emitted over all wavelengths is also a function of the fourth power of the emitter temperature, then the FRP can be estimated as a linear function of the fires MIR emitted spectral radiance, as expressed in Equation 1.1.

In Equation 1.1,  $L_{f,MIR}$  ( $Wm^{-2} sr^{-1} \mu m^{-1}$ ) represents the MIR spectral radiance emittance of the fire. However, under the circumstances pertaining to the observation of sub-pixel sized fires by a system such as SEVIRI, the fire is not fully resolved by the imaging system and the at-sensor received signal  $L_{MIR}$  is in fact the summation the following terms; emitted fire thermal radiance, solar and atmospheric downwelling

irradiance reflected from the fire, emitted thermal radiance from the non-fire background, solar and atmospheric downwelling irradiance reflected from the non-fire background, and upwelling atmospheric thermal radiation:

$$\begin{aligned}
L_{MIR} = & \tau_{MIR} p_f \varepsilon_{f,MIR} B(\lambda_{MIR}, T_f) + \tau_{MIR} p_f (1 - \varepsilon_{f,MIR}) (\tau_{d,MIR} I_{sun,MIR} \cos \phi + I_{atm,MIR}) / \pi \\
& + \tau_{MIR} (1 - p_f) \varepsilon_{b,MIR} B(\lambda_{MIR}, T_b) + \tau_{MIR} (1 - p_f) (1 - \varepsilon_{b,MIR}) (\tau_{d,MIR} I_{sun,MIR} \cos \phi + I_{atm,MIR}) / \pi \\
& + L_{atm,MIR}
\end{aligned}$$

### Equation 1.2

where  $\tau_{MIR}$  is the upward atmospheric transmission in the sensors MIR spectral band,  $\phi$  is the solar zenith angle,  $\tau_{d,MIR}$  is the downward atmospheric transmission in the sensors MIR spectral band at angle  $\phi$ ,  $I_{sun,MIR}$  is the extraterrestrial solar irradiance in the sensors MIR spectral band,  $I_{atm,MIR}$  is the diffuse downwelling atmospheric irradiance in the MIR spectral band, and  $L_{atm,MIR}$  is the upwelling atmospheric spectral radiance in the MIR spectral band, the other symbols ( $T$ ,  $\varepsilon$ ,  $p$ ) have their previously defined meanings, with subscript  $f$  corresponding to their value at the fire and  $b$  at the non-fire background.

Similarly for a neighbouring non-fire ‘background’ pixel:

$$L_{b,MIR} = \tau_{MIR} \varepsilon_{b,MIR} B(\lambda_{MIR}, T_b) + \tau_{MIR} (1 - \varepsilon_{b,MIR}) (\tau_{d,MIR} I_{sun,MIR} \cos \phi + I_{atm,MIR}) / \pi + L_{atm,MIR}$$

### Equation 1.3

The fire emitted spectral radiance in the MIR spectral band,  $L_{f,MIR}$ , required for input into Equation 1.1 is in fact the  $p_f \varepsilon_{f,MIR} B(\lambda_{MIR}, T_f)$  term on the right hand side of Equation 1.2, and its value can be obtained numerically by combining Equation 1.2 and Equation 1.3:

$$\begin{aligned}
L_{MIR} = & \tau_{MIR} p_f \varepsilon_{f,MIR} B(\lambda_{MIR}, T_f) + L_{atm,MIR} + (1 - p_f) (L_{b,MIR} - L_{atm,MIR}) \\
& + \tau_{MIR} p_f (1 - \varepsilon_{f,MIR}) (\tau_{d,MIR} I_{sun,MIR} \cos \phi + I_{atm,MIR}) / \pi
\end{aligned}$$

### Equation 1.4

and re-arranging:

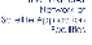

$$\begin{aligned}
p_f \varepsilon_{f,MIR} B(\lambda_{MIR}, T_f) = & \frac{1}{\tau_{MIR}} (L_{MIR} - (1 - p_f) L_{b,MIR} + p_f L_{atm,MIR}) \\
& - p_f (1 - \varepsilon_{f,MIR}) (\tau_{d,MIR} I_{sun,MIR} \cos \phi + I_{atm,MIR}) / \pi
\end{aligned}$$

### Equation 1.5

Equation 1.5 represents the true value of  $p_f \varepsilon_{f,MIR} B(\lambda_{MIR}, T_f)$  for use as  $L_{f,MIR}$  in Equation 1.1. Multiplying the output of Equation 1.1 by the sensor pixel area then provides an estimate of the fire radiative power in Watts (generally expressed in MW due to the large fire radiative power values observed from open wildfires), based only on the MIR spectral signal.

However, certain of the parameters in Equation 1.5 cannot be determined, for example the fire fractional area,  $p_f$ , whilst others, for example the atmospheric parameters are



 	Land SAF VR-FRP	Doc: SAF/LAND/IM/VR_FRP/V_09 Issue: Version V/2009 Date: 18/10/2009
---	-----------------	---

likely to be imperfectly known. By neglecting the (relatively) unimportant terms, Equation 1.5 can be greatly simplified and then parameterised using even coarse resolution satellite data, in order to provide an estimate of  $L_{f,MIR}$  for input into Equation 1.1.

The first assumption is that the atmospheric term  $p_f L_{atm,MIR}$  on the right hand side of Equation 1.5 will always be small compared to at least one of the first two terms and is therefore negligible. Next, the requirement to know the fire fractional area is removed by assuming that  $(1-p_f)L_{b,MIR} \approx L_{b,MIR}$ , which is considered workable when  $p_f$  is sufficiently small, and as  $p_f$  increases the error this assumption introduces is still negligible since in that case the spectral radiance of the fire pixel will be increasingly dominated by emittance from the (increasingly large) fire rather than from the much cooler ambient temperature background (since  $B(\lambda_{MIR}, T_f)$  can be four orders of magnitude larger than  $B(\lambda_{MIR}, T_b)$  at MIR wavelengths). The final term in Equation 1.5, corresponding to the solar and downwelling atmospheric radiation that are reflected from the fire, is assumed negligible for the same reason.

Via these simplifications the fire-emitted spectral radiance ( $L_{f,MIR}$ ) for input into Equation 1.1 can be estimated from the difference between the MIR spectral radiance of the active fire pixel ( $L_{MIR}$ ) and that of the surrounding non-fire ‘background’ ( $L_{b,MIR}$ ) calculated as the mean signal of the ‘background window pixels, and adjusted for the MIR atmospheric transmission:

$$L_{f,MIR} = p_f \varepsilon_{f,MIR} B(\lambda_{MIR}, T_f) = \frac{1}{\tau_{MIR}} (L_{MIR} - L_{b,MIR})$$



**Equation 1.6**

The impact of the assumptions made during the derivation and application of the above equation used to estimate  $L_{f,MIR}$ , the assumptions made during the derivation of Equation 1.1, will control the theoretical accuracy of the FRP algorithm.

## 1.5 Factors Limiting FRP Product Accuracy

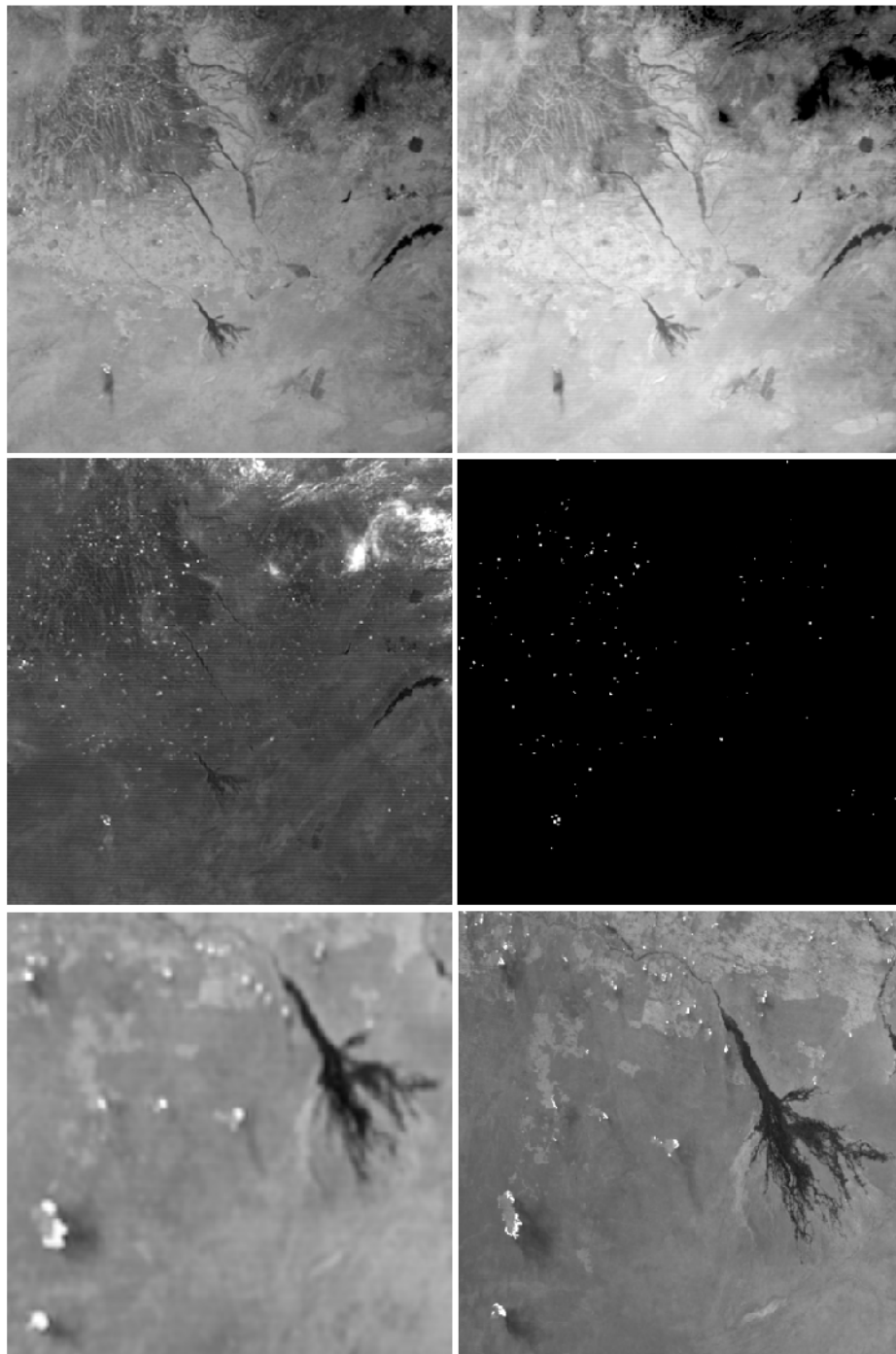
Although SEVIRI has been designed for operational weather forecasting and not specifically for fire detection, its MIR channel (thermal band centred at 3.9  $\mu\text{m}$ ) shows great potential for fire detection and the measurement of fire radiative power (FRP) using Equation 1.1 and Equation 1.5, as demonstrated in Figure 1.1. However, the MIR channel of the SEVIRI sensor has a saturation level of  $\sim 335$  K, and as a result a certain proportion of the particularly large and/or high intensity fires are expected to cause saturation of the measurements in this spectral band. Whilst this will not impact detection of such fire pixels (indeed their large signal will very likely make them amongst the most detectable such events), it will lead to an impact on the accuracy of the FRP measurements of such fires since their MIR spectral radiance will be underestimated.





 	Land SAF VR-FRP	Doc: SAF/LAND/IM/VR_FRP/V_09 Issue: Version V/2009 Date: 18/10/2009
---	-----------------	---

A further factor influencing FRP product accuracy is the relatively coarse spatial resolution of the SEVIRI MIR channel, which also varies with viewing geometry. The sub-satellite pixel size is 4.8 x 4.8 km (FWHM), and these 23 km<sup>2</sup> pixels are oversampled by a factor 1.6 in the EW and SN directions leading to a sub-satellite pixel sampling distance of 3 x 3 km. Pixels close to the disk edge (for example those over Madagascar and South America) reach areas of ~ 90 km<sup>2</sup>. The relatively large pixel size limits the detectability of small/low intensity fires having a low FRP, and may lead to a misinterpretation of fire clusters as individual large fire events. The increasing pixel size away from the sub-satellite point is expected to increase the significance of these events relative to smaller fires.

Finally, the on-board processing of SEVIRI data and its conversion to the level 1.5 radiance product from which all geophysical datasets including the FRP product are derived (termed here the level 1 to level 1.5 processing) introduces perturbations to the measurements made in each spectral band. This will include the introduction of interpolation errors due to the geolocation and projection onto the nominal geostationary projection centered at (0°; 0°) (see EUMETSAT Technical Document EUM/MSG/ICD/105, 2007).



*Figure 1.1: Imagery of southern Africa on 4 September 2003, in which numerous active fires are burning. (a)-(d) are derived from SEVIRI data covering a 1200 km wide region, collected at 12:12 UTC. (a) 3.9 $\mu$ m, (b) 10.8 $\mu$ m, (c) 3.9 $\mu$ m - 10.8 $\mu$ m brightness temperature difference, and (d) mask of confirmed active fire pixels. (e) and (f) show, respectively, a SEVIRI and MODIS MIR image subset centred on the Okavango delta region of Botswana, captured at 11:57 UTC and 12:05 UTC respectively.*

 	Land SAF VR-FRP	Doc: SAF/LAND/IM/VR_FRP/V_09 Issue: Version V/2009 Date: 18/10/2009
---	-----------------	---



## 1.6 Validation Strategy

The initial implementation of the geostationary fire detection algorithm was made at King's College London using commissioning phase SEVIRI data, and was coded in the Interactive Data Language (IDL) environment (Roberts et al., 2005). At the start of the validation activity this algorithm was in the process of being significantly improved, and it is this improved implementation that forms the basis of the approach to be used in the proposed operational production of FRP data from SEVIRI, as outlined in the FRP Product Algorithm Theoretical Basis Document (Govaerts et al., 2007). Details of this fire detection algorithm are provided there in full, and are also included in a forthcoming paper (Roberts and Wooster, 2008) and so will not be repeated here.

After the fire detection process, each pixel has its FRP estimated, as a function of the pixels MIR spectral radiance increase above the background non-fire signal. The theory behind this approach to FRP estimation can be found in Wooster et al. (2003; 2005), and Section (0) of this document. Hence, much of the fundamental validation work described herein was carried out with dataset covering a full one-year duration (Feb 2004 – Jan 2005) that was produced at KCL by running the first year of operational (non-commissioning phase) Meteosat-8 SEVIRI data through the available IDL-coded processing chain. This product is here referred to as the *KCL FRP dataset*, and is supplemented by Meteosat-9 derived FRP data from July and August 2007 produced by the same system. It is assumed that the validation of the algorithm mathematical concept is independent from the environment where the algorithm is used.

At the start of the validation, a prototype FRP algorithm was developed at EUMETSAT in C language, using the KCL IDL code as the basis but with minor modifications to deal with the operational environment (Lattanzio 2006). The details of this implementation are fully described in Govaerts et al. (2007), and this is the code that runs at the LandSAF processing facility at the IM in Lisbon and which generates the operational FRP product. Data from the LandSAF processing chain was made available later during the FREEVAL study, produced solely from Meteosat-9 SEVIRI data of 2007, and the performance of this *LandSAF FRP* product is here compared to that produced by the KCL processing chain to ensure that it has similar product accuracy characteristics. Some perturbations to performance are expected due to the aforementioned (small) differences in the KCL and EUMETSAT/LandSAF processing chains, and due to unresolved differences between the calibration of the Meteosat-8 and Meteosat-9 imaging radiometers, particularly at higher signals such as are obtained over fires in the MIR channel (Lattanzio and Govaerts, 2006).

Considering the potential aspects theoretically limiting the accuracy and performance of the SEVIRI FRP algorithm and outlined in Sections (0) and (0), and the availability of FRP products produced via the KCL and EUMETSAT/LandSAF data processing chains, the strategy adopted to validate the SEVIRI FRP product was to individually assess the following aspects:

 	Land SAF VR-FRP	Doc: SAF/LAND/IM/VR_FRP/V_09 Issue: Version V/2009 Date: 18/10/2009
---	-----------------	---



- (1) **The theoretical and actual performance of the SEVIRI fire detection and FRP algorithm:** This is assessed using model simulations and analysis of the *KCL FRP* product and matching MODIS-derived FRP data.
- (2) **The accuracy and performance limitations introduced due to the SEVIRI instrument characteristics and level 1.0 to 1.5 data pre processing procedures:** This is assessed using model simulations and analysis of matching SEVIRI level 1.0 and 1.5 data and data from SEVIRI ‘special’ mode operations
- (3) **The actual performance of the operational algorithm implementation at the Land Surface Analysis Satellite Applications Facility [Land-SAF];** assessed using the *LandSAF FRP* product and comparisons to the *KCL FRP* product and to matching MODIS-derived FRP data.
- (4) **The impact of using it in potential operational applications:** Both the *KCL FRP* and *LandSAF FRP* products have been used in these exercises.

The validation strategy approach comprises both theoretical modelling, including simulations of the spectral energy emissions of fires of different sizes/tempreatures and calculations of the atmospheric effects on such signals with the MODTRAN radiative transfer code (Berk et al., 1999), and comparisons to independent observations of the same parameter (*i.e.*, per-fire FRP and per-area FRP) made with the MODIS sensor onboard the polar-orbiting EOS Terra and Aqua satellites. The data sets used in these comparisons are described in Section (3).

Under (1) the underlying assumptions of the FRP algorithm are considered via an analysis of the numerical approximations made during its derivation, and the main error sources impacting the product are considered. In addition, a sensitivity analysis was performed including the effect of SEVIRI MIR channel saturation and background thermal ‘clutter’ (referring to the fact that the background temperature signal upon which the fire signal is superimposed is unlikely to be uniform).

Findings from the simulation are compared to the actual retrieved range of fire characteristics present in the FRP data to determine the consistency of the product in relation to the theoretical performance and determine whether the current error estimations are appropriate. The impact of the SEVIRI 3.9  $\mu\text{m}$  channel saturation was considered in terms of the percentage of observations where saturation has an impact, and its temporal distribution.

The products’ error of fire detection omission, commission and FRP accuracy is assessed via comparison of the *KCL FRP* product to near simultaneous MODIS observations (both at a per-fire level, as well as over fixed grid-cells and regions of the MODIS swath for regional-scale comparisons). In this exercise, and in the subsequent validation of the LSA SAF SEVIRI FRP Product, we use all MODIS


 	Land SAF VR-FRP	Doc: SAF/LAND/IM/VR_FRP/V_09 Issue: Version V/2009 Date: 18/10/2009
---	-----------------	---

observations, irrespective of their confidence parameter. We also derive FRP from MODIS radiances using the same MIR radiance method (Wooster et al., 2003) that is used with SEVIRI [rather than using the MODIS method result, which is contained within the MODIS MOD14/MYD14 products). In this way the SEVIRI and MODIS FRP estimates are directly comparable. We do use the official MODIS fire detections to identify the MODIS fire pixel locations, since the MOD14/MYD14 fire detection algorithms have undergone significant validation and are currently the standard against which most other fire detection algorithms are gauged (Giglio et al., 2003). This analysis includes an assessment of the fire detection capabilities of SEVIRI in various vegetation cover classes. MODIS was selected as the reference data set because of its relatively finer spatial resolution (1 km at the sub satellite point) and its sufficient data coverage (up to 4-times daily observations over Africa). Daytime and nighttime MODIS to SEVIRI FRP comparisons have been conducted, across the fire-affected regions of the SEVIRI disk. Furthermore, derivative secondary datasets, which are themselves derived from observations made by MODIS are also used. One of these is the Global Fire Emissions Database (GFED) (van der Werf et al. 2006), whose fire emissions calculations are based upon the previously mentioned burned area  $\times$  fuel load  $\times$  combustion completeness relationship. In version 2 of the GFED database, burned area is actually calibrated from cumulative counts of MODIS hotspots (i.e. active fire detections) and a previously derived relationship between this variable and actual area burned in the causal fire (van der Werf et al. 2006).

Under (2) the impact of the observational and data pre-processing procedures used to generate the SEVIRI level 1.5 data product, which is the input to all versions of the FRP processing chain, was assessed via simulation modelling of the SEVIRI observations process when viewing active fires, by comparisons of level 1.0 and 1.5 data recorded under standard conditions, and via analysis of co-incident Meteosat 8 and 9 SEVIRI data when the Meteosat 8 instrument was operated in a number of non-standard modes (including a low gain mode to reduce or negate the influence of sensor saturation).


Under (3), the fire detection and FRP products output from the recently implemented LandSAF data processing chain were validated. This chain will ultimately be used to produce the operational SEVIRI FRP product foreseen to be produced from mid-2008 onwards (see <http://landsaf.meteo.pt/algorithms.jsp?seltab=8>). The aim of the LandSAF product validation is to demonstrate that the LandSAF operational products have the same or similar accuracy to those produced by the original IDL code used at KCL. Since the EUMETSAT-derived C code operating at the LandSAF is essentially an implementation of the original KCL algorithm written in IDL, with some small modifications necessary for its implementation in an operational environment, it should be expected that the performance of the two products is similar (Lattanzio 2006).

Finally, under (4), the content, efficacy and value of the spatio-temporal patterns and magnitude of burning provided by the information contained within the SEVIRI FRP product have been assessed via an 'impact analysis' study. This was undertaken via inclusion of the data product as an emissions source term in a series of specific impact

	Land SAF VR-FRP	Doc: SAF/LAND/IM/VR_FRP/V_09 Issue: Version V/2009 Date: 18/10/2009
---	-----------------	---

studies, with comparison of the results to those found when using alternative fuel consumption databases (*e.g.*, GFED version 2, van der Werf et al., 2006) as the source term. In these impact studies, the results of atmospheric modelling applications using SEVIRI FRP information to estimate fire emission fluxes were evaluated with independent data sources measuring the atmospheric composition and its changes due to vegetation fires. The strategic approach comprises the following steps: The FRP product from the KCL chain was formatted and distributed to the users ECMWF and Met Office. Emission factors were used to convert the FRP data to emissions estimates. Due to the need for global emission data sets, SEVIRI FRP derived emissions were superimposed on an existing global data set based on MODIS fire counts (GFEDv2). Model runs with and without blending of the FRP-derived emissions, were conducted in order to assess the adjustments to the model outputs provided by the FRP products inclusion. Comparisons to *in situ* and/or remotely sensed observations of atmospheric constituents (mainly aerosols) perturbed by major biomass burning events allowed for an assessment of the impact of the FRP data product on the model results. Consideration was given to whether adjustments to the FRP product spatio-temporal characteristics or error specifications are required to provide an optimum emissions data source for ingestion into these currently operating simulation models.



	Land SAF VR-FRP	Doc: SAF/LAND/IM/VR_FRP/V_09 Issue: Version V/2009 Date: 18/10/2009
---	-----------------	---

## 2. FRP REQUIREMENT DEFINITION

### *2.1 Identification of Potential Operational Users*

In the context of this project we define operational use predominantly as short-term “chemical weather” and “air quality” forecasts and reanalysis simulations of greenhouse gases, aerosols, and reactive gas-phase compounds, all of which are significantly affected by emissions to the atmosphere from open vegetation fires. In light of the ongoing urgent and high-profile development of such services, and given the relatively coarse spatial resolution of the SEVIRI FRP product, these seem certainly the most promising applications in the near future. Other potential applications could include early detection of new fires (for fire fighting and management purposes), the monitoring of land-use change by fire, and assessment of climate impacts on fire activity. FREEVAL established a list of potential applications and contacted a number of key potential users to inform them about the availability of an FRP product from SEVIRI and sample their specific requirements. An evaluation of the product with respect to these ‘secondary’ applications will require another dedicated study.

#### **2.1.1 Chemical Weather Forecasting/Monitoring**

Besides the large European efforts in the GEMS project, which includes global trace compound forecasts and analyses at ECMWF as well as a suite of regional-scale European air quality models, there are other similar activities in the United States (Navy Research Laboratories, Monterey, CA; NOAA), Canada (Environment Canada) and in Brazil (INPE-CPTEC). Principal investigators from these initiatives were contacted and expressed their interest in the SEVIRI FRP methodology and in the data product so produced. Due to the similar nature of these systems we expect that they will have very similar requirements as the GEMS system.

GEMS is expected to develop into the core service component of the GMES Atmospheric Service, and several project members already made a commitment to make use of the SEVIRI FRP product in their respective modelling efforts on greenhouse gases, reactive gases, aerosols and regional air quality, respectively. Some further development of the GEMS models is needed before the product can be used as a regular and primary input data set for fire emissions. These developments have been written into the work plan of the GEMS successor project Monitoring of Atmospheric Composition and Climate (MACC). Initial use of the near-real-time SEVIRI FRP product is envisioned for the summer of 2008.

#### **2.1.2 Validation of Prognostic Fire Models and Visibility Forecasts**

There are two potential applications of SEVIRI FRP data that were further explored during FREEVAL at the Met Office in Exeter, UK. Firstly, the FRP product can be

extended to estimate CO<sub>2</sub> emission released by fires. This, in turn, can be compared to the output of on-line and off-line interactive fire models. Such a procedure allows a useful verification of current fire models. An example of such a comparison is shown in Figure 2.1.

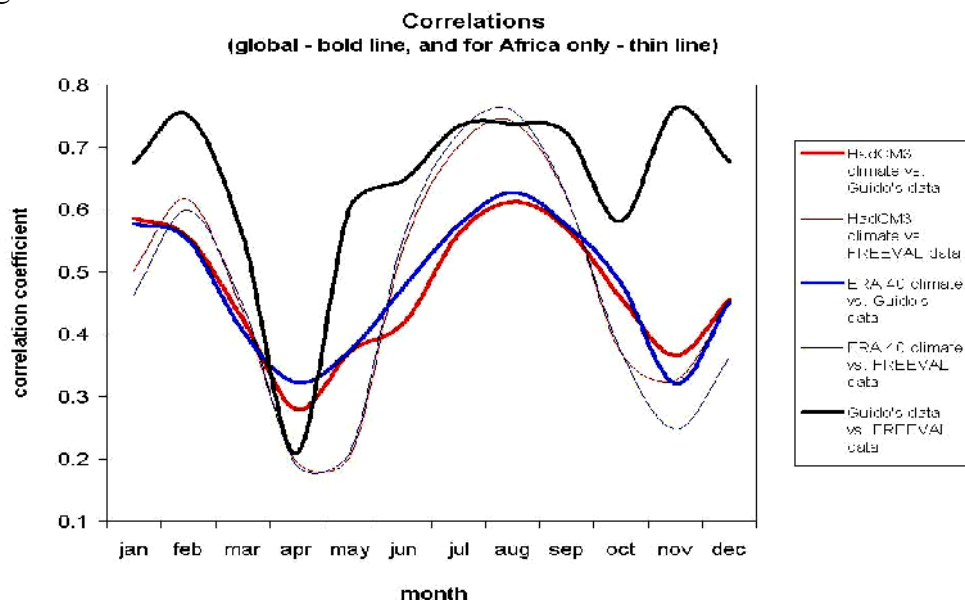


**Figure 2.1:** Example of a comparison of the correlation of monthly burned area derived from the fire model Had\_FIRE (using HadCM3 or ERA 40 climate data) with burned area derived from the GFED (Guido van der Werf et al. 2006) and from SEVIRI (FREEVAL).

A temporal resolution of 3 hours is sufficient for this purpose and would allow evaluation of the diurnal cycle of fire emissions, which is known to exhibit large variations in such areas as the African savannah. A spatial resolution of 1°×1° would match current GCM grid-size. In the case of such model modification/validation applications, there is no need to obtain FRP data in real or near-real time.

A further application of the FRP product lies with visibility forecasts. There is a small but increasing interest from various stakeholders in NRT forecast of atmospheric visibility in different regions of the world. The decrease in visibility associated with open fires requires an accurate source term for the emission of particulate matter from fires. The FRP product can be extended to provide estimates of particulate matter (PM) emissions, with emission factors depending on the type of ecosystem, and possibly the size of the fire. Temporal resolution of 1 to 3 hours and spatial resolution of about 10 km would be sufficient given the current resolution of models used for visibility forecasting at the regional scale.

In conclusion the FRP product will prove very useful at the Met Office as the importance of visibility forecasts and fire modelling grows. The operational provision of the FRP product is therefore strongly encouraged.



### 2.1.3 Public Information and Safety Aspects

South Africa operates a public fire information system reporting on the nightly weather forecast and on the web (<http://safnet.co.za/>). This is presently based mainly on MODIS active fire observations, though locally generated active fire detections from SEVIRI are available in addition, and the system could well benefit from the inclusion of operationally produced SEVIRI FRP data. Another application is the internal fire early warning system used by ESCOM (South African Power Company), which uses the locally-produced SEVIRI active fire information to determine when and where fires are burning close to electrical power lines. If they are deemed to pose a threat to power safety the line can be shut down before a ‘flashover’ (essentially a spark induced by the heated air and flames above a fire) can occur. At the present time locally derived MODIS and SEVIRI active fire location data are used for this application, and discussions with ESCOM resulted in the quote that the SEVIRI data were actually the most useful for the purpose due to its capability to detect rapidly changing fires, and the possibility for near realtime data transmission. Whilst MODIS can detect smaller fires, its usefulness is limited by the far less frequent nature of the observations. The potential value of additional FRP information to this application was determined using SEVIRI-derived FRP data for 2004 for fires that were identified as being close (within 10 km on the SEVIRI observational grid) to a power line.

Figure 2.2 confirms that fires that resulted in flashovers have, on average, an FRP that is higher than those that do not, and that the difference is statistically significant. This implies that the operational provision of SEVIRI FRP data might lead to an improved warning system at ESCOM and potentially other electric power companies in Africa.

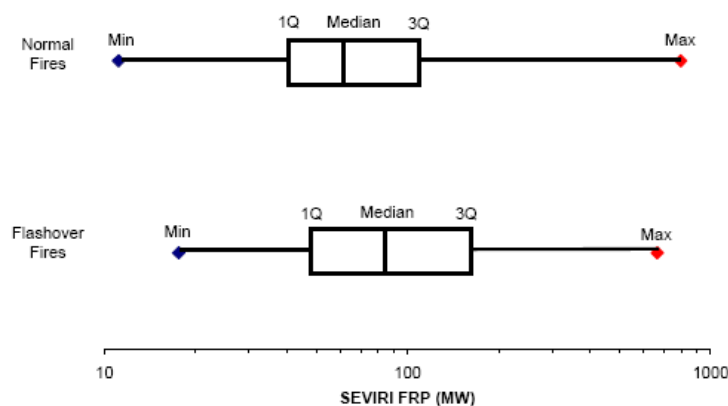


**Figure 2.2:** Differences in FRP for fires related to flashover events and those that pass within 10 km of the transmission line but which do not result in a flashover.

### 2.1.4 Scientific Studies

Several members of the atmospheric science community have expressed great interest in SEVIRI FRP data, because of its potential to improve accurate quantification of

trace compound emissions from fires and to study fire behaviour and climatology in Africa and southern Europe. Through the combined use of multiple remote sensing products, a more accurate and reliable quantification of fire emissions should become possible. As stated previously, the presently employed method for estimating fire emissions as input to atmospheric modelling studies relies on knowledge of the pre-burn fuel load and the combustion completeness. The SEVIRI FRP product can provide an independent validation for this approach. Figure 2.3 shows an example of such a comparison, where the SEVIRI time-integrated FRP data of a series of fires located in southern African grasslands and woodlands has been converted to a measure of fuel consumption via the method of Wooster et al. (2005). This is then compared to the pre-burn available fuel estimates, which have been derived from the burn scar area (as measured by manual mapping from MODIS level 1b 250 m spatial resolution NIR spectral reflectance imagery) and time integrated estimates of net primary production (NPP) made over the area of each burn scar during the prior growing season. The NPP data were obtained from the “geosuccess” portal, and are derived from use of SPOT-VGT spectral reflectance measures and a light use efficiency plant growth model ([www.geosuccess.net/geosuccess/relay.do?dispatch=NPP\\_info](http://www.geosuccess.net/geosuccess/relay.do?dispatch=NPP_info)). The ratio of the actual estimated fuel consumption to the available fuel consumption provides an estimate of the proportion of fuel combusted (*i.e.*, the “combustion completeness”) for this particular land cover type and time of year. As can be seen from Figure 2.3, the estimate of combusted biomass derived from SEVIRI is correctly below the estimate of available biomass for all fires examined.

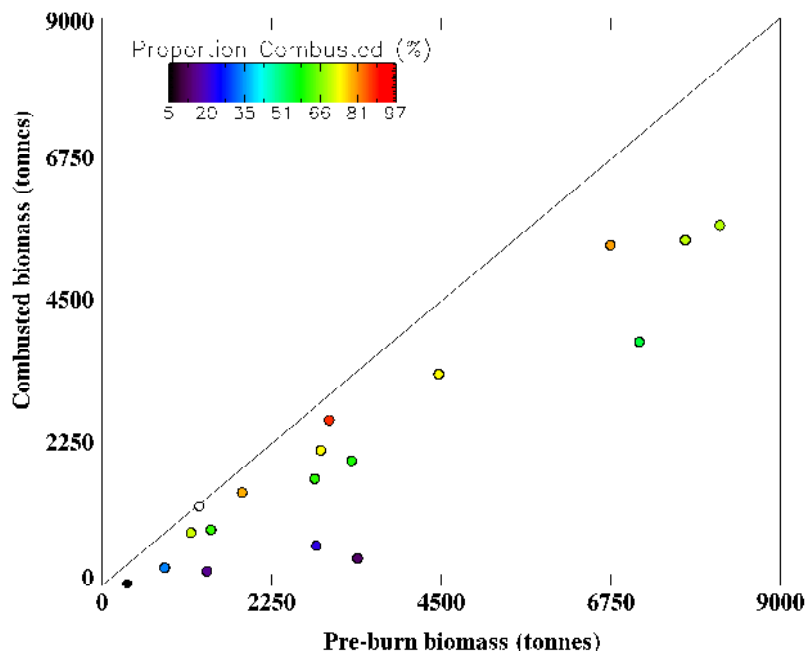


**Figure 2.3:** Estimates of SEVIRI FRP-derived biomass combustion as compared to the pre-burn fuel load for eighteen fires in southern African grasslands and woodlands. The latter was calculated from SPOT-VGT derived NPP data and burned area measures taken from MODIS. The ratio of the two provides an estimate of the proportion of available fuel combusted.



## 2.2 Requirements Analysis

The requirements of operational and scientific users of the FRP product can be categorized as follows:

- accuracy: what are the acceptable errors of omission and commission and what is the required accuracy of the derived FRP?
- resolution: is the relatively coarse spatial resolution of the SEVIRI MIR channel adequate for fire detection?
- measurement frequency: is the time interval of 15 minutes between SEVIRI scenes adequate to capture fire variability?
- data delivery and formats: how fast (timeliness) do users need the data and in which format should the data be provided?

Active fire products are by necessity subject to errors of omission and commission since at their heart is an anomaly detection procedure working on thresholding of image radiance and brightness temperature signals (Figure 1.1). This anomaly detection procedure will not successfully capture all pixels containing active fires, and will indeed very likely report some pixels where the supposed ‘anomaly’ is not caused by fire. Generally speaking, if an active fire product is made less sensitive in order to reduce false alarms (*i.e.*, errors of commission) then its errors of omission will very likely increase, so there is a balance to be struck. Giglio *et al.* (2003b) report the errors of commission of the widely used TRMM VIRS active fire product as, on average,  $\sim 10\%$  for a spatial resolution that provides  $4 \text{ km}^2$  pixels at nadir. The fire detection false alarm rate present in the SEVIRI FRP product should ideally be no higher than this, but the errors of omission are expected to be larger than for TRMM VIRS due to SEVIRI’s lower spatial resolution. It is difficult to formulate precise requirements for omission and commission errors, because the impact of such errors will depend on the application and its degree of aggregation and processing of the individual SEVIRI slot-level data products, and because the product errors are not independent of each other and one needs to find a balance between these errors so as to maximize the product usefulness. As a general rule, the level of fire detection omission for SEVIRI should be such that the fire pixels that it does successfully detect are responsible for the majority (*i.e.*  $> 50\%$ ) of the FRP actually being emitted at the time of observation (this can be verified via simultaneous use of a higher spatial resolution sensor, such as MODIS). Furthermore, the size spectrum of detected fires should ideally be unbiased (beyond a set lower FRP threshold) such that extrapolation of frequency – magnitude relations (Roberts *et al.*, 2003) can in theory be applied to estimate the frequency of ‘missing’ (undetected) low FRP fire pixels that are below the detection threshold.

In terms of the accuracy of the FRP observations made for the detected fire pixels, it is worth considering the theoretical optimum performance that can be achieved. The relatively high spatial resolution (370 m) BIRD sensor, that was designed specifically for active fire observations, and which was used by Wooster *et al.* (2003) in the derivation of the MIR FRP algorithm, is reportedly able to measure the FRP of around 75% of detected active fire pixels to within  $\pm 30\%$ , assuming perfect knowledge of the atmospheric transmissivity (Zhuckov *et al.*, 2005). It can be expected that SEVIRI

 	Land SAF VR-FRP	Doc: SAF/LAND/IM/VR_FRP/V_09 Issue: Version V/2009 Date: 18/10/2009
---	-----------------	---


with its coarser resolution and lower saturation temperature will yield somewhat larger errors than this. Since the accuracy is largely limited by the measurement of the background radiance that has to be determined from neighbouring pixels, it contains a random error term, which will decrease in relative magnitude when several fires are aggregated as in a gridded FRP product. Furthermore, as noted above, there are ways to improve estimates of total FRP within a grid cell if a correction for small fires escaping detection is applied (e.g. based on extrapolation of frequency magnitude statistics).

Finally, for the purpose of estimating combustion totals from SEVIRI data, one needs to consider that these are to be estimated as the time-integrated values of FRP, which will tend to reduce the impact of random error on each individual FRP observation. Specifically, it should be recognised that many applications are focused not on the use of per-slot FRP measures of individual fires or fire pixels, but on spatial and temporal aggregations of such measures so as to derive estimates of the overall amount of a chemical species emitted over a particular area and time (e.g. a 1 degree resolution spatial grid, over a 1 hr period) and as such the influence of random errors in FRP characterisation will be reduced in these applications via this spatial and temporal aggregation.

The spatial resolution requirements of the FRP product can be summarized as follows: for early detection and fire warning systems, it must be as high as possible – ideally, the fire position should be discernible within a few hundred metres. Nevertheless, even a coarser resolution product can be of use for these applications, in particular when it is delivered rapidly and with temporal sampling frequencies of less than 1 hour. Inclusion of fire data for emission estimates in global and regional modelling applications generally poses less stringent resolution requirements, although some regional models are run on grid scales of 5 km × 5 km or less.

Since fire characteristics are extremely variable, a high temporal sampling frequency is desirable, and it is clear that a geostationary platform offers great advantage in this respect. Due to the fact that in the past data with less than daily coverage has hardly been available, and even these data proved highly useful in the various applications of fire satellite observations, it may be premature to define strict thresholds for the temporal sampling frequency requirements. From the feedback we gathered from various users it certainly seems as if the 15-minute sampling frequency provided by SEVIRI is adequate, though for “emergency response” type applications the delay between the collection of the level 1.5 source data and receipt of the locational information on new actively burning fires should be kept to an absolute minimum.


Atmospheric composition forecasts and event warning applications require a timely delivery of fire data products, ideally within less than 15 minutes after sampling. Other applications, notably for model validation and carbon budget studies, have much less stringent or no specific timeliness requirements. It should be noted that there is presently hardly any fire data set covering Africa and Europe that is delivered operationally and in near realtime. Therefore, even if the 15-minute requirement cannot be strictly met, a regular near-realtime data product from SEVIRI would

	Land SAF VR-FRP	Doc: SAF/LAND/IM/VR_FRP/V_09 Issue: Version V/2009 Date: 18/10/2009
---	-----------------	---

improve the status quo and would be welcomed by all users. Data formats don't seem to be a major issue, but some users expressed wishes concerning the use of specific dissemination channels so that their access is guaranteed.

## 2.3 Requirement summary

The following Table summarizes the temporal, spatial and accuracy requirements that were expressed by various user communities. Note that in particular the spatial resolution requirements refer to the resolution used in the various applications. Fire detection and derivation of FRP generally require data with finer resolution than what the applications will use.

	Land SAF VR-FRP	Doc: SAF/LAND/IM/VR_FRP/V_09 Issue: Version V/2009 Date: 18/10/2009
---	-----------------	---

User community	User requirement				
	temporal resolution	spatial resolution	timeliness	accuracy	Notes
<b>GEMS<sup>1</sup></b>	15-60 min (3 hours)	25-50 km for global system, 5-50 km for regional air quality models	15-30 min after image acquisition (less than 6 hours)	25-50% error, aggregated within model grid box after correction for missing small fires	Access at ECMWF; includes reprocessing of past periods
<b>CPTEC-INPE</b>	1-2 hours (3 hours)	pixel - 50 km	30 min	as above	Access from Brazil; ftp access requested
<b>Visibility forecast</b>	1-3 hours	10 km	3-6h	<100% error	
<b>Carbon budget study</b>	daily integrals	1 deg	1 month	25-50% error, aggregated within model grid box after correction for missing small fires	Reprocessing of past SEVIRI observations
<b>fire climate model development</b>	3 hours	1degree	1 month	25-50% error, aggregated within model grid box after correction for missing small fires	Reprocessing of past SEVIRI observations
<b>SA FIS</b>	15 min	Pixel	asap (e.g. 15 min of end of slot)	Errors of omission and commission as low as possible, FRP uncritical	
<b>Emergency response</b>	15 min	Pixel	asap (e.g. 15 min of end of slot)	Errors of omission and commission as low as possible, FRP uncritical	

asap= as soon as possible

<sup>1</sup> this includes the GEMS follow-up project MACC and ultimately the GMES Atmospheric Service

**Table 2.1:** User requirements for operational use of the SEVIRI FRP product. Unless otherwise stated, the requirements should be seen as target requirements. Where a range is given, the lower value represents the optimal value and the upper value the target requirement. In cases where a clear threshold requirement can be identified, this is listed in paranthesis.

### 3. VALIDATION DATASET DESCRIPTION

The independent validation data came mainly from the MODIS active fire products, and specifically the fire detections recorded in the MOD14/MYD14 product (Justice *et al.*, 2002; Giglio *et al.*, 2003) collected by the MODIS sensors onboard the EOS Terra and Aqua satellites. Various study periods have been selected as described below. SEVIRI data was acquired from MSG-8 and MSG-9 and processed either at KCL, EUMETSAT or the Land SAF data processing centre. Radiative transfer modelling at KCL was performed using MODTRAN v4 (Berk *et al.*, 1999). Other datasets used in the validation were the Global Land Cover Map 2000 (GLC2000; Mayaux *et al.*, 2004) to prescribe landcover type. Validation of emission estimates and performance analysis in impact studies was done using the the Global Fire Emission Database (GFED) version 2 and the prototype version 3 (van der Werf *et al.*, 2006), and using the modelling systems at ECMWF (GEMS), the UK Met Office, and the Finnish Meteorological Institute (SILAM). The following sub sections describe these data sets in more detail and discuss some dataset features that are relevant for the SEVIRI FRP validation procedure.

#### 3.1 The MODIS MOD14 Data Set

The MOD14 product is a level 2 data product for thermal anomalies/fire derived from the Moderate Resolution Imaging Spectroradiometer (MODIS) instruments on EOS-Terra and EOS-Aqua (Justice *et al.*, 2002; Giglio *et al.*, 2003). A dataset description can be found on <http://edcdaac.usgs.gov/modis/mod14.asp>. For our analysis we used ver4 of the MOD14 product, and the fire detection abilities of these data in southern Africa have been independently assessed by Morisette *et al.* (2005) against high spatial resolution data from the 15 m – 90 m spatial resolution ASTER imaging radiometer which also flies on EOS Terra. Results from that study demonstrate the strong performance of the MODIS MOD14 fire detection algorithm, since when even when only relatively few 30 m spatial resolution ASTER-derived active fire pixels are present within the MODIS 1 km pixel recorded at the same moment, the MODIS active fire detection algorithm provides a high probability of detection [provided the ASTER fire pixels are distributed in a relatively spatially contiguous manner within the MODIS pixel, as measured here by Moran's I (Moran, 1950)]. When larger numbers of ASTER fire pixels are present within a MODIS pixel (e.g. > 100) the MOD14 product shows strong performance whatever the actual fire pixel spatial distribution at the scale of the ASTER observations.

The MOD14 product contains both a fire pixel mask, but also a near-complete record of the spectral characteristics of both the fire pixel and its neighbouring background pixels. It also contains an FRP record, though this is produced using a different algorithm to that implemented with SEVIRI and which takes no account of the spatially varying pixel size across the MODIS swath (in fact the MODIS algorithm



reports FRP in units of  $W/m^2$ ). For this reason, during the comparisons made herein, the FRP for each MODIS fire pixel detected by the MOD14 product, *i.e.*, using all confidence levels, was recomputed based on the same equation as for SEVIRI (Equation 1.1), as described in Wooster *et al.* (2005). Prior to comparisons to SEVIRI, the MODIS-derived FRP data were post-processed to remove the influence of duplicate fire detections in the original MOD14 mask due to the so-called MODIS ‘bow-tie’ effect that significantly affects far off-nadir views (see below explanation). The ability of MODIS to measure FRP to a set accuracy and precision has not yet been fully verified due to the difficulties of finding an independent data source covering different land cover and fire regimes. However, testing against BIRD high spatial resolution FRP data derived on a per-fire basis for forest fires in Australia indicated, on average, that the MODIS FRP measure was within 25% of the near-contemporaneously recorded BIRD FRP measure (Wooster *et al.*, 2003). The main reason for the differences were identified as (i) the fact that the MODIS fire detection algorithm failed to identify some parts of the individual fronts of each fire that BIRD successfully managed to detect by virtue of its higher spatial resolution, and (ii) the small time delay, of the order to minutes, between the MODIS and BIRD observations of each fire.

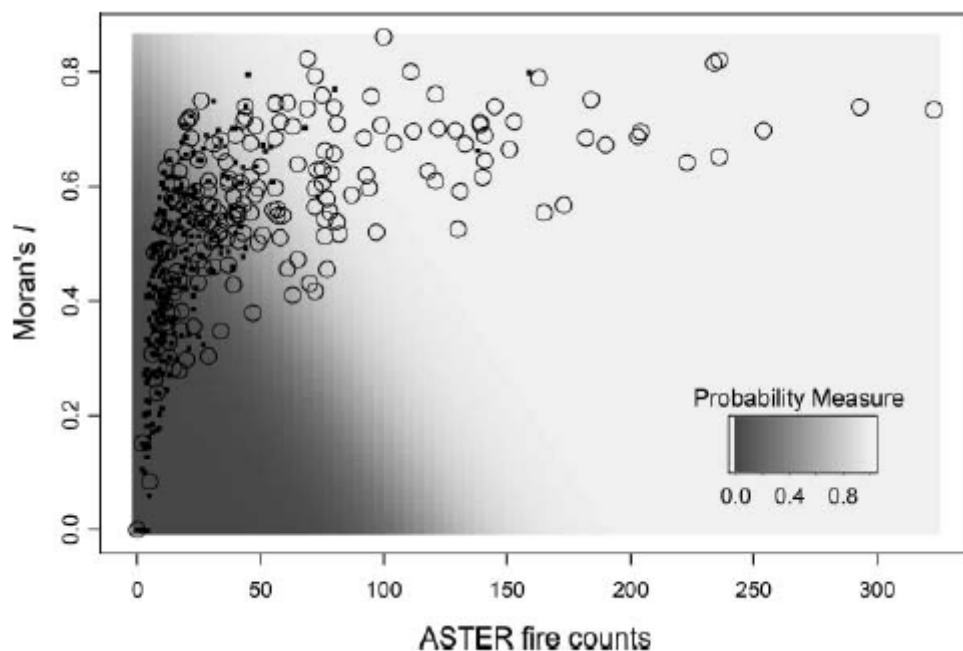


**Figure 3.1:** Estimated detection probabilities of a 1 km MODIS active fire pixel, calculated as a function of the number of 30 m ASTER active fire pixels it contains, and the spatial distribution of those ASTER active fire pixels (as expressed by Moran's I). Taken from Morissette *et al.* (2005).



### 3.2 Dataset Used to Investigate Algorithm Assumptions

Numerical simulations using calculations of the spectral radiant energy emissions resulting from bodies of different temperatures, and with atmospheric components of the signal calculated using MODTRAN v4, were used as the primary data to investigate the algorithm assumptions, following in part the methodology adopted previously by Wooster *et al.* (2005) but expanding this to provide an uncertainty estimate for each per-pixel FRP record. Additional data used to parameterise these numerical simulations consisted of radiances recorded in the SEVIRI level 1.5 data product, atmospheric transmissivity values calculated via radiative transfer modelling made at EUMETSAT, and example per-pixel FRP products processed with the KCL and Land SAF data processing chains.

### 3.3 Dataset Used to Investigate Per-Fire Comparisons

For the purpose of the per-fire intercomparisons, all the MODIS active fire pixel detections from over 800 individual MODIS active fire products were used. The data were MOD14 (EOS Terra) and MYD14 (EOS Aqua) Level 2 Active Fire Products (Giglio *et al.*, 2003) covering Africa for the matching period of 2004-05 and were obtained through the EOS Data Gateway at the Land Processes Distributed Active Archive Center (LP DAAC). This represents all the active fire pixel detections made by MODIS over Africa in February, May and August 2004, during which time continental-scale fire activity shifted southwards from Senegal and Ethiopia (February) to southern Africa (August). Matching SEVIRI data processed through the KCL data processing chain were selected as those taken within  $\pm 6$  minutes of the MODIS overpass, and all such matchups were used in the comparison process.

As mentioned above, prior to the inter-comparison, MOD14 fire detections were post-processed to remove the influence of the ‘bow-tie’ effect, an artifact of the MODIS design that results in off-nadir areas being imaged more than once in successive scans (Wolfe *et al.*, 2002). Double-counted, off-nadir fire pixels were identified using their recorded latitudes and longitudes, and the duplicates removed. The FRP for each remaining fire pixel was then calculated using the MIR radiance method of Wooster *et al.* (2003), applying the MIR radiance method algorithm coefficients presented in Wooster *et al.* (2005) for use with MODIS data and taking account of the changing MODIS pixel area across the swath.

### 3.4 Dataset Used to Investigate Effects of Spatial Resolution

SEVIRI data obtained from EUMETSAT between February 1<sup>st</sup>, 2004 and January 31<sup>st</sup>, 2005 from MSG-8 were used to investigate this issue. With the exception of a few, spurious failures in data acquisition, all images of the full Earth disk at 15-minute temporal resolution were processed over this one-year period. As stated previously, the algorithm used was the KCL geostationary fire detection and characterisation algorithm defined in Robert and Wooster (2008). This algorithm forms the bases (with only minimal changes) of the operational FRP algorithm

defined in the ATBD (Govaerts *et al.*, 2007). Only the continent of Africa, including Madagascar, was processed since the algorithm has been optimised for this area, and the vast majority (> 95%) of the biomass burning covered by the imagery was located on the African continent. The active fire detection algorithm uses i.) a novel high spatial resolution cloud mask derived from thresholding of the HRV channel data to supplement the cloud processing scheme of the Meteorological Product Extraction Facility (MPEF) at EUMETSAT (Lutz *et al.* 2003), ii.) a preliminary detection stage with liberal thresholds to identify the maximum number of potential fire pixels, iii.) multiple subsequent stages to minimize false detections due to large uniform areas of warm ground, and sun glint from water bodies or undetected clouds, iv.) a stage to reject potential fire pixels based upon their proximity to a cloud or water body, and v.) a stage to statistically compare the elevated thermal signal of a potential fire pixel relative to the surrounding background.


On average four MODIS swaths per day subtended some portion of the African continent, depending on the exact ground tracks of the polar orbiting, sun-synchronous AQUA and TERRA satellites that carry the MODIS instrument. The fire detections made by MODIS and contained within the aforementioned MOD14/MYD14 active fire products obtained for the same one year time period (February 1<sup>st</sup>, 2004 and January 31<sup>st</sup>, 2005) from the LP DAAC were used to identify fire pixels, and for each active fire pixel FRP was calculated via the MIR radiance method, taking account of the MODIS pixel area variation across the swath as described above and in Wooster *et al.* (2005).

### **3.5 Dataset Used to Investigate Effect of SEVIRI Sensor Characteristics and Level 1 to 1.5 Pre-Processing Operations**

A key dataset used here was that from a dedicated SEVIRI Fire Radiative Power (FRP) test (so-called SEVIRI ‘special operations mode’) conducted to collect data for an evaluation of the errors inherent in the FRP product due to the SEVIRI standard configuration. In order to do this the following configuration changes were made to Meteosat-8, and co-incident Meteosat-8 and 9 data collected over the duration of the test period (3- 7 September 2007):

- a. Change to SEVIRI Rapid Scan (5 minute temporal resolution) for a latitude range covering 0° to 30° S
- b. Change the digital filter coefficients to a top hat function instead of the standard finite impulse response filter
- c. Reduce the gain for for the 3.9  $\mu\text{m}$  channel to allow measurement up to pixel brightness temperatures of ~375 K without sensor saturation.

In addition to exploitation of the data from the above SEVIRI ‘special operations mode’ experiment, the dataset used for this study consisted of a small set of co-incident level 1.0 and 1.5 SEVIRI data obtained over Africa for large fires recorded by Meteosat-9, together with a BIRD Hotspot Recognition Sensor image of southern

	Land SAF VR-FRP	Doc: SAF/LAND/IM/VR_FRP/V_09 Issue: Version V/2009 Date: 18/10/2009
---	-----------------	---

Africa recorded in 2003 and which contained a series of active fire observations that provided data from which model simulations were derived. Characteristics of the BIRD HSRS imager can be found in Wooster *et al.* (2003) and Zhuckov *et al.* (2005), with the most relevant aspects to this study being the provision of non-saturated MIR channel data at fairly high spatial resolution (370 m pixel size) over even the most intensely burning fires.



### 3.6 Datasets Used in Impact Studies

#### 3.6.1 Global Fire Emissions Database (GFED)

The SEVIRI-FRP derived fire emission estimates for Africa are compared to the published inventory of the Global Fire Emissions Database (GFED) version 2 (van der Werf *et al.*, 2006). The GFED dataset was compiled using fire satellite data from different sources and the Carnegie-Ames-Stanford Approach (CASA) biogeochemical model. Burned area measures for 2001-2004 were derived from the aforementioned MOD14/MYD14 MODIS active fire ('hot spot') data which were calibrated using MODIS 500m burned area estimates for selected regions (Giglio *et al.*, 2006). ATSR (Along Track Scanning Radiometer) and VIRS (Visible and Infrared Scanner) satellite data were used to extend the burned area time series back to 1997 based on simple linear regression between the time periods when both products overlapped (Arino *et al.*, 1999; Giglio *et al.*, 2003; Van der Werf *et al.*, 2006). Fuel loads and net flux from terrestrial ecosystems were estimated as the balance between net primary production, heterotrophic respiration, and biomass burning, using time varying inputs of precipitation, temperature, solar radiation, and satellite-derived fractional absorbed photosynthetically active radiation.

The current version, GFED version 2, is freely available for download from <http://www.geo.vu.nl/users/gwerf/GFED/index.html>. The dataset consists of 1°×1° gridded monthly burned area, fuel loads, combustion completeness, and fire emissions (Carbon, carbon dioxide (CO<sub>2</sub>), carbon monoxide (CO), methane (CH<sub>4</sub>), non-methane hydrocarbons (NMHC), hydrogen (H<sub>2</sub>), oxides of nitrogen (NO<sub>x</sub>), nitrous oxide (N<sub>2</sub>O), particulate matter smaller than 2.5 µm diameter (PM<sub>2.5</sub>), total particulate matter (TPM), total carbon (TC), organic carbon (OC), black carbon (BC)). Emission estimates for the 2001 – 2006 period are also available with an 8-day time step.

For the comparison with SEVIRI-based biomass burning estimates, data from the preliminary ver3 GFED database are also included, because processing newly available burned area data has revealed relatively large changes in Africa [with less burned area (compared to version 2) for northern Africa and more in southern Africa]. For the comparisons presented in section 0, the GFED version 2 emission estimates were therefore scaled with the ratio between burned area from version 2 and 3 in order to produce a prototype GFED ver3 emissions estimate. The final version 3 will include other important changes, so that the GFED ver3 emissions presented here should be considered a preliminary data set only.

 	Land SAF VR-FRP	Doc: SAF/LAND/IM/VR_FRP/V_09 Issue: Version V/2009 Date: 18/10/2009
---	-----------------	---

### 3.6.2 Global GEMS Model


The Global and regional Earth-system Monitoring using Satellite and in-situ data (GEMS) project is combining the manifold expertise in atmospheric composition research and numerical weather prediction of thirty-two European institutes to build a comprehensive monitoring and forecasting system for greenhouse gases, reactive gases, aerosol, and regional air quality (Hollingsworth *et al.*, 2008). The project is funded by the European Commission as part of the Global Monitoring of Environment and Security (GMES) framework.

As part of the GEMS project, prognostic representations of aerosols and greenhouse gases are being developed in the ECMWF Integrated Forecast System (IFS), in both its analysis and forecast modules. An experimental version of the global forecast model now accounts for five tropospheric aerosol types (i.e. sea-salt, desert dust, organic matter, black carbon and a sulphate related variable), carbon dioxide and methane. The sources for all species are located at the surface. The species are advected and included explicitly in the vertical diffusion and mass-flux convection schemes. The greenhouse gases have sinks at the surface only, while the aerosols undergo sedimentation and dry and wet deposition by large-scale and convective precipitation (Morcrette *et al.*, 2008). Feedbacks of the aerosol and greenhouse gas fields on other atmospheric variables are not included in the current model version.

Biomass burning emits carbon dioxide, methane, organic matter, black carbon, and sulphate and some of its precursors. The global GEMS system currently accounts for these emissions using the aforementioned retrospective inventory GFED version 2, that has a temporal resolution of 8 days (van der Werf *et al.*, 2006). However, this approach is only a temporary solution. In the operational phase, more and better fire observations need to be acquired in near realtime and assimilated to obtain accurate atmospheric composition estimates (Kaiser *et al.*, 2006). For the impact studies described in this report (section 0) the SEVIRI FRP product was used to provide a greatly improved temporal resolution over the observed areas, and GFED ver2 provided the source terms outside of the SEVIRI-observed regions of Africa and Southern Europe. The latest information on the GEMS system can be found on the project home pages at [http://www.ecmwf.int/research/EU\\_projects/GEMS/index.jsp](http://www.ecmwf.int/research/EU_projects/GEMS/index.jsp).

### 3.6.3 SILAM Dispersion Model and Fire Assimilation System at FMI

The Finnish Meteorological Institute (FMI) is producing regional PM<sub>2.5</sub> aerosol concentration forecasts with the SILAM dispersion model driven by emissions calculated with the FMI Fire Assimilation System (FAS). The FMI FAS is based on fire observation products over Northern Europe from the MODIS instrument. It uses the products of either temperature anomaly (TA) [K] or fire radiative power (FRP) [W], both with a temporal resolution of one day. Calibration of both FAS versions was started from literature data, *e.g.*, Ichoku and Kaufman (2005). Then the emission factors were fine-tuned using a model-based approach. Namely, FMI took a few fire cases, primarily in 2006, estimated their emissions of PM<sub>2.5</sub>, ran the SILAM dispersion model and compared total column loads and near-surface concentrations

	Land SAF VR-FRP	Doc: SAF/LAND/IM/VR_FRP/V_09 Issue: Version V/2009 Date: 18/10/2009
---	-----------------	---

with available observations. The systematic deviation was eliminated via adjustment of the emission factor. More information on SILAM can be found at <http://silam.fmi.fi>.

### 3.6.4 MOPITT Atmospheric Carbon Monoxide Concentration Data

Carbon Monoxide column concentrations, and vertical profiles, are provided by the Measurements of Pollution in the Troposphere (MOPITT) instrument on EOS Terra ([http://terra.nasa.gov/About/MOPITT/about\\_mopitt.html](http://terra.nasa.gov/About/MOPITT/about_mopitt.html)). MOPITT is an 8-channel nadir infrared instrument with a 22 km pixel spatial resolution designed to detect trace gas signals of carbon monoxide (CO) and methane (CH<sub>4</sub>) in the troposphere. Via the application of different weighting functions, CO vertical profiles can be retrieved for independent levels within the atmosphere.

For the impact study presented in section 0, MOPITT level 3 (ver 3) data derived via averaging the daily level 2 product into a global 1°×1° dataset and obtained from the NASA Langley DAAC ([http://eosweb.larc.nasa.gov/PRODOCS/mopitt/table\\_mopitt.html](http://eosweb.larc.nasa.gov/PRODOCS/mopitt/table_mopitt.html)) were used. The MOPITT level 3 data contain retrieved CO profiles for seven pressure levels, day / night total column CO concentration and various quality indicators. Following the filtering approach implemented by Hyer *et al.* (2007), the ‘percent *a priori*’ quality indicator is used to filter out retrievals which were composed of greater than 40% of *a priori* profile. In addition to this, only daytime cloud free (as determined from the MOPITT cloud mask) land pixels are used in the analysis.

## 4. SPECIFIC VALIDATION METHODOLOGY

### 4.1 Algorithm Performance Analysis


As explained in Section 0, the following assumptions are made in the FRP algorithm derivation and application of the approach in the SEVIRI FRP product:

- i. Over the temperature range relevant to active fires, Planck's radiation law is well approximated by a fourth order power law in the 3.4–4.2 $\mu$ m interval (as implied in the derivation of the scaling factor  $a$  of Equation 1.1, shown in Section 0,).
- ii. The approximations made during the derivation of the equation to estimate the fires contribution to the fire pixels MIR spectral radiant emission (Equation 1.6) are valid.
- iii. The background MIR radiance signal of the fire pixel can be appropriately estimated from analysis of the neighbouring non-fire, non-cloudy pixel group. At present the mean spectra radiance of this pixel group is used.
- iv. The effects of aerosols and trace gases (beyond those in the ambient atmosphere) are not taken into account, and the atmospheric transmissivity assumed in the application of the algorithm is a reasonable estimate of the true atmospheric transmission in the 3.4 – 4.2 $\mu$ m interval.

In addition, it is assumed that the fire (and background) thermal emission is isotropic and that the fire behaves as a grey body. These assumptions (or indeed, quite commonly the even more stringent assumption that the fire is a blackbody) are made in all existing applications deriving fire radiative power, and cannot be easily checked without detailed field experiments that have not been carried out. They will therefore not be addressed here.

The investigation of the theoretical FRP algorithm performance analysis was based around an analysis of these assumptions and a sensitivity study of the FRP algorithm. The effect of assumption (i) above (the fourth order power law approximation) was analysed by first comparing FRP derived using Equation 1.1 to that derived from the true Stefan Boltzmann Law. The effect assumption (ii) was investigated using a radiative transfer modelling study simulating the radiances measured over sub-pixel sized fires observed from space, and then using these within Equation 1.1 to estimate the fires FRP using the equations applied during the SEVIRI FRP processing chain. These estimates were then compared to the true fire FRP calculated using the Stefan Boltzmann Law. Finally, the impact of uncertainty in the background radiance field, and in the atmospheric parameters (assumptions iii and iv), was considered using a sensitivity study that perturbed these values prior to incorporation into within FRP algorithm. The appropriate range of atmospheric transmissivity in the 3.4 – 4.2  $\mu$ m interval (that covered by the SEVIRI MIR spectral



	Land SAF VR-FRP	Doc: SAF/LAND/IM/VR_FRP/V_09 Issue: Version V/2009 Date: 18/10/2009
---	-----------------	---

band) was taken from the ATBD (Govaerts *et al.*, 2007), and was assumed to vary over the range 0.61 – 0.7 [mid-range value of 0.66]. Expected uncertainties in the MIR background window pixel signal, and the difference between this and fire pixel background, were taken from SEVIRI level 1.5 data and LandSAF FRP products covering the southern African region.

## 4.2 SEVIRI Product Performance Analysis



### 4.2.1 Per-Fire Comparisons

Assessment at the scale of individual fires was performed via a comparison to the aforementioned MODIS active fire observations identified by the MOD14 and MYD14 MODIS level 2 fire products. MODIS is the sensor for which the measurement of fire radiative power was first proposed as a mean of classifying a fire emission source strength (Kaufman *et al.*, 1998).

The analysis was conducted at the scale of individual fires (*i.e.*, clusters of separately identified fire pixels) using data from eight MODIS MOD14/MYD14 products (6 days and 2 nights) from February and August 2004, together with fire detections extracted from the SEVIRI-derived KCL FRP dataset within 6 minutes of the MODIS acquisition time<sup>1</sup>. The MIR radiance method algorithm (Equation 1.1) was used to derive the FRP measure of each fire pixel detected by the sensors. The approach followed that first used by Wooster *et al.* (2003) and Roberts *et al.* (2005), clustering groups of spatially contiguous fire pixels in the primary dataset into single ‘fires’ whose total FRP for that imaging slot was then derived, and using the latitude and longitude range of that fire pixel cluster (expanded by the equivalent of two SEVIRI pixels to account for any geo-locational offsets) to check for the presence of the same fire pixel cluster in the reference dataset.

In most cases a fire would be expected to be represented by more fire pixels in the MODIS dataset than in the SEVIRI dataset, due to the higher spatial resolution of the MODIS observations. Comparison of fire detections made by MODIS and SEVIRI allowed for an assessment of the errors of commission (false alarms) and omission (missed fires). When both datasets successfully recorded the presence of the same fire, the total FRP of the fire as recorded by both sensors was compared to assess the ability of SEVIRI to characterise the full FRP of each fire detected.

<sup>1</sup> The SEVIRI acquisition time is 12 minutes and so every MODIS fire pixel will be observed by SEVIRI a maximum of 6 minutes before or after. Since some fires will get more intense and others less intense between the two sensors “simultaneous” observations, the FRP difference induced by the maximum 6 min time difference should be random rather than in any one direction, and thus the time difference is not expected to introduce bias in the comparison (but it maybe responsible for a large part of the scatter between the data from the two sensors).

 	Land SAF VR-FRP	Doc: SAF/LAND/IM/VR_FRP/V_09 Issue: Version V/2009 Date: 18/10/2009
---	-----------------	---

#### 4.2.2 Effect of Spatial Resolution - Area Based Comparisons

SEVIRI has a nominal sampling distance at the sub-satellite point of 3 km, and a spatial resolution of 4.8 km, the values increasing with distance away from the sub-satellite point. This spatial resolution is relatively coarse compared to most other imaging radiometers currently used for active fire detection and characterisation, most notably the polar-orbiting MODIS sensor which as mentioned previously has a nominal  $1 \text{ km} \times 1 \text{ km}$  spatial resolution at the sub-satellite point (increasing to  $\sim 2 \times 10 \text{ km}$  at the swath edge). Detectability of a fire within a cloud-free pixel depends primarily on the MIR spectral radiance signal increase of the ‘fire pixel’ above that of the surrounding (background) non-fire pixels and/or above the signal of the same pixel in another spectral channel less affected by the presence of sub-pixel fires (e.g. a longer wavelength TIR channel). These signal increases ultimately depend on (i) the fires effective emitter temperature, and (ii) the effective proportion of the pixel covered by this elevated emitter temperature. These two properties also determine the fires FRP through the Stefan-Boltzmann Law, and so for any particular fire detection algorithm criteria (e.g. a required MIR brightness temperature increase of the fire pixel above that of the ambient background) the corresponding minimum-detectable fire can be calculated in terms of its FRP.

shows this calculation for the SEVIRI sub-satellite point over a temperature range wider than that which is assumed valid for open vegetation fires ( $\sim 650 - 1300 \text{ K}$ ). It indicates that SEVIRI should be able to confidently detect actively burning fires whose FRP reaches a minimum of around 100 MW, and in certain cases maybe able to detect fires whose FRP is even lower than this, down to around 50 MW. Conversely, the calculation also suggests that SEVIRI will saturate over fire pixels whose FRP is greater than around 900-1000 MW.

The calculations presented in do not take into account any impact of the finite impulse response (FIR) filter applied in the production of the Level 1.5 SEVIRI data, nor the true SEVIRI pixel oversampling (by a factor 1.6) which is taken into account of during the FRP algorithm application via a reduction in assumed SEVIRI pixel area by the appropriate oversampling factor in the x and y directions (Govaerts *et al.*, 2007). Taking these factors into account would lead to minimum FRPs returned by the fire detection algorithm when applied to real SEVIRI Level 1.5 data of the order of  $\sim 40 \text{ MW}$  (and at the extreme  $\sim 20 \text{ MW}$ ) at the sub-satellite point, whilst maximum retrieved FRP would be expected to be of the order of 400 MW. These values will increase linearly with pixel area away from the sub-satellite point, and indicates that FRP retrievals from real SEVIRI data shows a statistical distribution consistent with this modelling. In Figure 4.2, the small number of fires pixels having  $\text{FRP} > 400 \text{ MW}$  are the result of fire detections at pixels well away from the sub-satellite point, and thus which are able to record FRP values higher than is possible at that location.



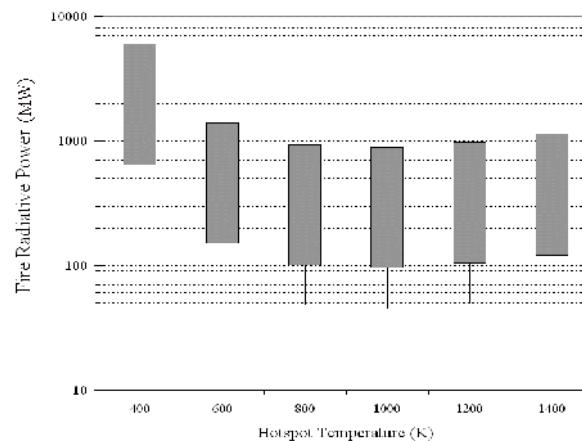



**Figure 4.1:** Estimated FRP range detectable for various fire temperatures using SEVIRI at the sub-satellite point. Minimum detectable FRP is shown by the vertical line extending below the bar (fire pixel MIR brightness temperature raised 3 K above the background temperature). The lower limit of the black bar indicates the minimum detectable FRP when this threshold is raised to 6 K. The per-pixel FRP that saturates the sensor is shown by the upper limit of the black bar. FRP is calculated in each case by parameterising the Stefan-Boltzmann Law with the relevant fire temperature and area, and is relatively consistent across the assumed fire temperature range since these parameters are inversely related for a particular fire pixel brightness temperature. Calculations were performed using the MODTRAN radiative transfer code (Berk et al., 1999) and assume a mid-latitude summer atmosphere (rural aerosol, 23 km visibility), with a fixed surface reflectance (0.15) and emissivity (0.85) and a daytime solar zenith angle of 20°. Results differ between day and night due to differing assumed ambient background temperatures (day: 300 K, night: 285 K) and the lack of a solar reflected radiation contribution in the latter case.

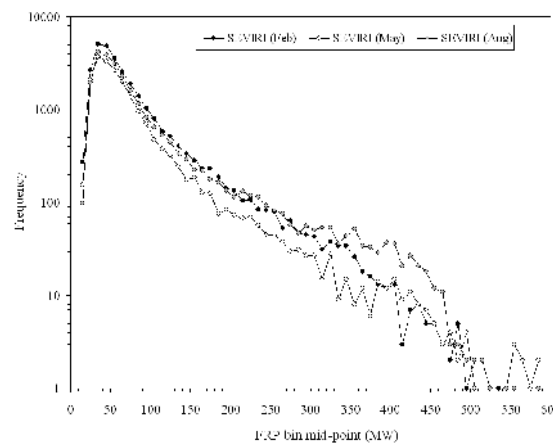


**Figure 4.2:** Frequency-magnitude of per-pixel FRP derived from SEVIRI active fire detections, binned into 10 MW intervals. Data are all SEVIRI fire pixel detections made across Africa using the KCL algorithm over the periods February, May, and August 2004. Only SEVIRI images matching the MODIS overpass time and swath were used to produce this plot, since the same data are used later to compare to MODIS. The vertical dotted line indicates the 40-50 MW threshold, indicated by modelling as the approximate minimum fire FRP that can be confidently detected by SEVIRI. Here the frequency of fire pixels with an FRP lower than this is significantly reduced, and thus these data are in accordance with that prediction.


	Land SAF VR-FRP	Doc: SAF/LAND/IM/VR_FRP/V_09 Issue: Version V/2009 Date: 18/10/2009
---	-----------------	---

In contrast to SEVIRI, the much higher spatial resolution MODIS sensor can detect fire pixels whose FRP values are as low as 7 - 10 MW. From this analysis, it is very clear that SEVIRI will fail to detect some fire pixels that MODIS can detect.

Whilst such low FRP fire pixels are each themselves responsible for only a small amount of the total emitted FRP of an area, Figure 4.2 confirms that the statistical distribution of per-pixel FRP is skewed towards low FRP fire pixels. For this reason, the overall FRP underestimation resulting from SEVIRI's inability to detect the lowest FRP fire pixels can be substantial.

The degree of regional-scale underestimation inherent in the SEVIRI data products is, however, slightly more complex than can be gauged by simply applying a minimum FRP detection threshold to a set of MODIS-derived FRP data in order to determine which fires SEVIRI would detect and which it would not. This is because individual MODIS-detected fire pixels, that each may have a lower FRP than the SEVIRI FRP detection threshold, may still in fact have their FRP characterised by SEVIRI if they are arranged spatially such that a sufficient number of them contribute to the signal of one SEVIRI pixel (and thus result in a per-pixel FRP measure higher than the SEVIRI minimum FRP detection threshold). For this reason, the best way of gauging the impact of the effect of SEVIRI's lower spatial resolution on regionally aggregated FRP measures is to directly compare simultaneously-derived MODIS and SEVIRI active fire detections and FRP retrievals, with the assumption that the MODIS-derived record represents the true representation of the regionally-aggregated FRP from all fires burning in the area.

It was expected that the degree of underestimation inherent in the SEVIRI-derived FRP measures might vary in space and time, due for example to changes in the FRP frequency-magnitude relationship over burning season (e.g. from early to late dry season). For this reason, the magnitude of the FRP underestimation inherent in the regional-scale SEVIRI-derived FRP measures was investigated spatially over the entire continent of Africa for the period Feb 2004 - Jan 2005, using the KCL derived FRP dataset and a matching MODIS-derived dataset extracted from the year-long MOD14/MYD14 archive of the same area. This investigation has particular relevance to the proposed production of a SEVIRI-derived FRP gridded product at 5.0 degree grid resolution and which is proposed to best represent the mean FRP emitted by all fires in each cell averaged over one hour intervals (Govaerts *et al.*, 2007). In this dataset, the SEVIRI-derived FRP signals within each grid cell would ideally be adjusted to the value that MODIS would have seen had it been the observing instrument (remembering that the advantage of actually using SEVIRI rather than MODIS is that it provides data at a very much higher temporal resolution than MODIS, and which is in theory available in near-real time for use in the derivation of short- to medium-term atmospheric forecasts). For this reason, potential methods to adjust the proposed SEVIRI-derived FRP gridded product for the expected effects of FRP underestimation were also implemented, and their efficacy assessed via testing with an independent MODIS- and SEVIRI-derived FRP match up dataset collected between May 2008 and April 2009.

	Land SAF VR-FRP	Doc: SAF/LAND/IM/VR_FRP/V_09 Issue: Version V/2009 Date: 18/10/2009
---	-----------------	---

### Basic Approach

Regional scale FRP comparisons were first conducted by comparing the cumulative (aggregated) within-scene FRP observed near simultaneously by SEVIRI and by MODIS over the area equivalent to the full MODIS swath and latitudinal image extent, together with visual examinations of the active fire pixel detections made across key-fire affected regions of Africa. This analysis used data from three separate months of 2004 where fires were predominately located in North Africa (February), Central Africa (May) and Southern Africa (August). As will be shown in section 0, this analysis established a substantial difference between the MODIS and SEVIRI area based FRP measures in all regions, and one that varied in time/space, and so confirmed the need for a more complete investigation covering the full year of continent-wide data.

This longer-term investigation again used a ‘validation dataset’ consisting of active fire detections made only with near-simultaneous SEVIRI and MODIS fire pixel and FRP observations collected over the same geographic extent. Fire pixels reported by the MOD14 and MYD14 MODIS products were temporally subset to within  $\pm 6$  minutes of a SEVIRI scan, and this time were also spatially subset to include only those detected within the center two-thirds of the MODIS swath, specifically between columns 225 and 1129, in order to reduce any effect introduced by the very large MODIS pixel areas that are found towards the edges of the MODIS swath. As previously mentioned, at these locations the MODIS “bowtie effect” (Wolfe, 2002) is known to (i) induce multiple, overlapping detections for a single fire occurrence, (ii) reduce the absolute number of detections at extreme view angles since an elevated thermal signal is required to overcome the increased ground sampling area, and (iii) as a consequence of (ii), produce fire pixels with mean FRP values significantly greater than those interior to the swath. Conversely, fire pixels detected by SEVIRI were temporally subset to only those within  $\pm 6$  minutes of a MODIS overpass, and also spatially subset to a convex hull encompassing the MODIS-detected fire pixels within the centre 2/3<sup>rd</sup>s of the MODIS swath. Given that SEVIRI is less responsive than MODIS to the lower FRP fire pixels that sometimes exist along a fires’ perimeter, the potential number and intensity of SEVIRI fire pixels lying outside a convex hull of MODIS fire pixels was considered negligible.

If there were insufficient MODIS fire pixels to perform a convex hull operation (e.g., if there only existed one or two MODIS fire pixels in a scene) then a 2 km square buffer around the identified MODIS fire pixels was used instead of the convex hull. The procedure for subsetting all SEVIRI and MODIS data to concurrent and collocated fire pixels essentially imposed the temporal resolution and spatial coverage of MODIS onto the SEVIRI temporal cycle and spatial extent -- as is demonstrated in Figure 4.3. For brevity, this temporal and spatial subset of the combined SEVIRI and MODIS fire products across Africa in 2004/05 is hereafter referred to as the “training dataset.”

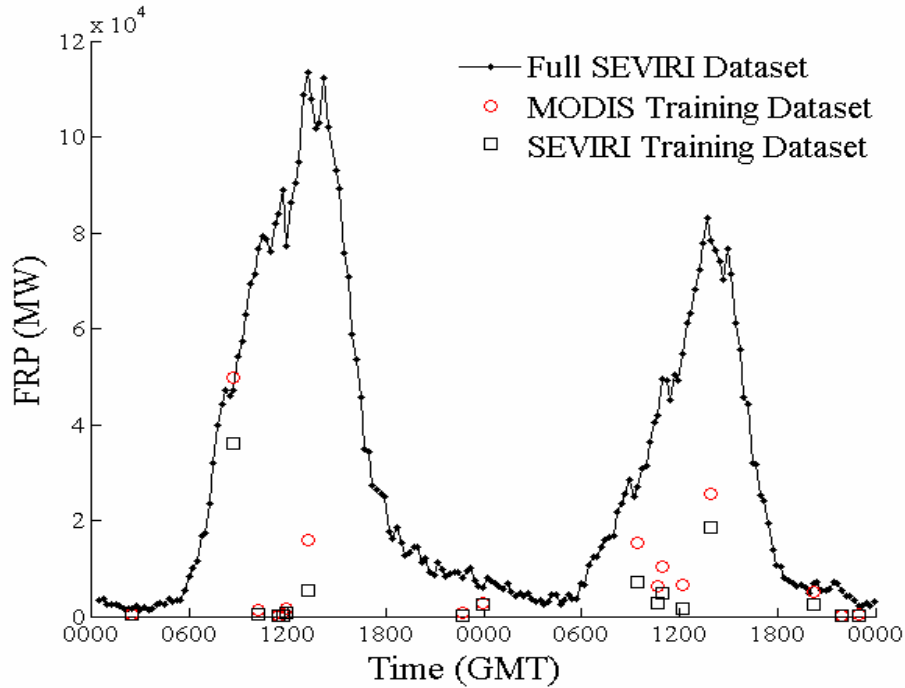


**Figure 4.3:** Temporal profile of FRP measured by SEVIRI and MODIS over two consecutive days. The full SEVIRI dataset (—) contains fire pixels at continental coverage and 15-minute temporal resolution. Observations in the training dataset for SEVIRI ( ) and MODIS ( ) are composed of concurrent and collocated fire pixels within the center 2/3<sup>rd</sup>s of a MODIS swath.

#### Detailed Sensor-to-Sensor Comparisons of Fire Activity Over the Annual Cycle

Sensor-to-sensor comparisons were performed by calculating the SEVIRI to MODIS ratios of both total fire pixel counts,  $\phi_{count}$ , and total FRP,  $\phi_{FRP}$ . Within the training dataset, the yearly ratios of total fire count and total FRP were calculated simply by summing the number of individual fire pixels and their respective FRP, then dividing the SEVIRI totals by the MODIS totals. This provided the base information of the extent to which SEVIRI underestimates fire pixel count and FRP with respect to MODIS, and how this varies seasonally.

To assess the effects of temporally aggregating the fire pixels,  $\phi_{count}$  and  $\phi_{FRP}$  were calculated in discrete, non-overlapping intervals of one-day, one-week, and four-weeks beginning from the time of the first observation. Widening the temporal window essentially expanded the number of samples available to calculate  $\phi_{count}$  and  $\phi_{FRP}$ . Ratios of fire pixel counts and FRP were assigned timestamps corresponding to the centre of each temporal window such that:

$$\phi_{FRP}\left(t + \frac{\Delta t}{2}\right) = \frac{\sum_{i_{SEVIRI}=1}^{n_{SEVIRI}} FRP_{i_{SEVIRI}}}{\sum_{i_{MODIS}=1}^{n_{MODIS}} FRP_{i_{MODIS}}} \quad \text{Equation 7}$$

where  $t$  is the serial time at the beginning of the day, week or four-week interval,  $\Delta t$  is the duration of the interval,  $i_{SEVIRI}$  and  $i_{MODIS}$  are indices of the fire pixels detected by each sensor,  $n_{\Delta t}$  is the total number of fire pixels detected by each sensor within the respective interval, and  $FRP$  is the fire radiative power associated with each fire pixel. The ratio of fire pixel counts,  $\phi_{count}$ , is simply the values of  $n_{\Delta t}$  for SEVIRI divided by that for MODIS.

Since fire activity varies with the season, as well as with ecoregion and land use, the patterns of  $\phi_{count}$  and  $\phi_{FRP}$  were also mapped spatially. For comparison, the full continent of Africa was gridded at  $5.0^\circ$ ,  $1.0^\circ$  and  $0.25^\circ$  grid cell resolutions. Spatially explicit yearly ratios of count and FRP were calculated by summing all concurrent and collocated fire pixels detected in a single grid cell throughout the year, and again then dividing the SEVIRI totals by the MODIS totals within each grid cell.

#### Potential Adjustment of SEVIRI Gridded FRP Data for the Effect of Undetected Fires

Statistical distributions of FRP measured by SEVIRI suffer from left-hand truncation due to the inability of the sensor and active fire detection algorithms to reliably distinguish low FRP fires, an effect illustrated in Figure 4.3 above. Figure 4.4 shows the effect of this truncation on the FRP frequency-magnitude distributions obtained from the matched SEVIRI and MODIS training dataset, and it can be seen that the distribution here is in agreement with that of full SEVIRI data set displayed in Figure 4.2. It also confirms that for MODIS, the minimum FRP detection threshold for reliably detected fire pixels is  $\sim 7 - 10$  MW. Right hand truncation of the distributions is also seen, and this is due to the effects of sensor saturation occurring at a lower FRP for SEVIRI than for MODIS due to the low gain, high saturation temperature of the MODIS MIR channel (Kaufman *et al.*, 1998).

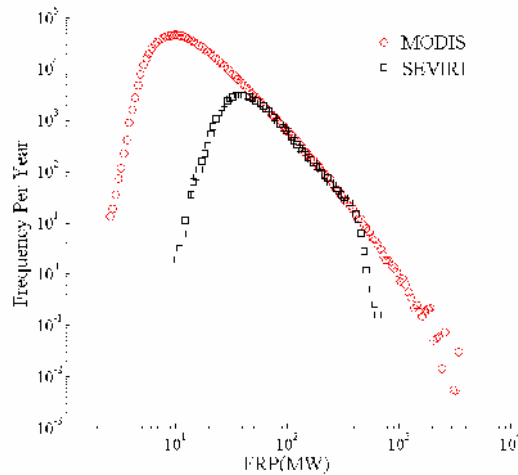


**Figure 4.4:** Frequency-magnitude distributions for all contemporaneous SEVIRI and MODIS fire pixels detected across Africa in Feb 2004-Jan 2005 (i.e. the training dataset discussed herein).


To account for the artefacts illustrated in the above frequency magnitude plot, a set of region-specific adjustment factors were developed and tested. Twelve months of coincident SEVIRI and MODIS observations made between May 2008 and April 2009 were used to construct a set of training and validation datasets – one pair for each of the four LSA SAF regions (e.g. Euro, NAfr, SAfr, and SAme). Boundaries of the MODIS level 2 swath products were used to identify all MODIS granules that intersected each region during the yearlong study period. Fire pixels were subset from the full MODIS ‘MOD14’ and ‘MYD14’ fire products using six, non-overlapping 5.0° grid cells arranged in the centre of each MODIS granule (Figure 4.5). Active fire pixels detected by MODIS outside of this region of interest were discarded and not used during the analysis. Such a sampling design ensured complete coverage of the 5.0° grid cells regardless of the MODIS ground track, and also mitigated the effects of image distortion at the edge of the MODIS swath due to the “bowtie effect.” Although the number of fire pixels detected in a 5.0° grid cell would theoretically decrease at higher latitudes due to a decrease in the ground sampling area (assuming observations of identical fire behaviour), this artefact was ignored since the latitudinal gradient existed in both the training and validation datasets.

Latitudes and longitudes of the MODIS fire pixels were translated into line and pixel (column) values in the SEVIRI coordinate system. This georeferencing procedure facilitated the retrieval of total column water vapour (TCWV), and thus enabled the calculation of atmospheric transmittance ( $\tau_a$ ) using the optical thickness ( $\tau_a$ ) and view zenith angle ( $\theta_v$ ) as described by Equation (49) in the ATBD. The MODIS estimates of FRP were then adjusted to account for atmospheric transmittance in the middle infrared spectral band. Atmospheric corrections could not be applied to MODIS fire pixels detected in September 2008 due to the unavailability of TCWV fields stored at LSA SAF.

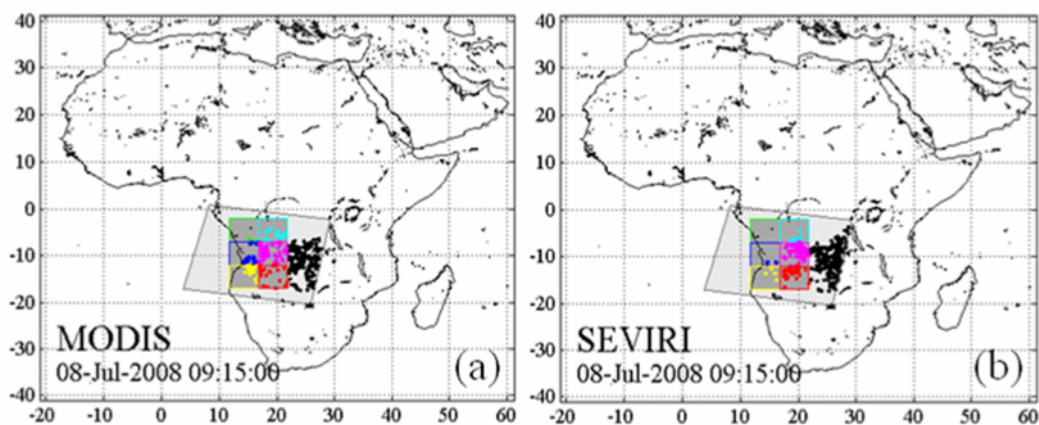


**Figure 4.5:** Graphical representation of the procedure used to generate the 2008 training and validation datasets. Fire pixels were subset from the “MOD14” and “MYD14” fire products between May 2008 and April 2009 using six 5.0° grid cells centred on the MODIS swath, as illustrated in (a). These same grid cells were then used in (b) to subset fire pixels from the SEVIRI full Earth disk images acquired at times coincident with the MODIS overpass, as well as from the three previous SEVIRI imaging timeslots prior to the MODIS overpass.



	Land SAF VR-FRP	Doc: SAF/LAND/IM/VR_FRP/V_09 Issue: Version V/2009 Date: 18/10/2009
---	-----------------	---

Next, all MODIS granules collected during the yearlong study period were matched to the most concurrent SEVIRI full Earth disk image. Here the MODIS granules and SEVIRI scans were considered concurrent if the start times for each acquisition were within  $\pm 6$  minutes of each other. The same  $5.0^\circ$  grid cells inscribed within the MODIS granule were then used to clip SEVIRI fire pixels from (i) the most coincident SEVIRI timeslot, and (ii) the three SEVIRI timeslots immediately preceding the MODIS overpass (Figure 8b). Again, active fire pixels detected by SEVIRI outside of this region of interest were not included in the analysis. Entire grid cells were also discarded if three consecutive SEVIRI imaging timeslots could not be retrieved prior to the SEVIRI timeslot concurrent with the MODIS overpass (i.e., if four imaging timeslots were not available). This sampling design not only permitted a genuine comparison of coincident SEVIRI and MODIS observations of FRP, but also mimicked the hourly temporal resolution of the gridded FRP product.

After the SEVIRI and MODIS fire pixels were spatially and temporally accumulated the concurrent and collocated  $5.0^\circ$  grid cells in each region were split into two halves to create the training datasets and the validation datasets. Relationships between the atmospherically corrected FRP observed by SEVIRI and MODIS were directly compared among the  $5.0^\circ$  grid cells contained within the training dataset. Rather than using the instantaneous FRP observed by SEVIRI at the timeslot most concurrent with the MODIS overpass, however, the average FRP estimated by SEVIRI during the preceding hour was used instead to correspond more appropriately with the hourly temporal resolution of the gridded fire product. The hourly-average of FRP estimated by SEVIRI was calculated by first summing the pixel level FRP in each  $G^\circ \times G^\circ$  grid box and at each 15-minute timeslot,  $t$ , as follows:

$$\tilde{R}_p(t, i_G, j_G) = \sum_{(i_f, j_f) \in G^\circ \times G^\circ} \tilde{R}_p(t, i_f, j_f) \quad \text{Equation 8}$$

where  $\tilde{R}_p(t, i_f, j_f)$  is the pixel-level FRP associated with each detection located at column  $i_f$  and line  $j_f$  within a particular  $5^\circ$  grid cell. The average FRP observed during the hour in each grid cell was then calculated as follows:

$$\tilde{R}_p(t_e, i_G, j_G) = \frac{1}{N_t} \sum_{t=t_e-C_t}^{t_e} \tilde{R}_p(t, i_G, j_G) \quad \text{Equation 9}$$

where  $t_e$  is the time of the gridded product generation,  $C_t$  is the duration of the compositing period (in this case one hour), and  $N_t$  is the number of valid (i.e., non-corrupted) images in the compositing period. The SEVIRI timeslot coincident with the MODIS overpass was considered as the time at which the gridded FRP product is generated,  $t_e$ . Note that  $N_t$  varies depending on the LSA SAF region that is processed, and that  $N_t$  ideally achieves a maximum of four timeslots per hour. Also note that  $N_t$  represents the number of available images during the compositing period regardless of whether SEVIRI detects a fire pixel or not. Lastly, as a reminder, the hourly-average of FRP estimated by SEVIRI in Equation 9 is atmospherically corrected, but is not yet adjusted by the fraction of cloud cover.

At this point in the analysis it was necessary to develop a functional relationship between  $\tilde{R}_p(t_s, i_G, j_G)$  and the FRP observed by MODIS. This functional relationship was again explored at a spatial resolution of  $5.0^\circ$  and a temporal resolution of one hour in order to correspond with the gridded fire product. Prior to performing any comparison, however, the training and validation datasets for the northern and southern hemispheres of Africa were combined since the analysis of either hemisphere in isolation, and the analysis of one- half year, would include several months of high fire activity, but also several months of low fire activity. Combining the two regions increased the observations of increased fire activity and extended the range over which a preliminary, underlying relationship could be developed.

For each  $5^\circ$  grid cell in both the NAfr and SAfr regions, the value of  $\tilde{R}_p(t_s, i_G, j_G)$  was compared to the SEVIRI-to-MODIS ratios of FRP (Figure 3a). The SEVIRI-to-MODIS ratios of FRP were calculated by simply dividing  $\tilde{R}_p(t_s, i_G, j_G)$  by the FRP measured by MODIS at the most concurrent timeslot. Despite the broad range of these ratios, the underlying trend between  $\tilde{R}_p(t_s, i_G, j_G)$  and the SEVIRI-to-MODIS ratios of FRP was discerned by calculating the median value of the sensor-to-sensor ratios within decadal bands along the x-axis (Figure 3a). Here the median SEVIRI-to-MODIS ratio of FRP increased from 0.10 to 0.74 as  $\tilde{R}_p(t_s, i_G, j_G)$  spanned 5 orders of magnitude. Such a relationship is consistent with the seasonal cycle of SEVIRI-to-MODIS ratios of FRP illustrated earlier in Figure 0.15 in so far as the SEVIRI-to-MODIS ratios of FRP were greater when the total radiative output of the fires were also at their peak.

The median SEVIRI-to-MODIS ratios were then re-applied to the binned values of  $\tilde{R}_p(t_s, i_G, j_G)$  in order to predict the FRP observed by MODIS (Figure 3b). This preliminary analysis revealed that  $\tilde{R}_p(t_s, i_G, j_G)$  could be related to the FRP observed by MODIS via a simple power law function. Therefore the power function is assumed to be the most general form of the relationship between SEVIRI and MODIS and is expressed as follows:

$$\hat{\tilde{R}}_p(t_s, i_G, j_G) = \alpha \times \tilde{R}_p(t_s, i_G, j_G)^\beta \quad \text{Equation 10}$$

where  $\hat{\tilde{R}}_p(t_s, i_G, j_G)$  is the predicted MODIS measurement of FRP, and  $\alpha$  and  $\beta$  are parameters to be applied to the hourly-average of FRP estimated by SEVIRI in a  $5.0^\circ$  grid cell.



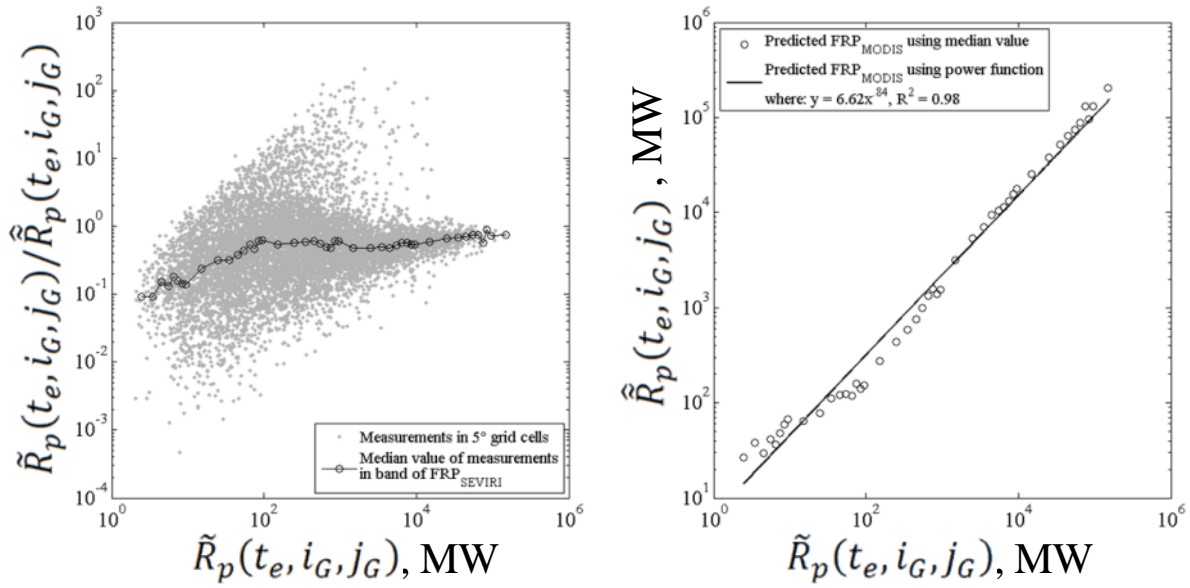




**Figure 4.6:** On the left, SEVIRI-to-MODIS ratios of FRP plotted as a function of the hourly average of FRP measured by SEVIRI in 5.0° grid cells in both the NAfr and SAfr regions. The SEVIRI measurements were binned and the median MODIS value within each bin is shown as an open circle. On the right is the relationship between the SEVIRI binned values and the median MODIS measurement within the bin. At the continental scale the relationship between SEVIRI and MODIS can best be described with a power-law function (solid line).

A unique set of coefficients (with associated standard errors) were derived for each of the four LSA SAF regions using the training datasets. The parameters  $\alpha$  and  $\beta$  for each region were then applied to the values of  $\tilde{R}_p(t_e, i_G, j_G)$  contained within the validation dataset in order to predict the FRP measured by MODIS. Differences between the prediction and the MODIS measurements in the validation datasets were used to evaluate the efficacy of the model at 5.0° spatial resolution and hourly temporal resolution. In addition, estimates of FRP were generated at a coarser spatio-temporal resolution by aggregating the 5.0°, hourly-average values of FRP measured by SEVIRI and the 5.0°, instantaneous FRP measured by MODIS. Here, all fire pixels were aggregated into weekly windows. Although MODIS only images a small portion of the continent at any given overpass, the repeat cycle of MODIS provides unbiased geographical coverage of a region a weekly basis. Therefore this coarsest collection of fire pixels is representative of weekly fire activity across the entire region.

#### 4.2.3 Analysis of Ecosystem-Specific Biases

In this study component, the ratio of fire detections between SEVIRI and MODIS was studied with a view to an analysis of any bias that resulted from fires burning in different landcover types. As an example, it might be possible that SEVIRI detects a greater proportion of the MODIS-detected fires in grasslands than in forests due to the fires in forests being dominated by lower FRP events. For this study, fire detections

 	Land SAF VR-FRP	Doc: SAF/LAND/IM/VR_FRP/V_09 Issue: Version V/2009 Date: 18/10/2009
---	-----------------	---

from the KCL SEVIRI FRP product for the time period February 2004 to January 2005 were grouped according to the land cover type classification of the Global Land Cover (GLC) 2000 product (Mayaux *et al.*, 2004). MODIS fire detections from the corresponding MOD14 and MYD14 datasets were used for the comparison datasets. The relative frequency of fire occurrence in the various land cover classes was analyzed in order to find out if the detection algorithm or the pixel resolution of the SEVIRI data was leading to ecosystem specific biases.

#### **4.2.4 Effects of Viewing Geometry**



As noted above, the SEVIRI pixel size increases with distance from the sub-satellite point. This will lead to larger FRP values required to detect a fire (and also the ability to record larger FRP values before the pixel reaches saturation). The impact will be masked to some degree by the fact that different landcover classes will likely characterised by different FRP characteristics (see above), and that landcover is not uniform as you move away from the sub-satellite point. The most extreme effects of viewing geometry related issues will be seen towards the edge of the scan, and this issue was therefore investigated via an analysis to determine whether the SEVIRI FRP/MODIS FRP ratio is lower over such areas (e.g. Madagascar and South America) than at regions closer to the sub-satellite point.

#### **4.2.5 Effects of Saturation**

Saturation of the SEVIRI pixels (nominally for brightness temperatures above 335 K) will not impact on the ability of the FRP algorithm to detect fires, but it will lead to an underestimation of the true fire radiative power. The impact of this was gauged by firstly determining the typical degree of saturation seen in standard SEVIRI level 1.5 data, and secondly by exploiting data from the SEVIRI ‘special operations’ mode experiment whereby the Meteosat-8 SEVIRI was operated in the low-gain setting. In this mode the sensor was able to record without the effects of sensor saturation, and the resulting ‘true’ FRP record was compared to that in which the FRP of pixels whose MIR brightness temperature was above the normal 335 K maximum was set to what it would have been had saturation in fact occurred at that temperature.

#### **4.2.6 Effects of SEVIRI sensor characteristics and Level 1.0 to 1.5 pre-processing operations**

The methodology adopted was two fold, firstly a direct comparison of SEVIRI level 1.0 and level 1.5 data of large fires, in order to assess the impact of the level 1.0 to 1.5 pre-processing procedures. Secondly, simulation of the SEVIRI observation process, using modelled fires and background conditions taken from the aforementioned BIRD HSRS imagery (in order to obtain realistic measures of ambient background brightness temperature variability around fires). The modelling including simulation of the SEVIRI point spread function (PSR) and the impact of the Finite Impulse Response (FIR) filter, which is applied to the recorded signals onboard the MSG satellite. The impact of the PSF and FIR filter are present even within Level 1.0 data, but the level 1.5 data have additional features induced via the spatial regridding and interpolation algorithms used in the EUMETSAT data processing chain (algorithms

 	Land SAF VR-FRP	Doc: SAF/LAND/IM/VR_FRP/V_09 Issue: Version V/2009 Date: 18/10/2009
---	-----------------	---

are fully detailed in the Image Processing Facility Algorithm Documentation; EUMETSAT, 2003).

### **4.3 LandSAF Product Validations**

The key purpose here was to determine whether the Land SAF FRP product had similar accuracy characteristics to the KCL FRP product, which had formed the dataset used for the majority of the other accuracy evaluation tests.

#### **4.3.1 Comparison to KCL product**

This work examined the errors of omission and commission of the LandSAF FRP product with respect to the KCL FRP product, only over Africa since the KCL FRP product is only available for this continent. Data from 1 – 5 August 2007 (415 separate SEVIRI imaging slots) from both processing chains were compared over the Land SAF southern Africa region, with errors of omission, commission and per-fire FRP levels of agreement quantified. This allowed determination of whether the Land SAF products have the same or similar accuracies as the original KCL FRP product. The August 2007 Land SAF FRP product dataset showed insufficient fire detections in the north Africa region to warrant a detailed comparison, and data from a different period (e.g. February) should be obtained for this purpose during any future work.

#### **4.3.2 Comparison to MODIS**

Here the errors of omission, commission and per-fire FRP levels of agreement were quantified for the Land SAF FRP product, using as the comparison dataset the MOD14/MYD14 MODIS data. The methodology used was that previously adopted for the same analysis undertaken for the KCL FRP product, outlined in Section 0. The areas covered by this analysis were the southern African and South American Land SAF regions.

### **4.4 Validation Based on Impact Studies**

#### **4.4.1 Impacts of Temporal Resolution**

In order to assess the impact of representing or neglecting the temporal variability of fire emission on time scales of hours and days, model simulations of atmospheric carbon dioxide concentrations (CO<sub>2</sub>) using a preliminary version of the GEMS CO<sub>2</sub> model were carried out. Atmospheric CO<sub>2</sub> has been selected for the study because it has a long atmospheric lifetime and does not possess atmospheric sources and sinks. Therefore, it can be regarded as a passive tracer with a long lifetime, and its fields display the interactions of the different emission data with the atmospheric transport most clearly. Even though the variations of the CO<sub>2</sub> field induced by fire emissions appear relatively small, they are significant for the source/sink inversions, which are the ultimate goal of atmospheric CO<sub>2</sub> monitoring.

The GEMS CO<sub>2</sub> model is a global atmospheric transport model which predicts 3D global distributions of CO<sub>2</sub>. In the current setup of the model, CO<sub>2</sub> is treated as

passive tracer and transport by advection, turbulence and convection are resolved (see also section 0). The current GEMS system (Hollingsworth *et al.* 2008) uses fire emissions from the GFEDv2 inventory (van der Werf *et al.* 2006) with 8 day time resolution (see Section 0). Atmospheric CO<sub>2</sub> fields modelled with these emissions are compared to fields modelled with emissions with 1 hour and 1 day time resolution.


The CO<sub>2</sub> emission data with different time resolutions were created by modulating the GFEDv2 8 daily emissions with the higher frequency temporal patterns observed by SEVIRI. Thus the impact of the temporal resolutions is separated from the one due to different total emission amounts. The following steps are performed to make consistent emissions with 8d, 1d, and 1h resolution:

1. convert GFEDv2\_8days dimensions to [kg/m<sup>2</sup>/s]
2. obtain gridded (1°×1°) SEVIRI FRP data set corrected for partial cloud cover, atmospheric transmission, and missed small fires. This product has been generated by KCL.
3. fill FRP data gaps
  - a. missing 1 hour frames replaced with previous frames
  - b. missing grid cell values (-1) replaced with zero
4. average FRP over 8 day periods of GFEDv2\_8days
5. add 1 W to eliminate division by zero errors
6. compute conversion factor = GFEDv2 emission / SEVIRI FRP, for each 8 day period and 1°×1° pixel over Africa
7. compute SEVIRI emission = SEVIRI FRP times conversion factor, for each 1 hour and 1°×1° pixel over Africa
8. pad with GFEDv2\_8days for global coverage
9. average over 1 day and 8 days
10. convert 8. and 9. to GRIB with 1°×1° grid
11. convert 10. to GRIB with reduced Gaussian resolution T159

Four model runs have been performed, based on the different fire emission input data sets. The simulations are not constraint by any CO<sub>2</sub> observations. Key properties of the model setup are listed in Table 4.1.

**Table 4.1: CO<sub>2</sub> model run setup**

<b>modelled period</b>	2 February – 24 December 2004			
<b>horizontal resolution</b>	T159 (~ 125 km)			
<b>number of vertical levels</b>	60			
<b>meteorology</b>	nudged to operational analysis at 00 and 12 UTC			
<b>Fire emission level</b>	Lowest model level			
<b>fire emission time resolution</b>	no fires	8 days (8d)	1 day (1d)	1 hour (1h)

	Land SAF VR-FRP	Doc: SAF/LAND/IM/VR_FRP/V_09 Issue: Version V/2009 Date: 18/10/2009
---	-----------------	---

#### **4.4.2 Impact of FRP versus Hot Spot Detection**

Mikhail Sofiev at FMI has kindly given FREEVAL access to his analyses of the PM<sub>2.5</sub> fire emission fields generated with the FMI Fire Assimilation System (FAS) from MODIS TA and FRP observations and of the SILAM dispersion model forecasts of PM<sub>2.5</sub> based on the FAS emissions, see section 0.

One line of analysis compares the emission fields obtained from the two MODIS products and averaged over several months. Since both are obtained with empirical emission factors, the comparison is mostly sensitive to the different geographical distributions of fire emissions obtained by using either a qualitative hot spot product, i.e. TA, or the quantitative FRP information.


The second line of analysis compares modelled atmospheric PM<sub>2.5</sub> fields, based on the two different fire observation products, with satellite-based and in-situ observations of the actual atmospheric aerosol fields. Thus an end-to-end assessment of the two approaches can be made.

#### **4.4.3 Impact on Estimating Fire Emissions**

The quality of SEVIRI FRP-derived fire emissions was assessed by comparison to the published estimates contained in the Global Fire Emissions Database (GFED) version 2 (van der Werf *et al.* 2006). Because of the spatially limited coverage of the SEVIRI retrievals, the comparison is restricted to the African continent. For the analysis, the continent is subdivided into two study regions, namely Africa north of the equator and Africa south of the equator. The analysis covers the period February 2004 to January 2005 and uses monthly estimates of carbon emissions. The focus of the comparison is on how well SEVIRI FRP derived carbon emissions for the two sub-regions agree with the GFED estimates in terms of seasonal pattern and total amounts.

The GFED inventory for years after 2001 is based on MODIS active fire detections which were scaled to a limited number of MODIS burned area observations and then multiplied by available fuel loads and combustion efficiencies derived from the CASA vegetation model. While MODIS has a higher likelihood of fire detection in an individual scene compared to SEVIRI, there are far less scenes available per day and these do not capture the time window of maximum daily fire activity (the two daytime overpasses of MODIS Aqua and MODIS Terra occur at 10:30 and 14:30 local time, respectively). As a consequence SEVIRI actually detects a larger absolute number of fires per day than MODIS and one has to rely on the scaling procedure for MODIS to provide a complete estimate of fire affected area and burned material. Therefore, the comparison of SEVIRI FRP to GFED emissions should be regarded as a comparison between two independent data sets rather than a validation using a reference data set. Nevertheless, this comparison is important, because GFED has become a de-facto standard in atmospheric composition modelling.

Another, more qualitative validation of the seasonality of emissions derived from SEVIRI FRP uses MOPITT CO profiles for comparison. The analysis covers the

 <b>LSA SAF</b> Land Surface Analysis Satellite Application Facility	Land SAF VR-FRP	Doc: SAF/LAND/IM/VR_FRP/V_09 Issue: Version V/2009 Date: 18/10/2009
---	-----------------	---

same period as the analysis mentioned above (February 2004 to January 2005). For the analysis, monthly variations in SEVIRI FRP in southern hemispheric Africa are directly compared to mean monthly MOPITT CO profiles for the same region. CO is a tracer for biomass burning and the satellite-derived CO profiles provide an estimate of the seasonality and the amount of burning. Because of being different quantities, the direct comparison of FRP with measured CO profiles provides no quantitative comparison. However, because estimated CO emissions are considered to be largely proportional to the FRP (assuming that at least on a regional scale fires always represent a mix between flaming and smouldering conditions with roughly constant proportion), the comparison provides qualitative information on whether the seasonal pattern of FRP-derived CO emissions will match with observations.

#### **4.4.4 End-to-end Use (Greek Fires Case Study)**

In late August 2007, huge fires burnt in Greece. The FRP derived emissions and the simulated and observed plumes of these fires were used to test and demonstrate the feasibility and potential of fire plume modelling and, ultimately, forecasting by combining SEVIRI FRP with the GEMS system for aerosol monitoring.

The current version of the global aerosol model developed in GEMS (Morcrette *et al.*, 2008) is driven with the GFEDv2 inventory. For this study, aerosol emissions derived from the SEVIRI FRP product by KCL have been superimposed on this data set and the modelled smoke plumes are compared to MODIS observations. In contrast to the tests on the impact of temporal resolution (see section 0) where only the time information of SEVIRI was used, here the FRP product was used quantitatively with its correction to account for small fires. The simulation also covers a smoke plume that is transported from Algeria to Italy and is compared to ground-based AERONET observations at Lecce University. The individual data processing steps were:

1. convert SEVIRI 3.9  $\mu\text{m}$  channel to FRP [MW]
2. grid FRP to 0.1x0.1 deg grid
3. average over 1 hour
4. correct for fires below detection limit (no correction for partial cloud cover was needed, since Greece was cloud-free at the time of the fires)
5. convert
  - to Dry Matter combustion rate [kg/s] (factor 0.368 kg/s/MW)
  - to BC, OM, and SO<sub>4</sub> emission rate [kg/s] with emission factors based on a combination of Andreae and Merlet (2001) and Ichoku and Kaufman (2005)
6. interpolate to the grid cells corresponding to model resolution T799 (triangular truncation at wave number 799), which is the resolution of the operational deterministic ECMWF weather forecast and also representative for current regional air quality monitoring systems. (~25km)
7. run the GEMS aerosol model with fire emissions in lowest layer for 1 August – 6 September 2004. Compared to the standard GEMS model the resolution has been increased.



## VALIDATION RESULTS

### 5.1 Results of the Algorithm Performance Analysis

Figure 5.1 shows the impact of assumption (i), the fourth order power law approximation to Planck's Radiation Law, by comparing the FRP derived via the MIR radiance method ( $FRP_{MIR}$ ) to that derived via the Stefan-Boltzmann Law ( $FRP_{TRUE}$ ), in the case that the fire is fully resolved by the sensor (i.e. there is no 'background' non-fire component to the signal). The difference between these two measures, denoted by their ratio ( $R$ ), is due only to the uncertainty introduced by the Planck Function approximation, and is shown here to be relatively constant (i.e.  $R$  constrained between 0.88 and 1.12) over a significant part of the emitter temperature range considered (i.e.  $> \sim 665$  K and  $< 1365$  K).

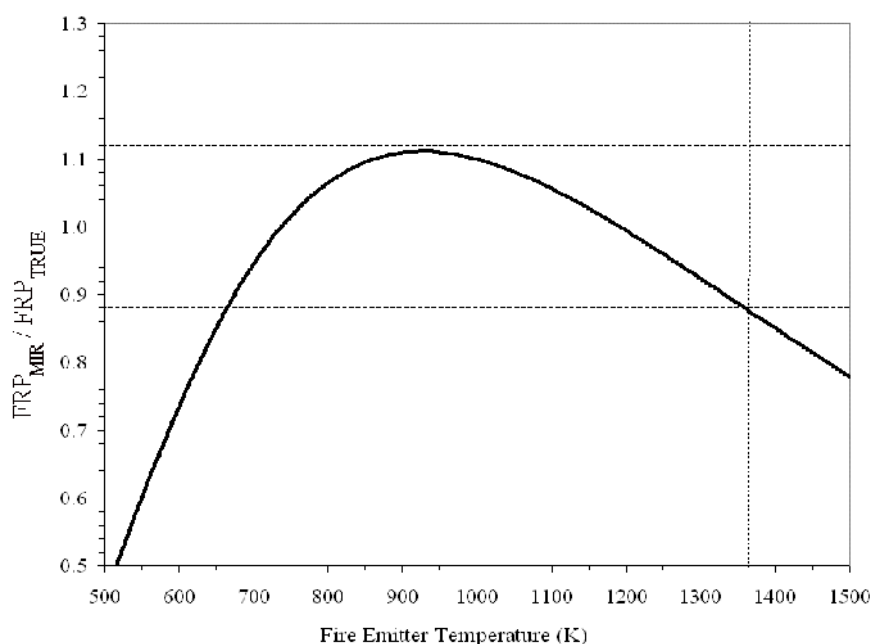


**Figure 5.1:** Ratio ( $R$ ) between the Fire Radiative Power estimate derived from MIR radiance method ( $FRP_{MIR}$ ), and the true FRP derived from the Stefan-Boltzmann Law ( $FRP_{TRUE}$ ). Calculations here assume pixels fully filled by fire. Horizontal dashed lines denote the limits where  $FRP_{MIR}$  values are within a factor of 0.88 and 1.12 of  $FRP_{TRUE}$ , whilst vertical lines denote the corresponding temperature range (665 - 1365 K).

An example of the emitter temperature distribution retrieved over a real wildfire is shown in Figure 5.2, indicating that in excess of 95% of the fire pixels have emitter temperatures in the 665 – 1365 K range, where  $R$  is constrained between 0.88 to 1.12. Thus the underlying FRP uncertainty induced by use of the MIR radiance method is



governed by this uncertainty, but the advantage is that by using this method we do not have to resolve the fire temperature distribution and can thus use the method on highly sub-pixel sized events, providing of course that we can assume that their temperatures lie within the above range. This range is expected to cover the vast majority of fire events, and is broadly consistent with that specified in, for example, Ohlemiller (1995) and Riggan *et al.*, (2004) for actively burning fires and in the assumptions made during derivation of the MODIS fire detection and fire characterisation approach (Kaufman *et al.*, 1998).

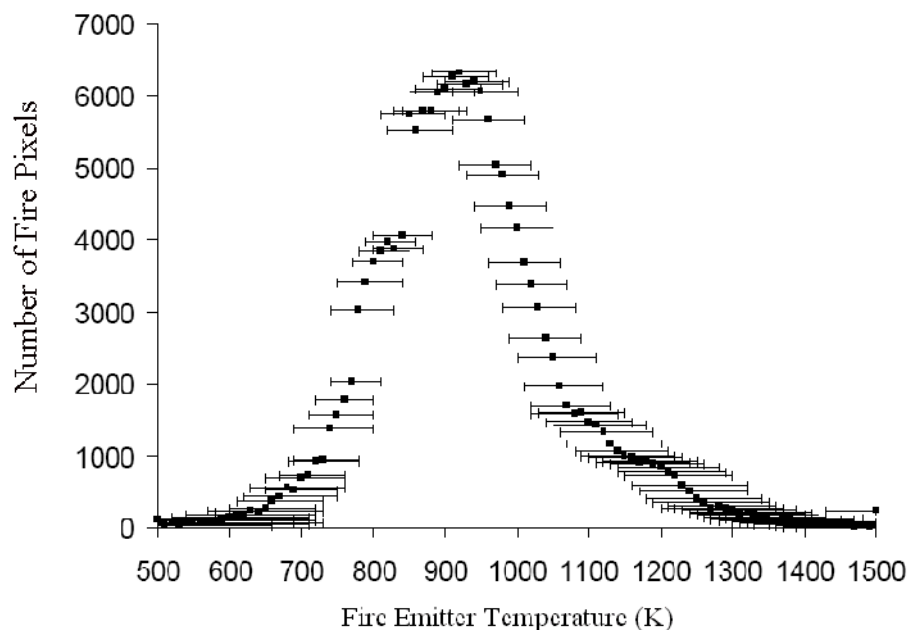


**Figure 5.2:** Fire emitter temperatures retrieved from analysis of Airborne Visible Infrared Imaging Spectrometer (AVIRIS) hyperspectral data of the 2003 Simi Fire in Southern California, USA by Dennison *et al.* (2006). The method used a spectral library of emitted hyperspectral radiance endmembers corresponding to a fire temperature range of 500-1500 K, along with reflected solar radiance endmembers, both based on simulations using the MODTRAN radiative transfer model. These endmembers were used to determine the true subpixel fire emitter temperature within each active fire pixel identified with AVIRIS. Error bars indicate the median range of emitter temperatures modelled within 5% of the RMSE for the indicated emitter temperature.

At the scale of satellite observations, e.g. the nominal 4.8 x 4.8 km pixel sizes supplied by SEVIRI, real fires consist of a wide mixture of temperature components within each ‘fire pixel’ rather than single temperature emitters – as can be seen from the temperature distributions seen in the 50 m spatial resolution AVIRIS data shown above. As a result, the ratio ( $R$ ) of  $FRP_{MIR}/FRP_{TRUE}$  for the mixed temperature fires contained in such large pixels may likely move away from the extremes shown in

Figure 5.1 due to FRP underestimation inherent towards the lower ( $< 750$  K) and upper ( $> 1200$  K) fire temperature limits being counteracted by FRP overestimation from the mid-range (750 – 1200 K) emitters. However, since the actual fire temperature distribution within a SEVIRI pixel is by definition unknown, the theoretical accuracy limits of 0.88 to 1.12 are maintained. Note that in the case of Figure 5.2, most fire pixels have temperatures between 800 and 1050 K, and in this range FRP estimated by the MIR radiance method positively biased ( $R > 1.0$ ), but when the full fire temperature distribution is considered the overestimation will be by a factor less than the maximum of 1.12.

The assumptions (ii) used to derive Equation 1.6 from Equation 1.5 were assessed for their impact on FRP retrieval accuracy via the aforementioned radiative transfer modelling of sub-pixel sized active fire observations. They were found to introduce no error significantly above the  $\pm 12\%$  introduced by the fourth order approximation to Planck's Radiation Law (whose magnitude was already demonstrated in

Figure 5.1.

Assumptions (iii) and (iv) regard uncertainties in the atmospheric parameter of the FRP equation ( $\tau_{MIR}$ , the MIR atmospheric transmission) and in  $L_{b,MIR}$  (the background radiance of the fire pixel, estimated from the background window pixels). Combining Equation 1.1 and an error of  $\pm L_{b,error,MIR}$  in the assumed background radiance we state:

$$FRP_{MIR} = \frac{1}{\tau_{MIR}} \left( \frac{\sigma}{a} \right) (L_{MIR} - L_{b,MIR}) \pm \frac{1}{\tau_{MIR}} \left( \frac{\sigma}{a} \right) L_{b,error,MIR}$$

[Wm<sup>-2</sup>]

**Equation 11**

The first term on the rhs of Equation represents the fire FRP, which has the potential *multiplicative* error sources due to the uncertainties related to the power law approximation (a factor of 0.88 to 1.12 as shown in Figure 5.1 and the assumed atmospheric transmission, which can act either in the same direction as the error introduced by the power law approximation (and thus magnify it) or can act in the opposite direction (and thus counteract it). The second term on the rhs represents the error in FRP introduced by the inability to estimate  $L_{b,MIR}$  perfectly from the background window pixels, and this is an *additive* error source. As can be seen from Equation , this value is multiplied by the inverse of the assumed atmospheric transmission. Only in cases where the fires actual FRP (term 1 of Equation ) is relatively small but the uncertainty in the background (term 2 of Equation ) is relatively large will the error in background characterisation have a major impact.

Conversely however, the magnitude of the multiplicative error on term 1 of Equation will grow with the fires FRP, and so it can remain significant for all classes of fire FRP.

The magnitude of these error sources is illustrated using a modelling exercise based on sets of true fire parameters (effective fire temperature and sub-pixel proportion; which together determine the fires FRP), the radiative transfer modelling to simulate SEVIRI spectral radiance observations of the ‘fire’ and ‘background window’ pixels, and the equations used to derive an estimate of the fire FRP from these observations. This system was perturbed by parameter alterations, notably to the assumed values of MIR atmospheric transmission and differences between the background pixel radiance and the true background radiance of the fire pixel itself (i.e.  $L_{berror,MIR}$  is non-zero in Equation ).

Results for three different effective fire emitter temperatures (650, 850 and 1000 K) and considering only a range of errors in the background characterisation, and not in assumed  $\tau_{MIR}$ , are shown in Figure 5.3. For each fire temperature, the results converge at the  $L_{berror,MIR} = 0$  point, with the magnitude of the error simply being that induced by the fourth order power law approximation to the Planck’s Radiation Law at that temperature (assumption (i)). As  $L_{berror,MIR}$  increases away from zero, the additive error component shown in Equation becomes non-zero and the same  $L_{berror,MIR}$  perturbation induces a larger percentage error in FRP for low FRP (i.e. lower temperature and/or lower sub-pixel fractional area) fires than for large FRP fires. Giglio and Kendall (2001) in a somewhat similar exercise considered perturbations in the background radiance of  $\pm 0.02 \text{ Wm}^2\text{sr-1}\mu\text{m}^{-1}$ , but here we consider perturbations up to of  $\pm 0.1 \text{ Wm}^2\text{sr-1}\mu\text{m}^{-1}$  since this level of background window radiance variability is seen in the SEVIRI FRP data, though values around  $\pm 0.03 \text{ Wm}^2\text{sr-1}\mu\text{m}^{-1}$  are more common. Only in situations where the fires are, in any case, very unlikely to be detectable do  $L_{berror,MIR}$  perturbations of  $\pm 0.03 \text{ Wm}^2\text{sr-1}\mu\text{m}^{-1}$  have a strong influence on  $FRP_{MIR}$ . For fires having FRPs greater than the minimum values confidently detectable by SEVIRI, perturbations of this sort add significantly less than 10% error to that already existing from the Planck function approximation, irrespective of the actual fire temperature or sub-pixel size.

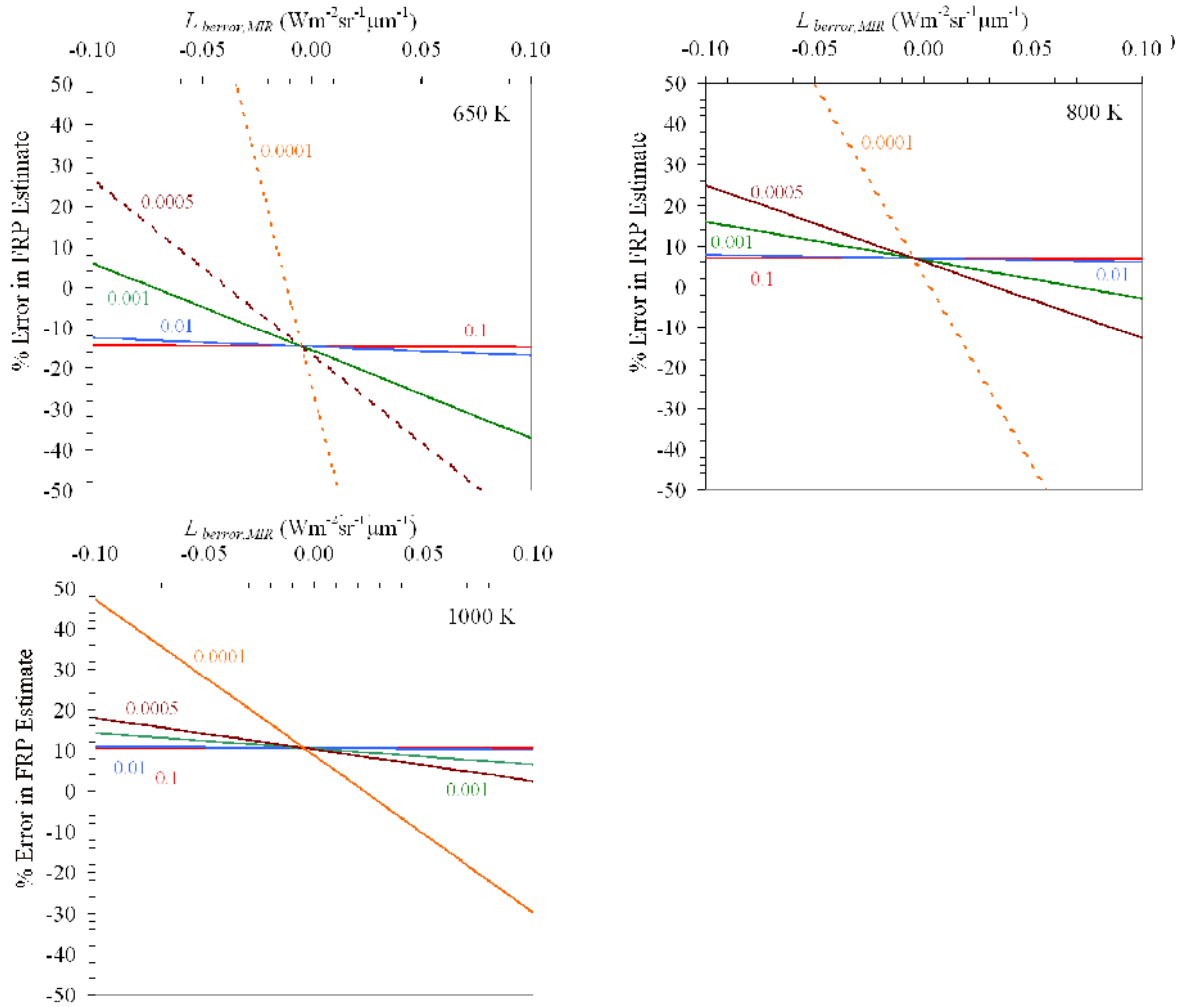


**Figure 5.3:** Departure of estimated FRP from true FRP for blackbody fires of temperature 650, 800 and 1000 K and fractional areas 0.1 to 0.0001 (denoted by the labels) as a function of the level of disagreement between the assumed background radiance signal and its true value (i.e. the value expressed by  $L_{berror,MIR}$  in Equation ). Values of other fixed parameters such as downwelling and upwelling atmospheric radiances and the atmospheric transmissivity have the values taken previously in the similar modelling study conducted by Wooster et al. (2005). Results are calculated here using the full parameterisation of Equation 1.5 and Equation 1.1 to take into account all error sources. Dotted lines indicate situations where the fire is too cool and/or small to be robustly detectable (i.e. MIR brightness temperature is raised by less than 6 K over that of surrounding non-fire pixels). At  $L_{berror,MIR} = 0$  results for each fire temperature converge, confirming the insensitivity of the error to fire fractional area under this condition and thus the appropriateness of the assumptions made in deriving Equation 1.6 from Equation 1.5.

Figure 5.4 indicates the additional sensitivity of the FRP retrievals to the estimate of MIR atmospheric transmission, and how this interacts with  $L_{berror,MIR}$  assessed in the previous Figure. Using an 800 K fire as an example, the effect of an error of  $\pm 15\%$  in

the assumed value of  $\tau_{MIR}$  is assessed. Assuming observations at the sub-satellite point, this equates approximately to an assumed minimum atmospheric transmission in the MIR spectral band ( $\tau_{MIR} = 0.61$ ) when the transmission is actually at a maximum ( $\tau_{MIR} = 0.7$ ), and *vice versa*. For such a fire, Figure 5.4b confirms that perfect knowledge of both  $\tau_{MIR}$  and  $L_{b,MIR}$  allows the maximum error in FRP to remain lower than +10% for all fire fractional areas and thus all FRP values. A 15% overestimate in  $\tau_{MIR}$  results in an FRP underestimate of  $\sim 10\%$  (Figure 5.4a), whilst a 15% underestimate in  $\tau_{MIR}$  increases the magnitude of the FRP overestimate derived via the MIR radiance method, to  $\sim 25\%$  for all detectable fires Figure 5.4c).

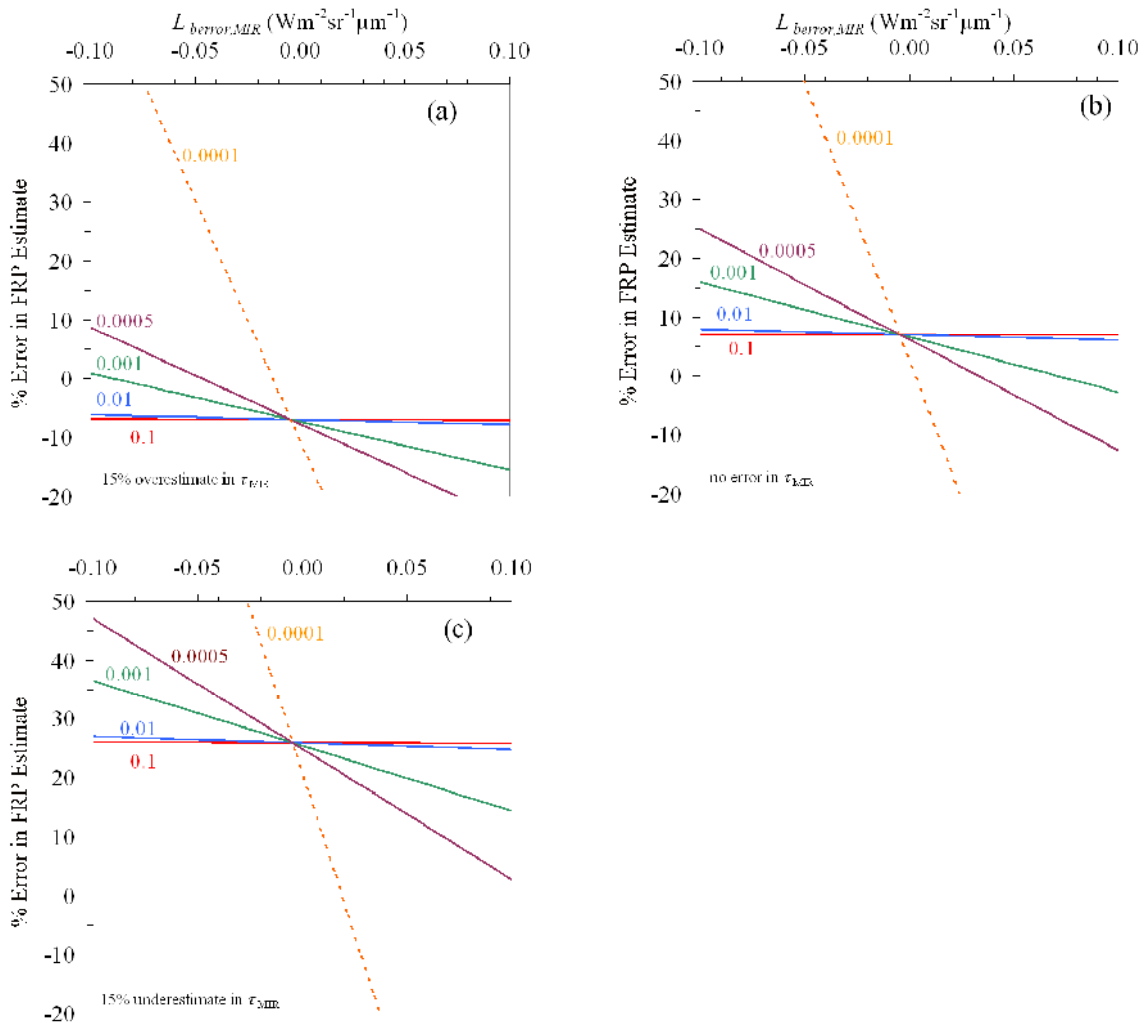


**Figure 5.4:** As Figure 5.3. but now expressing the departure of the estimated FRP from the true FRP for blackbody fires of temperature 800 K and fractional areas 0.1 to 0.0001 (denoted by the labels) as a function of the level of disagreement between the assumed background radiance signal and its true value (i.e. the value expressed by  $L_{berror,MIR}$  in Equation ) and for different errors in the assumed MIR atmospheric transmission. Values of other fixed parameters such as downwelling and upwelling atmospheric radiances and the atmospheric transmissivity have the values taken previously in the similar modelling study conducted by Wooster et al. (2005). A 15% overestimate in assumed MIR atmospheric transmission is assumed in (a), perfect knowledge in (b), and a 15% underestimate in (c).

Dotted lines indicate situations where the fire has too low and FRP to be robustly detectable (i.e. the MIR brightness temperature is raised by less than 6 K over that of surrounding non-fire pixels). At  $L_{\text{error}, \text{MIR}} = 0$  results for each fire temperature converge, indicating the insensitivity of the error to fire fractional area under this condition.

In terms of reported error for each FRP estimate, currently what is provided in the Land SAF FRP product is a measure of the additive error component (term 2 of Equation ), calculated as the following [though from the ATBD it may not, apparently, currently be adjusted for the atmospheric transmission]:

$$FRP_{\text{error\_additive}} = \pm \frac{A_s}{\tau_{\text{assumed}, \text{MIR}}} \left( \frac{\sigma}{a} \right) \sigma_{\tilde{I}_b} \quad [\text{W}]$$

### Equation 12

where  $\tau_{\text{assumed}, \text{MIR}}$  is the assumed MIR atmospheric transmission,  $A_s$  is the pixel sample area, and  $\sigma_{\tilde{I}_b}$  is the estimate of uncertainty in the background radiance of the fire pixel, estimated from the background window standard deviation.

Additional uncertainty comes from the multiplicative error term, which can be calculated from:

$$FRP_{\text{error\_multiplicative}} = \left( FRP_{\text{measured}} \pm FRP_{\text{error\_additive}} \right) \left( \frac{1}{R} \frac{\tau_{\text{assumed}, \text{MIR}}}{\tau_{\text{actual}, \text{MIR}}} - 1 \right) \quad [\text{W}]$$

### Equation 13

Where  $FRP_{\text{measured}}$  is the reported FRP in the product,  $FRP_{\text{error\_additive}}$  is the additive error calculated from Equation ,  $R$  is the ratio uncertainty resulting from the fourth order approximation to the Planck function shown in Figure 5.1 and  $\tau_{\text{assumed}, \text{MIR}}$  and  $\tau_{\text{actual}, \text{MIR}}$  are the assumed and actual MIR atmospheric transmission respectively. In most cases the actual values of  $R$  and  $\tau_{\text{actual}, \text{MIR}}$  will be unknown, though their potential range is known and reported in the ATBD (Govaerts *et al.*, 2007). Hence, using these values the appropriate range of potential multiplicative error can also be calculated for any FRP estimate reported in the product. The extreme values of the sum of the additive and multiplicative error components can then be taken as the estimate of overall uncertainty on FRP, which can be used to place uncertainty bounds on  $FRP_{\text{measured}}$ .

A mean background window radiance standard deviation of  $\sim 0.03 \text{ Wm}^{-2}\text{sr}^{-1}\mu\text{m}^{-1}$  was determined from the Land SAF FRP products of southern Africa, with maximum values three times this. Independent testing of the levels of background window variability found at non-fire pixels (where the true ‘background’ temperature of the central pixel in the background window pixel grid is known) indicated that the standard deviation of background window radiances was mostly larger than the actual radiance difference between the central pixel of the background window and the mean radiance of the surrounding pixels, with Figure 5.5 showing an example of this at two different landcover classes (grassland and forest). This was found true for background windows of  $5 \times 5$ ,  $7 \times 7$  or  $10 \times 10$  pixels in size. Therefore, the background window

radiance standard deviation measure currently used to estimate the additive error component of the FRP uncertainty budget is an appropriate, if perhaps somewhat conservative, measure.

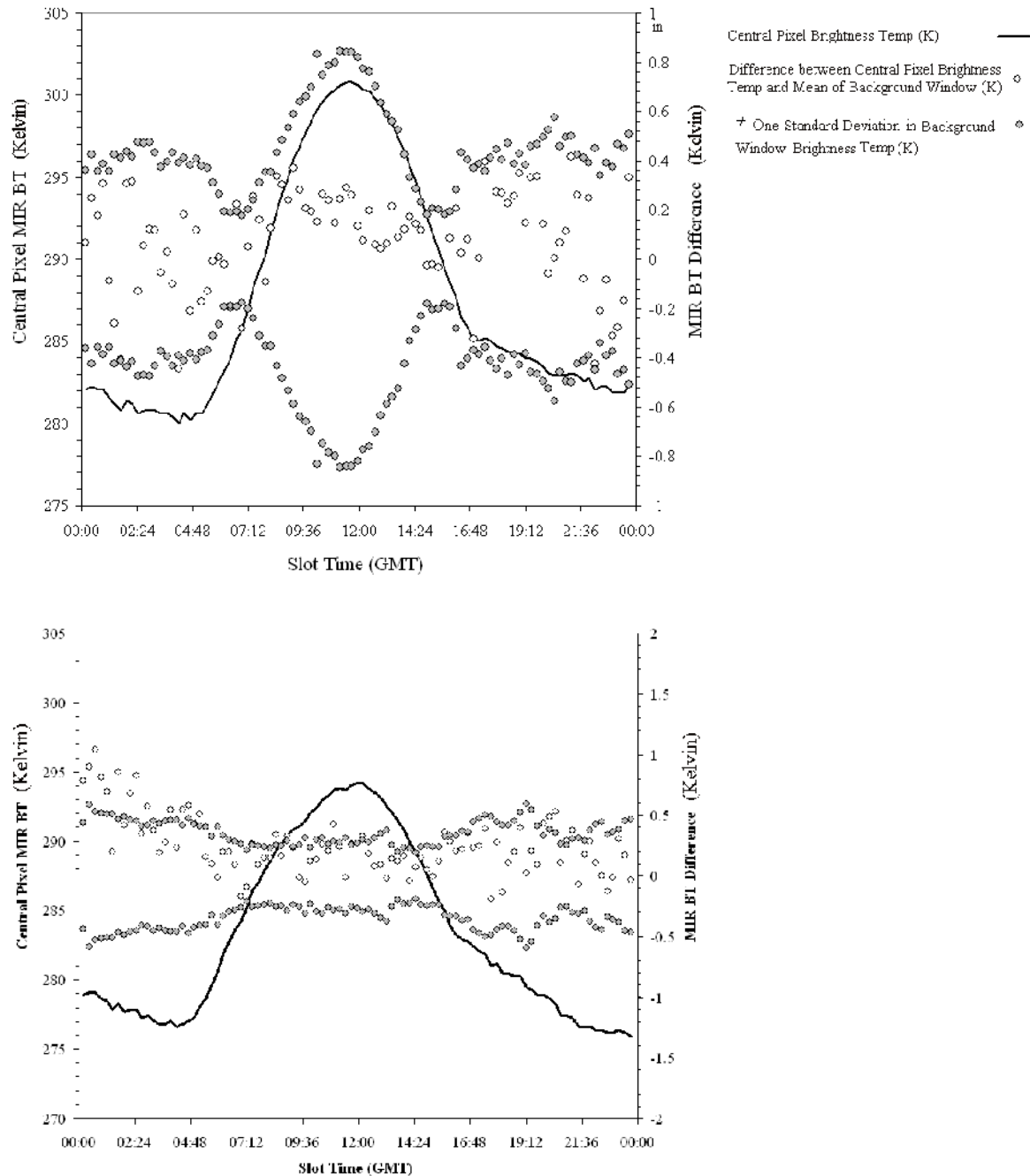


**Figure 5.5:** The central pixel brightness temperature of a 5×5 pixel window plotted over the full 24 hr cycle for a southern Africa closed grassland site (top) and a deciduous forest site (bottom), as identified by the GLC2000 landcover database. Also shown are the difference between this pixels brightness temperature and the mean of the remaining background window pixels, and  $\pm$  one standard



*deviation of the background window pixels. This latter figure is seen to mostly be larger than the actual difference between the central pixel and the mean of the background window pixels.*

The total FRP uncertainty, estimated as the maximum range of the sum of the additive and multiplicative error components discussed above and presented in Equation and , was estimated for the full range of per-pixel FRP potentially measurable from SEVIRI. The calculations assumed both a ‘worst case’ (Case 1) additive error budget scenario where  $\sigma_{\tilde{I}_b}$  is equivalent to the aforementioned maximum background variation, and the ‘mean’ case (Case 2) where  $\sigma_{\tilde{I}_b}$  is equivalent to the aforementioned mean variation. In both cases it was assumed that little information was available to estimate the true atmospheric transmission in the MIR spectral band, so  $\tau_{assumed, MIR}$  was taken as the mid-range value of 0.66 calculated for a SEVIRI view zenith angle of 30 degrees and a water vapour content of 30 kg/m<sup>2</sup> [and thus is essentially a ‘default’ value in the middle of the actual potential range] and values of  $\tau_{actual, MIR}$  were taken up to the possible extremes of 0.61 to 0.7 for that view zenith angle. In this way the multiplicative error budget represented her is the maximum uncertainty likely to be present, and could be reduced should it be possible to provide values of  $\tau_{assumed, MIR}$  that are known to be closer to  $\tau_{actual, MIR}$  than this (e.g. from modelled atmospheric water vapour distributions across the SEVIRI field of view obtained with a meteorological forecast model).

Figure 5.7 shows the results from the uncertainty model produced with such assumptions. In Case 1 the additive error resulting from the large background radiance uncertainty equates to an FRP uncertainty of 34 MW at the 30 degree VZA (where pixels are 15% larger than at the sub-satellite point), which represents a substantial fraction of the measured FRP for fire pixels not too far above the minimum that are detectable with SEVIRI. (e.g.  $FRP_{measured}$  in the 50 – 100 MW range). In Case 2 the additive error resulting from the lower background radiance variability equates to a more manageable FRP uncertainty of 10 MW. In both Cases, it is apparent that the multiplicative error dominates the total uncertainty budget for most of the potential range of measured FRP, and only at the lower end of the potentially measurable FRP scale does the additive error make a major contribution. It should be noted, however, that this is particularly relevant as the majority of detected fires in Africa are characterised by low FRP values.

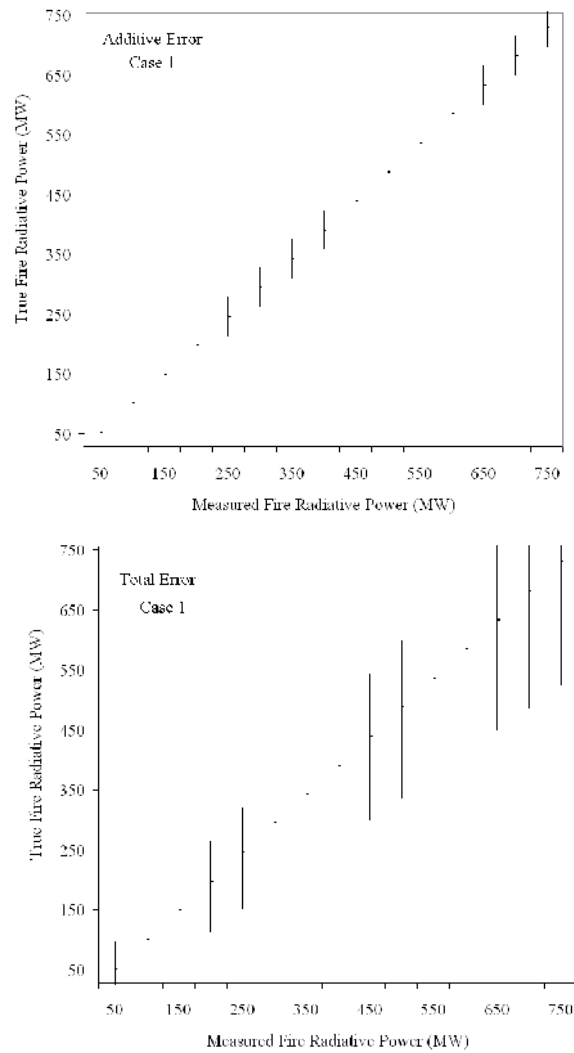
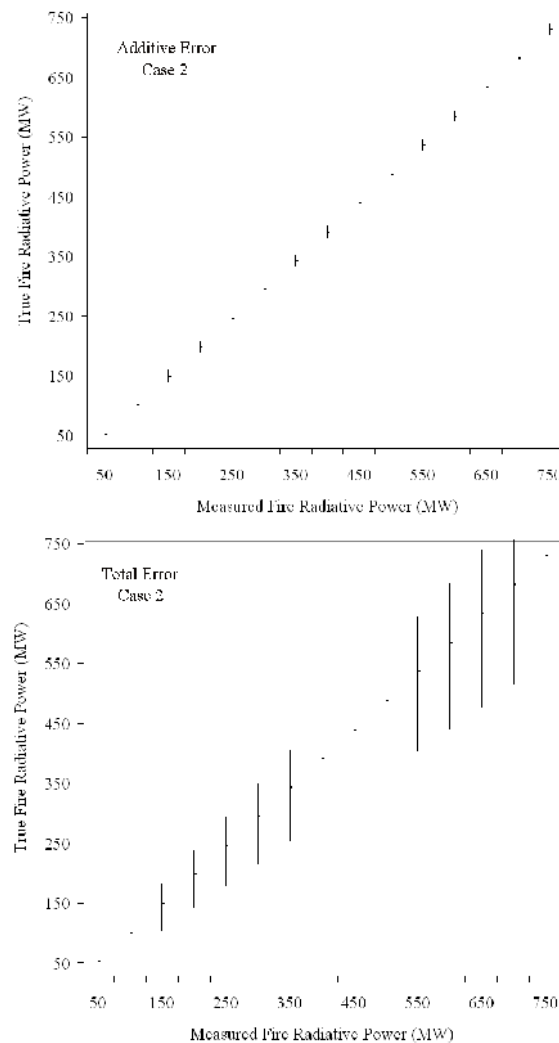


Figure 5.6 (continued on next page)




**Figure 5.7:** The x-axis reports the recorded FRP estimated by SEVIRI, whilst the y-axis reports the potential range of true FRP that could have given rise to that SEVIRI-derived FRP estimate. Results are shown over the over the 50 – 750 MW range, taking account of the additive error only (at left), and then both the total (additive plus multiplicative) error (at right). Case 1 assumes ‘maximum uncertainty’ errors in the radiance estimate of the fire pixel background (as deduced from the standard deviation of the background window radiances), whereas Case 2 assumes the mean uncertainty in this parameter. The maximum uncertainty in MIR atmospheric transmissivity is assumed in both cases, and both also take into account the full range of uncertainties in the fourth order approximation to the Planck Function (see text for details). In this way the multiplicative error component expressed here is the maximum expected for SEVIRI.

The calculations above assume the maximum uncertainty in atmospheric transmissivity. In all likelihood this will be reduced during the product development, for example by making use of model output for parameterise the atmospheric water vapour content and thus provide an estimate of  $\tau_{assumed, MIR}$  that better approximates  $\tau_{actual, MIR}$ . Where atmospheric transmissivity is known with negligible uncertainty, the error budget reduces to the additive error component from the background

window radiance variability, and the uncertainty due to the fourth order power law approximation to the Planck function. Assuming this, and using the relation presented in together with the observed FRP measures and additive error components deduced from 2000 fire pixel observations made across the southern African region on 2 June 2004 at the peak fire time slot (13:12 GMT). Figure 5.8 shows the distribution of FRP uncertainty. Half of the observations have a total FRP uncertainty less than  $\pm 40\%$ , and the mean uncertainty is also very close to this (i.e. uncertainties are normally distributed). On average the per-pixel FRP uncertainty due to the additive error component is 30%, and the remaining uncertainty comes from the Planck function approximation. If SEVIRI were to have a higher spatial resolution, the magnitude of the uncertainty for a particular FRP fire would reduce, since the spectral radiance contribution of that fire to the overall pixel radiance would be increase, though a higher spatial resolution system would also be able to detect fires having low FRP so the overall uncertainty distribution may not be significantly affected.

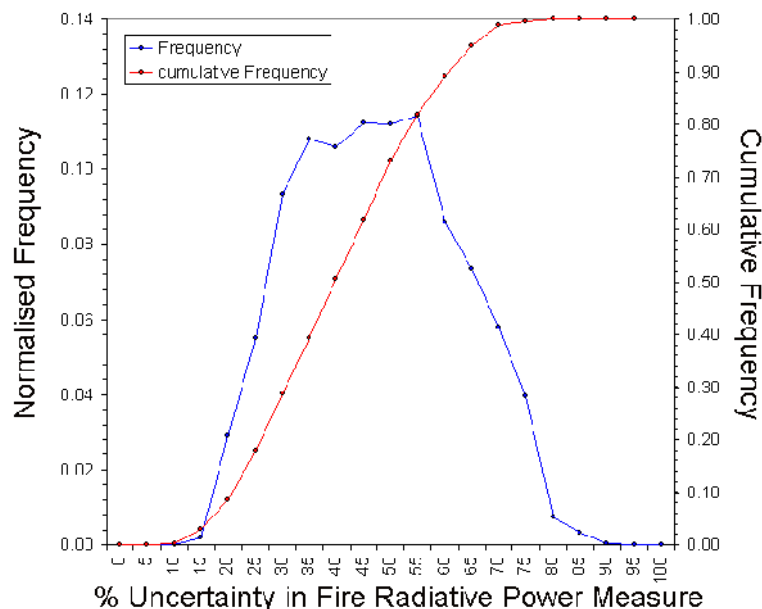


**Figure 5.8:** % uncertainty in FRP for 2000 observed fire pixels across southern Africa. The MIR atmospheric transmissivity of 0.66 was assumed to be known perfectly, and the additive error component was calculated from the background pixel window standard deviation. The multiplicative error component came from the fourth order power law approximation only.

	Land SAF VR-FRP	Doc: SAF/LAND/IM/VR_FRP/V_09 Issue: Version V/2009 Date: 18/10/2009
---	-----------------	---

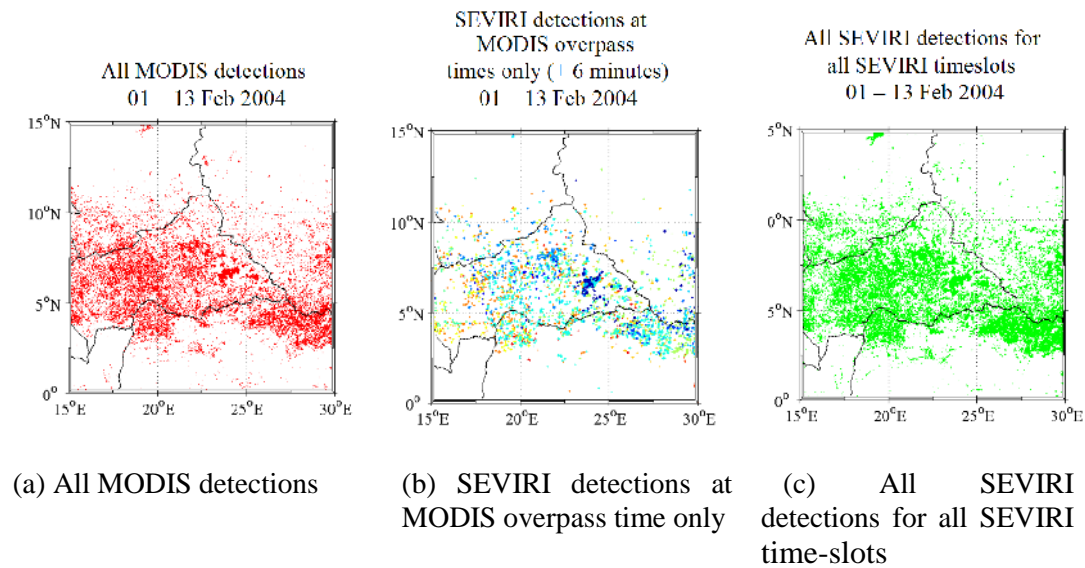
## 5.2 Results of the SEVIRI Product Performance Analysis

### 5.2.1 Per-Fire Comparisons

#### *Errors of Omission and Commission*

The analysis of errors of omission confirms that, though SEVIRI successfully detects very many fires each month, when MODIS and SEVIRI image the same area at the same time SEVIRI fails to detect some of the fires that MODIS does detect. Figure 5.8(a and b) demonstrate the effect over Central African Republic (CAR), a significantly fire-affected area of the continent. When using the SEVIRI observations that match to MODIS overpasses, fails to detect some of the ‘smaller’ fire clusters that MODIS does detect (e.g. in the western part of CAR). However, comparison of Figure 5.8a and 5.6c indicates that when all SEVIRI observations over the course of the 15-day study period are used, the spatio-temporal pattern of the SEVIRI-detected fires is very similar to those detected by MODIS – so most fires detected by MODIS are in fact detected by SEVIRI at some point in their lifetime. Thus by using all SEVIRI observations the spatial pattern and total number of individual fire events observed over any particular period is reproduced rather well. However, the fact that the signal of some of these fires goes undetected by SEVIRI at the time of the MODIS overpass [Figure 5.8 a and b] indicates the likelihood that, at any particular individual SEVIRI time slot, the instrument will only be detecting a fraction of the FRP that MODIS would have detected had it observed the area at the same moment. Thus, the total FRP derived from SEVIRI for a region at any given time will also be low biased when compared to MODIS



The detailed spatio-temporal performance of SEVIRI's fire detection capability was compared to that of MODIS in more detail for this area. In this section of the work the ‘full SEVIRI and MODIS datasets’ refer to all fire pixels detected within a  $15^\circ \times 15^\circ$  domain covering CAR between 01 and 13 Feb 2004. The ‘contemporaneous SEVIRI and MODIS datasets’ are a subset of the full datasets and include only those fire pixels detected at almost identical times ( $\pm 6$  minutes; remembering that a MODIS granule takes  $\sim 5$  minutes to collect and that SEVIRI collects a full image around every  $\sim 15$  minutes).



**Figure 5.9:** Effect of the inability of SEVIRI to detect low FRP fire pixels that MODIS can detect, illustrated by SEVIRI and MODIS fire detections collected over Central African Republic and surroundings in February 1-14 2004. Fire pixel detections are coloured by day of detection. When only using data from the SEVIRI imaging slots that were co-incident with a MODIS overpass, comparison of (b) with (a) confirms that SEVIRI misses a large number of (low FRP) fire pixels. However, it should also be noted that when using all SEVIRI imaging slots, SEVIRI appears to agree well in comparison to MODIS in terms of identifying the spatial distribution fire-affected areas, and in fact can detect a larger number of fires overall. The conclusion is that whilst many fires have an insufficiently high FRP to be detected by SEVIRI if we limit the SEVIRI observations to just those at the MODIS overpass time, most fires appear to become sufficiently large and intense at some point in their lifecycle that they will be successfully detected by SEVIRI.

First, a proximity analysis was performed using the contemporaneous datasets. The ground distance,  $\Delta d$ , was calculated between the centre of each contemporaneous MODIS fire pixel and the centres of all contemporaneous SEVIRI fire pixels. For each contemporaneous MODIS fire pixel, the minimum ground distance,  $\Delta d_{min}$ , was used to identify the nearest, temporally coincident SEVIRI fire pixel. Results presented in Figure 5.9 illustrate that 30%, 42%, and 53% of the contemporaneous MODIS fire pixels had a contemporaneous SEVIRI counterpart located within 3, 4, and 5 km, respectively. Approximately 10% of the contemporaneous MODIS fire pixels were quite isolated, however, and remained further than 20 km from the closest contemporaneous SEVIRI fire pixel.

The same proximity analysis was also performed using the full datasets. Here,  $\Delta d$  was calculated between each MODIS fire pixel and all SEVIRI fire pixels detected during the two week period. In contrast to the results for the contemporaneous matchups discussed above, Figure 5.9 illustrates that regardless of the time of either the SEVIRI

 	Land SAF VR-FRP	Doc: SAF/LAND/IM/VR_FRP/V_09 Issue: Version V/2009 Date: 18/10/2009
---	-----------------	---

or MODIS detection, 83%, 91%, and 95% of the MODIS fire pixels had a SEVIRI counterpart located within 3, 4, and 5 km, respectively. Furthermore, very few MODIS fire pixels remained isolated for the entire study period. Less than 1% of the full MODIS fire pixels failed to have a full SEVIRI counterpart located within 20 km of it.


Figure 5.9 thus demonstrates that although SEVIRI fails to detect a significant proportion of the active hotspots that are detectable by MODIS at the same time (i.e. at the time of an Aqua or Terra overpass), SEVIRI nevertheless detects a majority of these hotspots at some time during the study period. This performance is attributed to the increased sampling frequency of SEVIRI and the dynamic properties of fire and the other relevant natural phenomena (e.g. atmospheric properties, solar heating of the land surface etc). At any moment in time, the instantaneous state of a particular landscape fire, surrounding background and overlying atmosphere may not favour a positive fire detection by SEVIRI. Over time however, if the detection is warranted, the diurnal cycles of fire behaviour, land surface temperature, and atmospheric condition may provide multiple opportunities for a positive fire detection of the same event. The 15-minute repeat cycle of SEVIRI is well suited for capturing temporal fluctuations in fire behaviour, and is therefore well suited for capitalizing on these opportune moments.

Prior to identifying the times at which SEVIRI is more prone to detect an active hotspot within the vicinity of a MODIS fire pixel, it was first necessary to identify a set of collocated SEVIRI and MODIS fire pixels. Taking into account the point spread function and geolocation accuracies of each sensor, a distance of 4 km was subjectively selected to ensure an overlap between the SEVIRI and MODIS ground footprints. Hereafter the ‘collocated datasets’ refer to subsets of the full SEVIRI and MODIS fire pixels that are located within 4 km of one another. Incorporating this distance threshold revealed that 85% of all SEVIRI fire pixels in the full dataset were detected within 4 km of a MODIS fire pixel detected at any time in the study period. The remaining 15% of the “isolated” SEVIRI fire pixels are believed to represent a mix of the following situations: i) false alarms, ii) true landscape fires also detected by MODIS, but not classified as matching SEVIRI due to a broad ground footprint, large error in geolocation, or a ‘ghost fire pixel’ as a result of the SEVIRI spatial filtering operations, or iii) true landscape fires that were successfully detected by SEVIRI, but missed by MODIS.

The proportion of all SEVIRI fire pixels detected during a 24-hr period that were also collocated with MODIS fire pixels detected at some time during the study period ranged from 78% to 87% (sample size  $n = 13$ ). Furthermore, as a result of the diurnal cycle of fire activity, 88% of the collocated SEVIRI fire pixels were detected during the daytime between 0700 and 1900 UTC (Figure 5.10a).

A comparison between the collocated SEVIRI and MODIS detection times was less straight forward. Often there were multiple SEVIRI fire pixels and multiple SEVIRI



	Land SAF VR-FRP	Doc: SAF/LAND/IM/VR_FRP/V_09 Issue: Version V/2009 Date: 18/10/2009
---	-----------------	---

detection times associated with a single MODIS fire pixel. The former scenario occurred when a MODIS fire pixel was surrounded by a cluster of SEVIRI fire pixels, and the latter scenario occurred when the same SEVIRI pixel location was repeatedly flagged as a fire pixel during the study period. To account for this multiplicity, the time of SEVIRI fire detection that most closely matched the time of MODIS fire detection (i.e. the most contemporaneous SEVIRI fire detection) was selected to represent the time at which SEVIRI is likely to detect a hotspot also detected by MODIS.

Here the collocated MODIS detection times were subtracted from the most contemporaneous, collocated SEVIRI detection times, such that a positive time difference occurred if SEVIRI detected the same hotspot after the MODIS detection, and a negative time difference occurred if SEVIRI had detected the same hotspot before the MODIS detection. Figure 5.10b indicates that 70%, 79%, and 84% of the collocated MODIS fire pixels were detected by SEVIRI within 12, 24 and 36 hrs of the MODIS observation, respectively. The earlier detection of a fire by MODIS and the subsequent detection of SEVIRI is perhaps explained by a propagating flaming front and the subsequent increase in the fraction of the ground footprint occupied by combustion processes – thus the fire must become ‘large’ enough to be detectable by the sensor, and all other things being equal, this typically occurs for MODIS prior to SEVIRI due to its smaller pixel area that will consequently be more completely filled by fire for any particular fire size. On the other hand, the earlier detection of SEVIRI and the subsequent detection of MODIS (at least on the same day as the MODIS detection itself) may be attributed to the temporal advantage of the SEVIRI sampling scheme. Owing to the artefacts of the onboard spatial filtering, however, the detection of a hotspot by SEVIRI earlier than a day in advance of MODIS may be fortuitous.

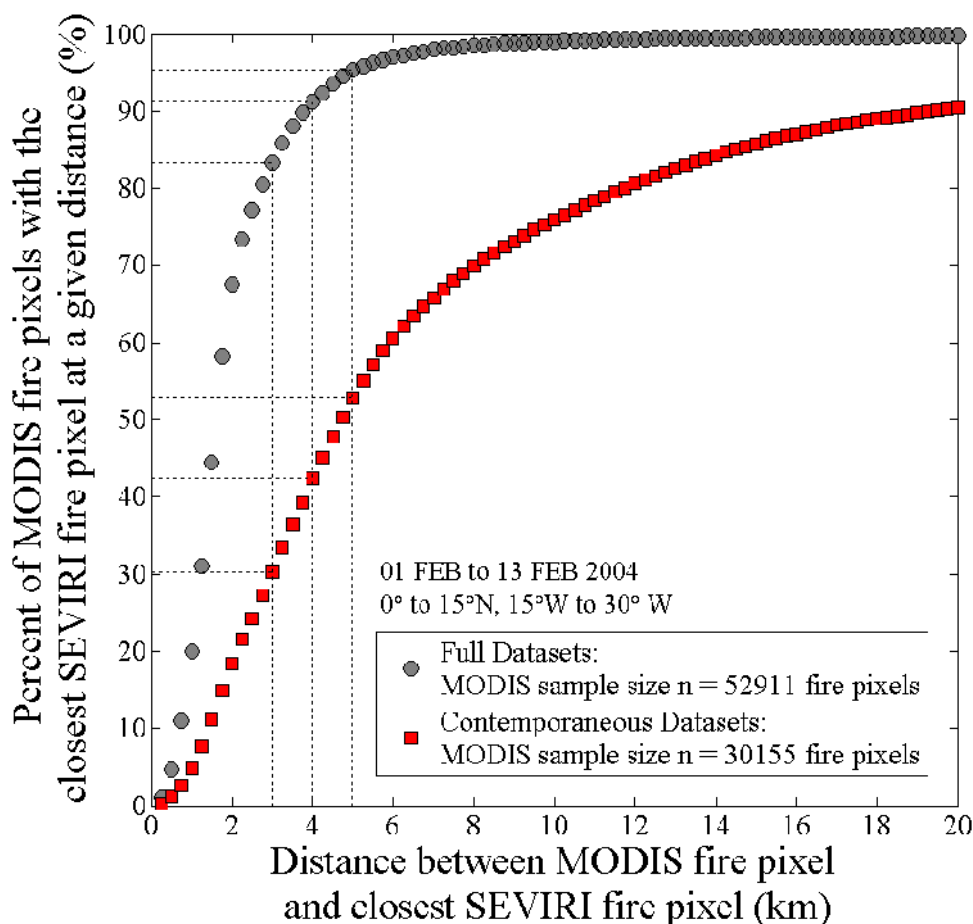


**Figure 5.9:** Results of the proximity analyses performed on the full (circle) and contemporaneous (square) datasets containing fire pixels detected in the region of CAR between 01 and 13 Feb 2004. For both cases the minimum ground distance was used to identify the SEVIRI fire pixel closest to each MODIS fire pixel. The difference between these two cumulative distributions indicates that for any given distance threshold, the ability of SEVIRI to detect a hotspot in the vicinity of a MODIS fire pixel can be improved by considering all SEVIRI fire pixels detected during the study period, not just those detected at the time of a MODIS overpass.

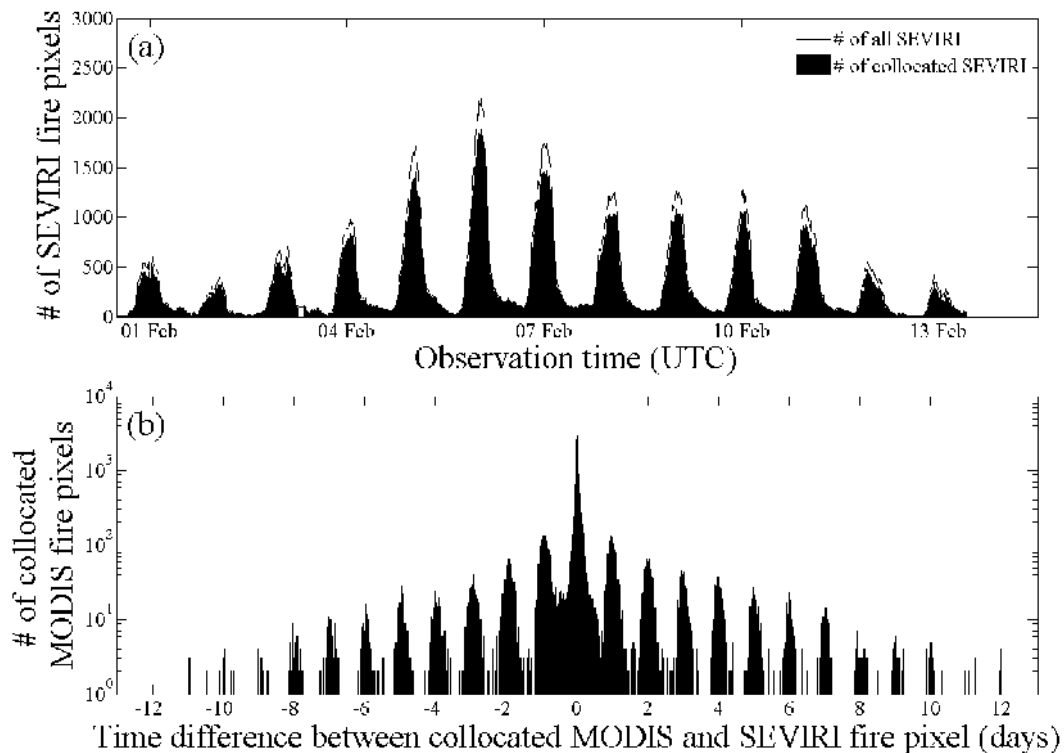
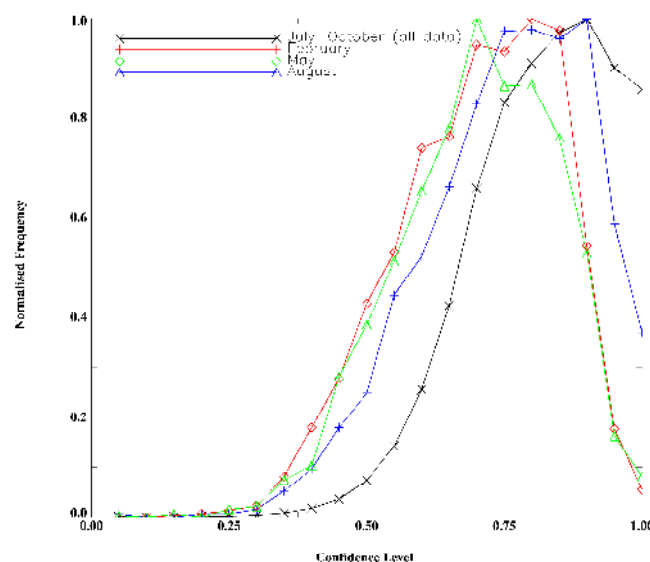


Figure 5.10: Results of the temporal analysis performed using the collocated SEVIRI and MODIS fire pixels detected in the region of CAR between 01 and 13 Feb 2004. In (a) is the number of SEVIRI fire pixels that were detected in each SEVIRI timeslot. Also in (a) is the number SEVIRI fire pixels that were detected in each SEVIRI timeslot and were within 4km of a MODIS fire pixel detected at any time during the study period. In (b) is a plot of the number of MODIS fire pixels detected within 4km of a SEVIRI fire pixel as a function of the time difference between the MODIS detection and the most contemporaneous SEVIRI detection. Note the log scale of the y-axis in (b).

Full results from the analysis of omission and commission, indicate that in February 2004, 54% of all MODIS-detected fire pixels over Africa (a total of 140,000 pixels) had no corresponding SEVIRI fire pixel. However, it should be remembered when interpreting these results that a large number of these MODIS pixels likely formed clusters such that several MODIS fire pixels correspond to only one ‘missing’ SEVIRI pixel. For May 2004 the equivalent results were 101,000 missed MODIS fire pixels (57%), and for August 198,000 fire pixels (57%). Corresponding errors of commission (false detections) by SEVIRI were rather small, at 6% (February), 8% (May) and 6% (August), a level comparable to the ~ 10% rate quoted for the TRMM active fire product (Giglio *et al.*, 2003a). The FRP of these false detections accounts for 3% (February), 6% (May) and 3% (August) of that months cumulative FRP total for the continent, indicating that the falsely detected fires have typically low FRP values.

In addition to its FRP, each detected fire pixel in the Land SAF and KCL FRP products has a confidence parameter attached, calculated as a function of the fires spectral signal above the background, its spatial location relative to clouds and water

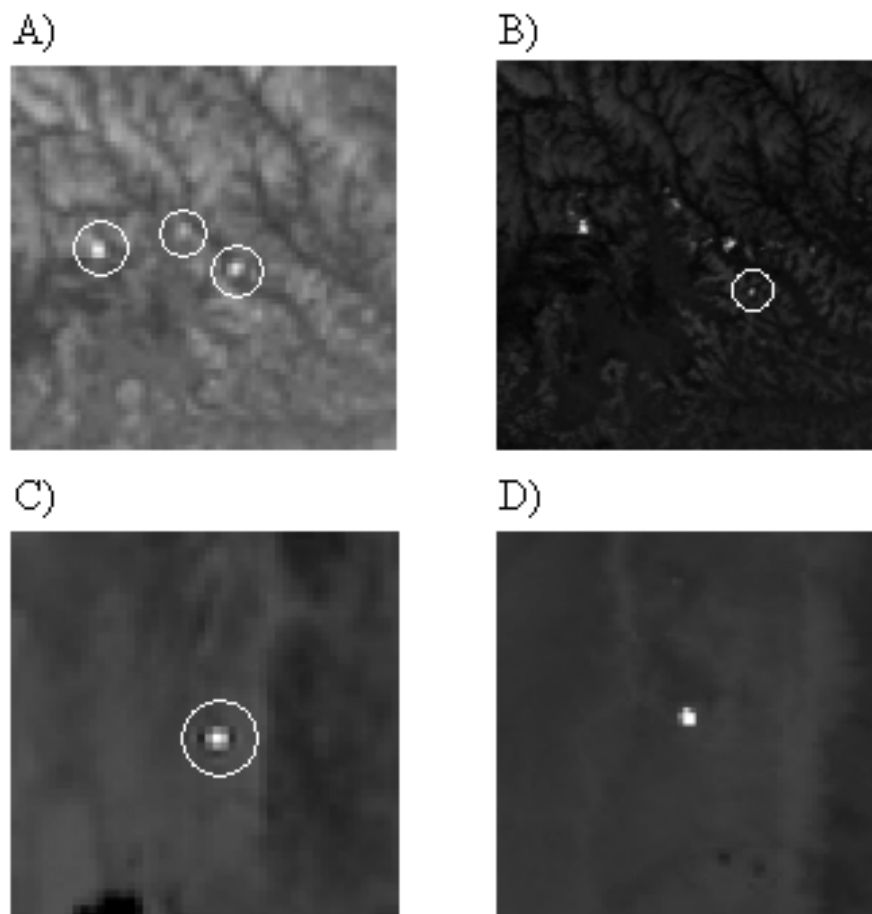
bodies, and series of other parameters detailed in Govaerts *et al.*, 2007. The statistical distribution of this fire pixel confidence parameter for the erroneously detected fire pixels identified in the February, May and August 2004 datasets discussed above is plotted in Figure 5.11 and compared to the confidence parameter of the set of correctly identified fire pixels. The similar degrees of commission error seen in each of the three months is reflected in the similar frequency distribution of the confidence parameter, though May has a distribution peaking towards a slightly lower confidence value, which reflects its slightly higher error of commission. The confidence values of the correct fire detections have a peak correctly shifted towards higher confidence values when compared to that of the false detections. However, it is not the case therefore that all fire pixels below a certain confidence limit can be automatically assumed to be false detections, since Figure 5.11 indicates that even some of the correctly identified fire pixels have confidence values lower than 0.5 for example. Such fire pixels are those most likely to be at the limit of detectability in terms of their spectral radiance signal above the background, and which maybe close to regions where false alarms are likely to be increased.





**Figure 5.11:** Frequency distribution of SEVIRI fire pixel detection confidence for all falsely detected fire pixels in February, May and August 2004, as compared to that of all fire pixels.

In fact, the majority of the false alarm fire pixels still have a confidence value exceeding 0.5, and this is mostly a result of the MIR brightness temperature limits used to define strong confidence and weak confidence fire pixels (Govaerts *et al.*, 2007), and the fact that the detection algorithm is designed only to confirm potential fire pixels as true fire pixels when there is a reasonable level of certainty that this is correct (i.e. to minimize errors of commission as far as possible; which has shown to be the case since levels of commission are < 10% even though low FRP fires at the very limit of detectability are in fact regularly distinguished by the algorithm). A similar effect relating to relatively high confidence values for false alarm fire pixels

has been noted in the MODIS fire products (Giglio *et al.*, 2005). Of course, a small fraction of the identified false alarm detections by SEVIRI may be due to MODIS incorrectly missing a fire. Morisette *et al.* (2005) indicate the strong performance of the MODIS fire detection product (using the version 4 algorithm), but Figure 5.12 illustrates two examples where we have found MODIS fire detection errors occur in comparison with a successful SEVIRI detection. Figure 5.12 (a-b) illustrates a case where SEVIRI detects three fires, whilst for some reason the MODIS MOD14 product only detects one fire. Figure 5.12 (c-d) highlights a further example where a MODIS pixel that clearly does contain an active fire is classified as a water pixel by the landcover map used in the MODIS fire detection procedure, and is therefore not passed through to the fire detection algorithm. This may possibly be a seasonal water body that in the dry season is the site of many fires.



**Figure 5.12:** Two examples where MODIS fire detection appears less sensitive than that of SEVIRI. (A) and (B) show, respectively, matching SEVIRI and MODIS night-time MIR channel images where fires are visible. White circles indicate the detected fires for each dataset. Of these, MODIS detects only one but SEVIRI all three. (C) and (D) again show, respectively, SEVIRI and MODIS MIR channel imagery which indicate the presence of a fire, which SEVIRI successfully detects. MODIS, however, fails to detect this fire, which appears to be due to the landcover of these pixels being (incorrectly) classed as water in the landcover map used by the MODIS fire detection algorithm. Although these results indicate that some errors of omission do exist in the MOD14 fire detections with respect to

 	Land SAF VR-FRP	Doc: SAF/LAND/IM/VR_FRP/V_09 Issue: Version V/2009 Date: 18/10/2009
---	-----------------	---

*SEVIRI, these are likely to be the exception rather than the norm since validation of the MOD 14 product using matching ASTER data indicates strong overall performance in this environment (Morisette *et al.*, 2005).*

### Sensor-to Sensor Per-Fire FRP Comparison

Figure 5.13 presents the results of the per-fire FRP comparison between fires that were successfully detected by SEVIRI and by MODIS, remembering that a fire maybe represented by different numbers of spatially contiguous fire pixels in the data of each sensor (an indeed is very likely to be, due to the sensors differing spatial resolutions). The per-fire FRP data generally show a strong level of agreement, with low bias but significant scatter. The observed scatter can result from a number causes, including:

- i) uncertainty in the ambient background characterization results of each sensor (Wooster *et al.*, 2005);
- ii) the small but potentially significant ( $\leq 6$  minutes) time difference between corresponding MODIS and SEVIRI observations of the same fire, during which time fire characteristics may have changed significantly;
- iii) variation in retrieved FRP related to the sub-pixel location of the fire with respect to the sensor IFOV and point spread function, and the impact of the filtering operations conducted during the production of SEVIRI level 1.5 data;
- iv) the fact that ‘fire pixels’ have to have a significantly higher minimum FRP to be detected by SEVIRI than by MODIS, but more of the overall radiance contribution from a fire maybe contained within a SEVIRI pixel than a MODIS pixel, and so on a case-by-case basis, certain of the individual pixels making up a fire may remain undetected by SEVIRI but detected by MODIS, or visa versa.
- v) the assumption of greybody emission from fires being significantly in error, and the spectrally varying emissivity interacting in such as way with the MIR channel sensor spectral response funcing that differences in retrieved FRP resulted.
- vi) the effects of sensor saturation in some of the detected fire pixels

Figure 5.13 indicates that the level of per-fire FRP agreement is lower for fires with a MODIS-derived FRP exceeding 3000 MW, which correspond to unusually large and/or intensely burning fires that are most likely subject to the effects of SEVIRI MIR detector saturation (Roberts *et al.*, 2005), and which is analysed in Section 0. Fortunately, the incidence of such fires is rather low, so the effect of SEVIRI pixel saturation is limited when considering all fires made over larger regions, and certainly is much less important than the fact that SEVIRI misses many of the lower FRP fire pixels that MODIS can detect.

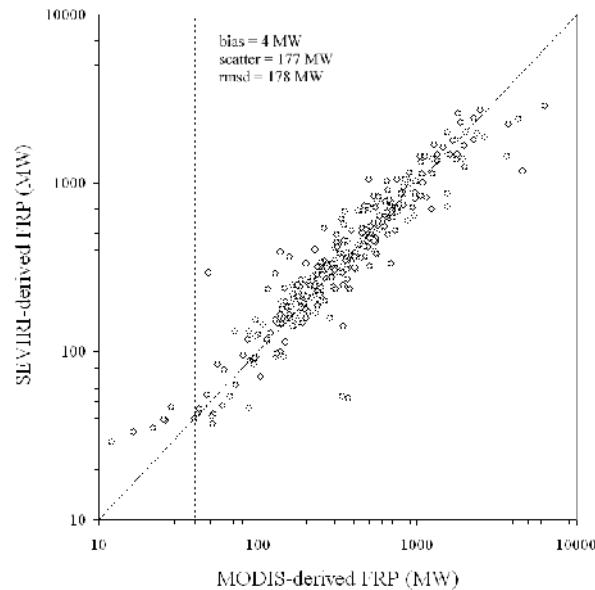



**Figure 5.13:** A comparison of per-fire FRP derived from SEVIRI and MODIS observations of 289 fires observed near-simultaneously by each sensor in February, May and August 2004. Fires are designated as contiguous clusters of active fire pixels. Correlation between the two datasets is quite strong ( $r^2 = 0.62$ ,  $p < 0.0001$ ) but there is clear evidence that SEVIRI overestimates FRP for fires where the MODIS-derived FRP is  $< \sim 40$  MW, and underestimates FRP for fires where the MODIS-derived FRP is  $> \sim 3000$  MW. Discounting these 17 cases increases the strength of the correlation significantly ( $r^2 = 0.87$ ,  $p < 0.0001$ ).

A further effect that mostly impacts retrievals over high-FRP fires is that the SCE cloud mask sometimes flags the thick smoke from particularly large fires as cloud. In the MIR it is possible to detect fire pixels through such smoke, but because the site of the fire pixel is flagged as cloud in the cloud mask, it will remain undetected. Visual inspection of a number of large fires indicates such occurrences are rare, but do occur and contribute to the increased FRP underestimation over the highest FRP fires.

The agreement between the MODIS- and SEVIRI-derived per-fire FRP is also considerably worsened for fire fires detected by SEVIRI where the MODIS-derived FRP was less than 40 MW. Such fires correspond to a SEVIRI MIR brightness temperature increase of only a few Kelvin above the background ( $\sim 2 - 3$  K, depending on the ambient temperature and levels of incoming solar radiation), thus indicating that they are at the very limit of the detectability envelope seen in and are also most subject to the additive errors introduced by uncertainty in the ambient background characterisation. Considering all 289 matchups presented in Figure 5.13, 76% of the MODIS and SEVIRI FRP values agree to within 33%, a proportion that increases to 79% when considering those fires whose FRP as derived from MODIS fell within the  $40 \text{ MW} < \text{FRP} < 3000 \text{ MW}$  limit. Within this limit the data show minimum bias with respect to MODIS (only 3.7 MW between the SEVIRI- and MODIS-derived per-pixel FRP measures).



	Land SAF VR-FRP	Doc: SAF/LAND/IM/VR_FRP/V_09 Issue: Version V/2009 Date: 18/10/2009
---	-----------------	---

## 5.2.2 Effect of Spatial Resolution – Area Based Comparisons

### Basic Results

Figure 5.14 presents the results of the regional-scale cumulative FRP comparisons, with each point representing the total FRP observed by MODIS and SEVIRI at the time of a MODIS overpass and within the area covered by the entire MODIS swath. This area-based cumulative FRP is clearly underestimated by SEVIRI with respect to MODIS (i.e. the gradient of the lines of best fit are  $< 1.0$ ), and this underestimation is due to SEVIRI's inability to detect the lowest FRP fire pixels, many of which MODIS can detect due to its significantly higher spatial resolution as already demonstrated.

Since the proportion of low-to-high FRP fire pixels varies between each MODIS image (depending presumably on time of acquisition and its interplay with the fire diurnal cycle, and location of acquisition and its interplay with landcover/landuse) the level of agreement between the cumulative inter-scene FRP recorded by SEVIRI and MODIS also varies, resulting in a significant scatter (as indicated by  $r^2 < 1.0$ ). Nevertheless, the relationship between SEVIRI- and MODIS-derived FRP is quite strong in each case, and the relatively high degree of similarity in the results from the different months and areas (e.g. in terms of the slope of the OLS line of best fit, the RMSE and  $r^2$  coefficient) indicates a degree of consistency in the fire regime and algorithm performance across Africa as a whole. The total FRP measures obtained by accumulating data from the entire month of matched SEVIRI and whole-swath MODIS imagery indicates a SEVIRI-to-MODIS monthly cumulative FRP ratio of 0.57 (Feb), 0.60 (May) and 0.55 (Aug), again indicating a high degree of consistency between months.


Looking in detail at Figure 5.14, it is apparent that in some cases SEVIRI underestimates regional FRP by more than 50% compared to MODIS. The most significant cases turn out to be a consequence of small, scattered clouds and the fact that the cloud mask used in the production of the MOD14 fire product is of a higher spatial resolution than that of SEVIRI, and also appears less conservative in that it sometimes fails to mask smaller clouds and cloud edges (Giglio *et al.*, 2003a). This typically results in a greater proportion of pixels being flagged as cloud contaminated by SEVIRI than by MODIS, and also allows MODIS to correctly identify active fire pixels occurring between closely spaced clouds in a higher proportion of cases. In the remaining examples, thin clouds and/or heavy aerosols covered large areas, and the Stage 2 SEVIRI MIR/RED radiance ratio test detailed in ATBD caused a number of low FRP fire pixels to remain undetected in these cases.

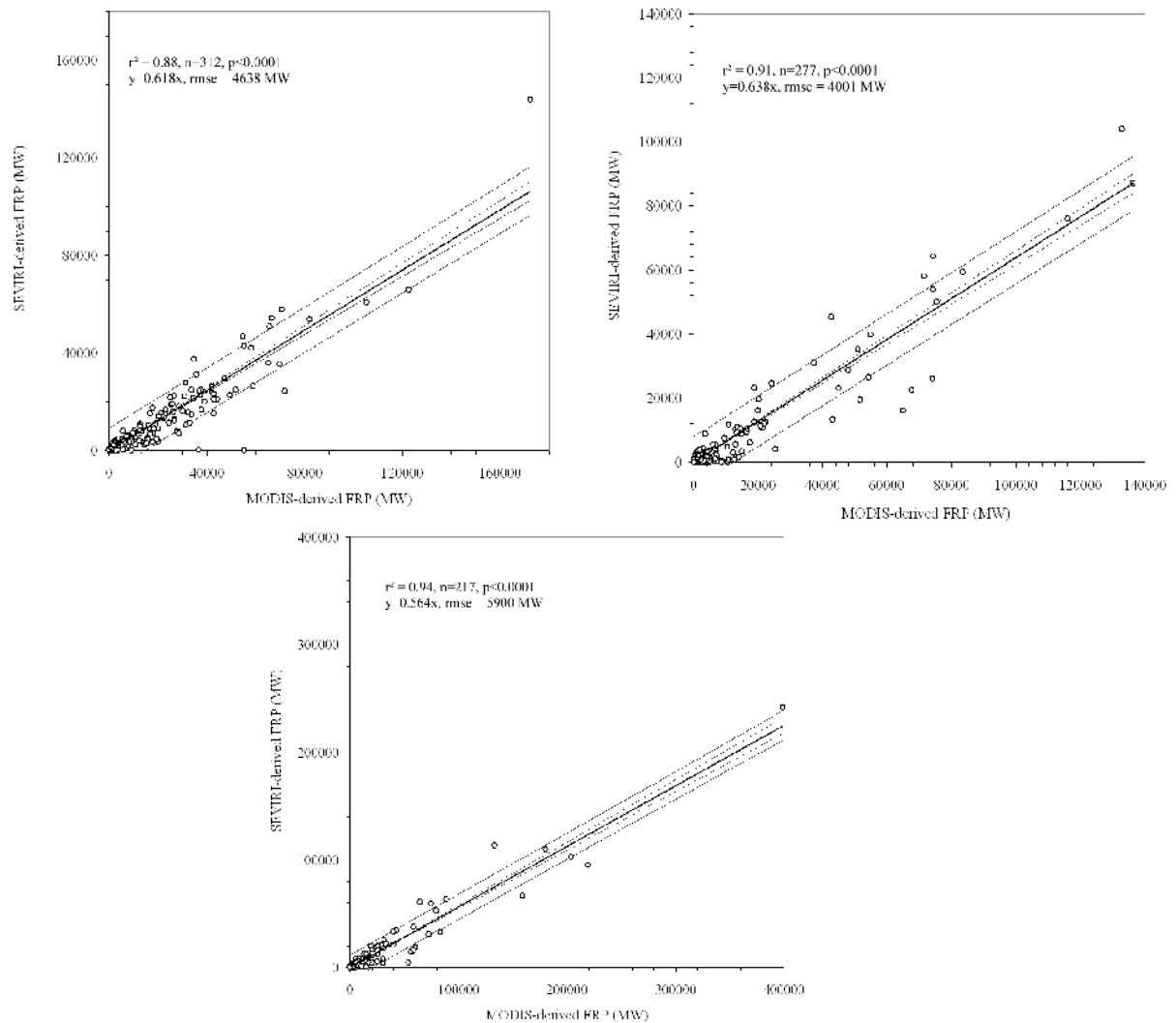


**Figure 5.14:** Relationship between regional-scale inter-scene FRP derived from all spatially matched, contemporaneous SEVIRI and MODIS observations for, from top left clockwise, February, May, and August 2004. Data are taken from across the African continent in each case, but fires are concentrated in north, central and southern Africa respectively. The data were taken from the entire MODIS swath, between nadir and  $55^\circ$  scan angle, and the area of the relevant contemporaneous SEVIRI image was spatially subset to reflect the same geographic coverage. The OLS linear best-fit passing through the origin is shown (bold line), along with the 95% confidence intervals on the mean (dotted line) and on the prediction of y from x (outermost lines). In each case SEVIRI generally underestimates regional-scale FRP, primarily due to the non-detection of the lowest FRP fire pixels, many of which MODIS can detect.

#### Detailed Sensor-to-Sensor Comparisons of Fire Activity Over the Annual Cycle

Of all SEVIRI scans and MODIS overpasses in the year between February 2004 and January 2005 there were 2239 timeslots in which both sensors concurrently ( $\pm 6$  minutes) observed a portion of Africa. No fire pixel in the training dataset exists between 0300 and 0630 GMT nor between 1500 and 1900 GMT, due to the absence

	Land SAF VR-FRP	Doc: SAF/LAND/IM/VR_FRP/V_09 Issue: Version V/2009 Date: 18/10/2009
---	-----------------	---

of a MODIS overpass. Daytime detections accounted for 95% of the total fire counts and 96% of the total FRP within in the training dataset for both MODIS and SEVIRI. Overall SEVIRI detected 20% of the total yearly fire pixel count, and measured 50% of the total yearly FRP compared to MODIS.

Ratios of fire pixel count and FRP were most variable at the instantaneous scale and ranged from 0.0 to 1.27 and from 0.0 to 4.86, respectively ('observation ratios'  $\phi_{count}$  and  $\phi_{FRP}$  in Figure 5.15). This variability in  $\phi_{count}$  and  $\phi_{FRP}$  between consecutive MODIS observations is attributed to the following: i) the dynamic nature and diurnal cycle of fire behaviour, ii) the timing and ground track of the MODIS overpass, iii) the different measured frequency-magnitude distributions associated with fire activity, and iv) the occasionally limited sample of fire pixels used to calculate  $\phi_{count}$  and  $\phi_{FRP}$ . The temporal profiles already presented in 4.3 demonstrate the combined effects of the MODIS overpass time, ground track, and swath width on the diurnal cycle of measured FRP.

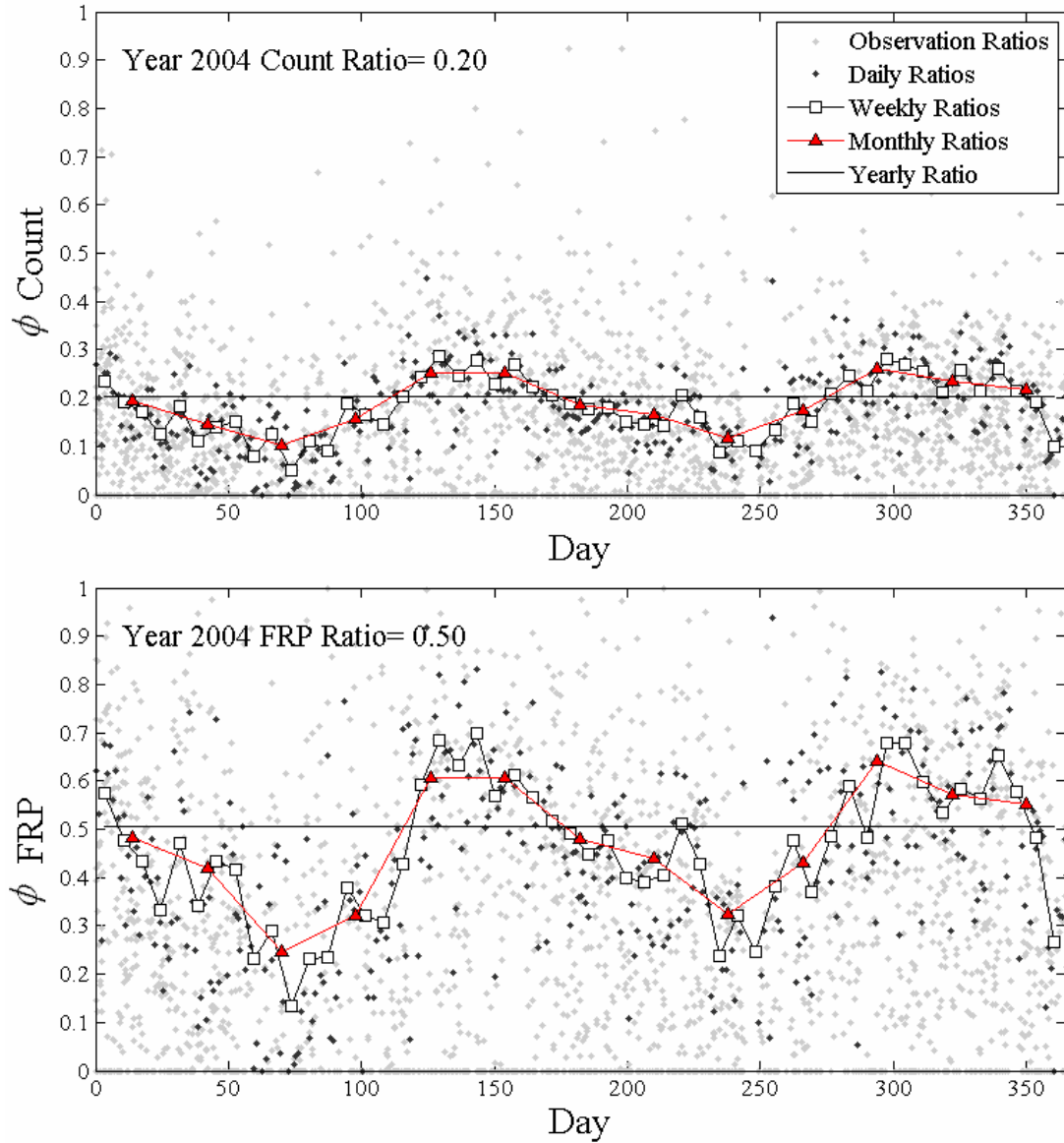


**Figure 5.15:** Temporal profiles in the ratios between SEVIRI and MODIS of fire pixel count, ( $\phi_{Count}$ ) and FRP ( $\phi_{FRP}$ ). Using fire pixels within the training dataset, the ratios are calculated within five temporal windows ranging from the instantaneous scale to one year.


Figure 5.16 shows the distribution of  $\phi_{FRP}$  with respect to the FRP measured by SEVIRI and by MODIS. Of note are the two extreme groups of observations with  $\phi_{FRP}$  greater than 1.0 and  $\phi_{FRP}$  less than 0.1. Though each cluster spans three orders of magnitude, the range of  $FRP_{SEVIRI}$  with  $\phi_{FRP} > 1.0$  was shifted an order of magnitude higher than the range of  $FRP_{SEVIRI}$  for which  $\phi_{FRP} < 0.1$ , while for the MODIS data the opposite behaviour is observed. The characteristics of these two clusters are separated as follows:

- For an identical value of scene-integrated  $FRP_{SEVIRI}$ , observations with  $\phi_{FRP}$  less than 0.1 had a greater absolute number of MODIS detections as well as lower fire pixel count ratios. Furthermore 52% of the observations with  $\phi_{FRP} < 0.1$  had frequency magnitude distributions that were composed entirely of SEVIRI fire pixels less than 56 MW.
- The scenario at which  $FRP_{SEVIRI}$  was 4.9 times greater than  $FRP_{MODIS}$  occurred at an observation with a low absolute number of MODIS detections ( $n_{MODIS} = 9$ ), a high count ratio ( $\phi_{FRP} = 0.78$ ), and captured a thermal distribution in which pixels greater than 56 MW accounted for 90% of  $FRP_{SEVIRI}$ .

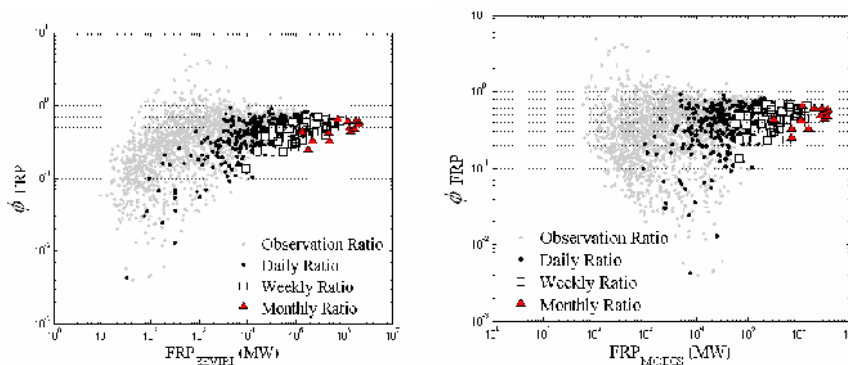


**Figure 5.16:** Ratios of FRP,  $\phi_{FRP}$ , as a function of the FRP measured by SEVIRI (left) and MODIS (right). Ratios are identical to those presented in Figure 5.15, and are separated by the width of the temporal window in which the fire pixels were aggregated; either on an observational ( $n=2239$ ), daily ( $n=365$ ), weekly ( $n=52$ ), or monthly basis ( $n=12$ ).

Given the variability of the instantaneous ratios in the training dataset, and the limited number of MODIS overpasses in a single day, diurnal cycles of  $\phi_{count}$  and  $\phi_{FRP}$  could not easily be discerned. However, seasonal patterns of  $\phi_{count}$  and  $\phi_{FRP}$  were discerned after accumulating fire pixels into non-overlapping intervals of one-day, one-week, and four-weeks (Figure 5.15 and Figure 5.16). The variability of the instantaneous ratios narrowed as more in-scene radiant energy was measured; and as an example  $\phi_{FRP}$  converged from over four orders of magnitude between low and moderate measures of  $FRP_{SEVIRI}$  to values within 0.4 and 0.9 for temporally aggregated measures of  $FRP_{SEVIRI}$  greater than  $1 \times 10^5$  MW (Figure 5.16a). The temporal superposition of the frequency magnitude distributions not only enhanced the thermal signal above the background, but due to the overpass times and the ground tracks of the MODIS swath, the wider temporal windows coalesced the ratios that were calculated i) at different times in the diurnal cycle of fire behaviour, and ii) at different geographic locations. Thus the extreme variability in the ratios at the instantaneous scale was moderated as the temporal window was widened, and this effect can be most clearly seen in Figure 5.15. Temporal windows above that of the individual MODIS observations include data from all four MODIS passes typically available for any particular location per day (i.e. 1:30am; 10:30am; 1:30pm and 10:30pm local equator crossing time).

	Land SAF VR-FRP	Doc: SAF/LAND/IM/VR_FRP/V_09 Issue: Version V/2009 Date: 18/10/2009
---	-----------------	---

Weekly and monthly ratios of  $\phi_{count}$  and  $\phi_{FRP}$  are shown to vary with the total FRP detected by SEVIRI, but the relationship is imperfect (e.g. Figure 5.156a), and analysis of the seasonal trend in ratios shows that they are loosely coupled to the migration of fire activity over the continent. In Figure 5.15 the elevated ratios ( $\phi_{count} > 0.2$  and  $\phi_{FRP} > 0.5$ ) seen at the beginning of February 2005 (Day 1) and also at the end of November through December (Days 300 – 336) are associated with fire activity in the latitudinal belt between 3 and 12° N in Sierra Leone, Guinea, Ghana, and in particular in Central African Republic and Sudan. Similarly, elevated ratios of  $\phi_{count}$  and  $\phi_{FRP}$  in June and July (Days 125 – 175) are associated with the latitudinal belt between 4 and 20 °S, and in particular the northern part of Angola. The depressed ratios ( $\phi_{count} < 0.2$  and  $\phi_{FRP} < 0.5$ ) correspond to the weaker fire activity during the transition between the Northern and Southern hemispheres.

Yearly ratios calculated at 5.0, 1.0 and 0.25° grid cell resolutions illustrate the spatial patterns of  $\phi_{count}$  and  $\phi_{FRP}$  across the African continent (Figure 5.17). Again the relationships between the absolute number of fire pixel counts and  $\phi_{count}$  and between FRP and  $\phi_{FRP}$  were relatively weak. As described above, the ratios at different locations were representative only of the time in which the areas burned. Grid cells at 5.0° resolution were large enough to span different land cover types, land use practices, and ultimately fire regimes and therefore fail in some respects to adequately capture the inherent spatial variability of the ratios. Conversely however, a higher grid cell resolution can result in noisy ratios that fail to obtain enough samples to reduce the inherent scene-to-scene variability (a feature analogous to the temporal sampling issues demonstrated in Figure 5.15). Similar to the expansion of the temporal window demonstrated there, the aggregation of fire activity within relatively large 5.0° grid cells moderated the ratios that otherwise can be dominated by localized hotspots at sub-5.0° grid cell resolutions.



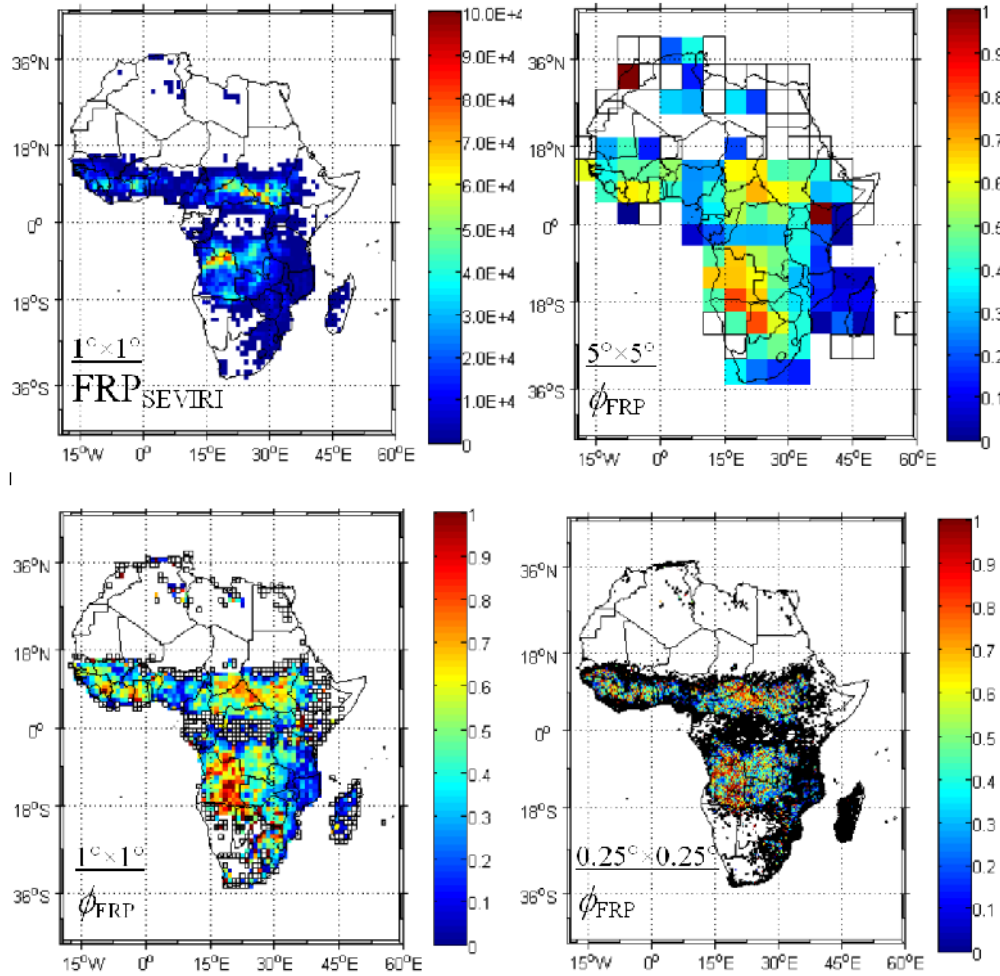


**Figure 5.17:** Yearly sum of  $FRP_{SEVIRI}$  at  $1^\circ$  grid cell resolution (upper left) and yearly ratios of  $FRP_{SEVIRI}$  to  $FRP_{MODIS}$  ( $\phi_{FRP}$ ) evaluated at 5.0, 1.0 and  $0.25^\circ$  grid cell resolutions. Open boxes with solid black outlines indicate null ratios where MODIS detected at least one fire pixel, but SEVIRI did not.

In Figure 5.17, clear spatial patterns in  $\phi_{count}$  and  $\phi_{FRP}$  become visually distinguishable at the  $1.0^\circ$  grid cell resolution, as compared to the  $5.0^\circ$  resolution. Furthermore, as with the lower density of fire pixels that surround regions of high fire activity, a higher number of grid cells at this finer spatial resolution had null ratios where MODIS detected fire pixels, but SEVIRI did not (indicated by the open boxes). Of note in Figure 5.17 is that the spatial pattern of  $\phi_{FRP}$  at  $0.25^\circ$  resolution becomes rather noisy, with the variability reinforced due to the smaller sample size that is influenced more by individual combustion events. At this spatial scale, the finest tested here, the small grid cell size and uncertainties in the registration of the fire pixel centres also become increasingly important. Fire pixels that in actuality represent the same fire on the ground might be successfully detected by SEVIRI and MODIS, but at this grid-cell size there is an increased chance they could be erroneously located in different (adjacent) grid cells.




Potential Adjustment of SEVIRI Gridded FRP Data for the Effect of Undetected Fires

In contrast to the preliminary analysis that revealed a power-law function as the underlying relationship between SEVIRI and MODIS at the continental scale, the notion of a power-law dissipated once fire pixels were separated into the four independent LSA SAF regions. For instance, for the southern hemisphere of Africa (i.e., SAfr), the best-fit power law yielded an exponent of  $1.012 \pm .04$ , which was not significantly different than 1 (Figure 5.18). These results suggest that a simple linear regression has statistically similar predictive capabilities as a power function. Hence for the remainder of the analysis the coefficient  $\beta$  was set to a constant of 1.0, and only the parameter  $\alpha$  was used to adjust SEVIRI observations of FRP.

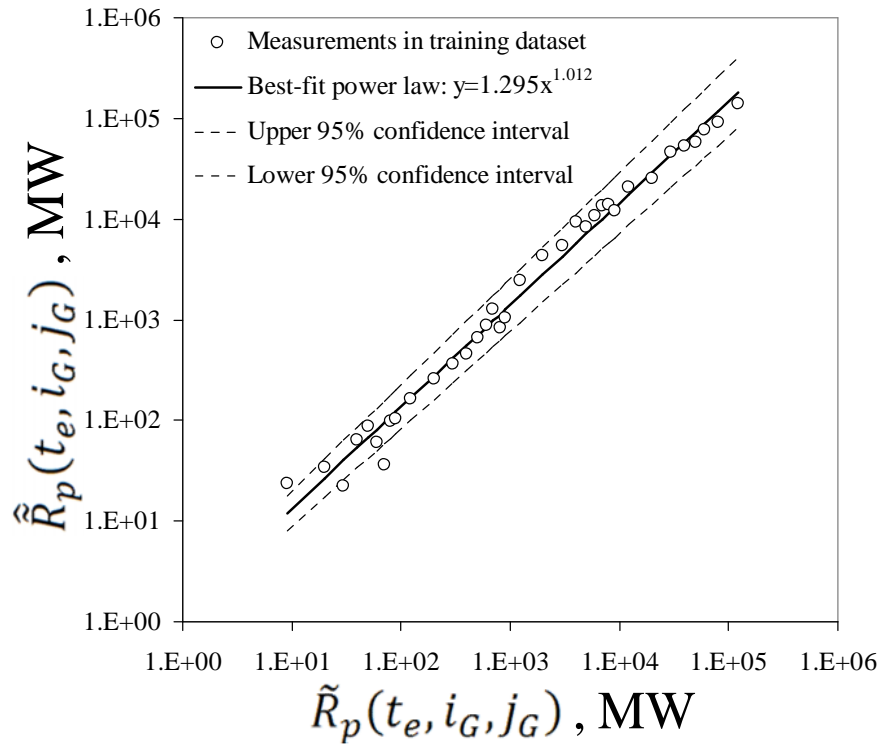


**Figure 5.18:** Relationship between the FRP measured by SEVIRI and MODIS for the southern hemisphere of Africa. The pixel level FRP was summed in  $5.0^\circ$  grid cells and the average was calculated at hourly temporal resolution according to Equation 9. The SEVIRI measurements were then binned and compared to the median value of the MODIS observations. The best-fit power law (shown with the 95% confidence intervals) indicates that the exponent is not significantly different than 1.0; therefore a simple linear regression would suffice at the regional scale.

Since it is expected that SEVIRI observations of FRP will be accumulated and adjusted every hour within  $5.0^\circ$  grid cells, the parameter  $\alpha$  was selected to provide an unbiased estimate of the FRP potentially observed by MODIS at this specific spatio-temporal resolution. In both the northern and southern regions of Africa there were a

	Land SAF VR-FRP	Doc: SAF/LAND/IM/VR_FRP/V_09 Issue: Version V/2009 Date: 18/10/2009
---	-----------------	---

sufficient number of observations of high fire activity at 5.0° grid cell resolution and hourly temporal resolution to (i) extend the range of FRP measured by SEVIRI and MODIS, and (ii) enable the development of statistically significant relationships between SEVIRI and MODIS. Ironically in order to obtain these high FRP observations implies that an even greater number of low FRP observations were also included in the training dataset. This sampling artefact is attributed to the right-skewed, heavy tailed distributions of FRP that are observed across the landscape. For example, consider the tracking over time of the true FRP emitted by a landscape fire within a frequency-magnitude distribution (c.f., Figure 4.4). The fire first begins in a low FRP bin upon ignition, then moves upwards through higher bins until it reaches a maximum radiative output during a peak in intensity or areal extent; after which it reverses direction along the abscissa and then moves downwards through lower FRP bins as the radiant power decays until it finally extinguishes. Not all cool fires eventually become the hottest fires, however, since the maximum FRP achieved by a fire depends on the fuel load and the spread rate, and thus the fuel consumption rate, all of which vary over the landscape and with weather conditions. Fast spreading fires in high fuel loads have a lower probability of developing and are therefore considered extreme event scenarios. Furthermore, the duration that a fire pixel exists above a certain threshold of FRP (or brightness temperature) decreases as the threshold increases. A fire pixel maintains maximum radiative output only briefly compared to the residence time of all combustion activity. For example consider the diurnal cycle of FRP for a single day (c.f., Figure 4.3). The time that a fire exists above half of its maximum value of FRP ( $0.5FRP_{max}$ ) is considerably shorter than the time a fire exists below  $0.5FRP_{max}$ . Thus there is a greater probability that a measurement will be collected either (i) along the leading edge of the ramp, or (ii) during prolonged episodes of thermally decay.

To account for the disproportionately greater number of observations of low FRP and the increased variance in FRP associated with observations of high fire activity, a weighted least squares (WLS) routine was performed to retrieve the parameter  $\alpha$ . The training relationships between the hourly average of FRP estimated by SEVIRI and the FRP estimated by MODIS are presented for all four LSA SAF regions in Figure 5.19). For completeness, a summary of the outputs from the WLS routine is also presented in Table 5.1.

At SEVIRI observations of low FRP the WLS routine (with the intercept set to zero) performs well at capturing the median value of the corresponding MODIS observations. That is for SEVIRI measurement of low FRP, the WLS routine identifies the MODIS value of FRP at which 50% of the observations were above and below this value. Furthermore, at SEVIRI observations of low FRP the MODIS distributions of FRP about the regression line tend to deviate further from Gaussian. Consequently the WLS prediction tends to underestimate the mean value of the corresponding MODIS measurements of FRP. It should also be noted that although the high FRP observations in NAfr and SAfr were necessary to extend the range of FRP, these cases were weighted less in the WLS routine due to their increased variance, and therefore had relatively less influence on the retrieval of  $\alpha$ .

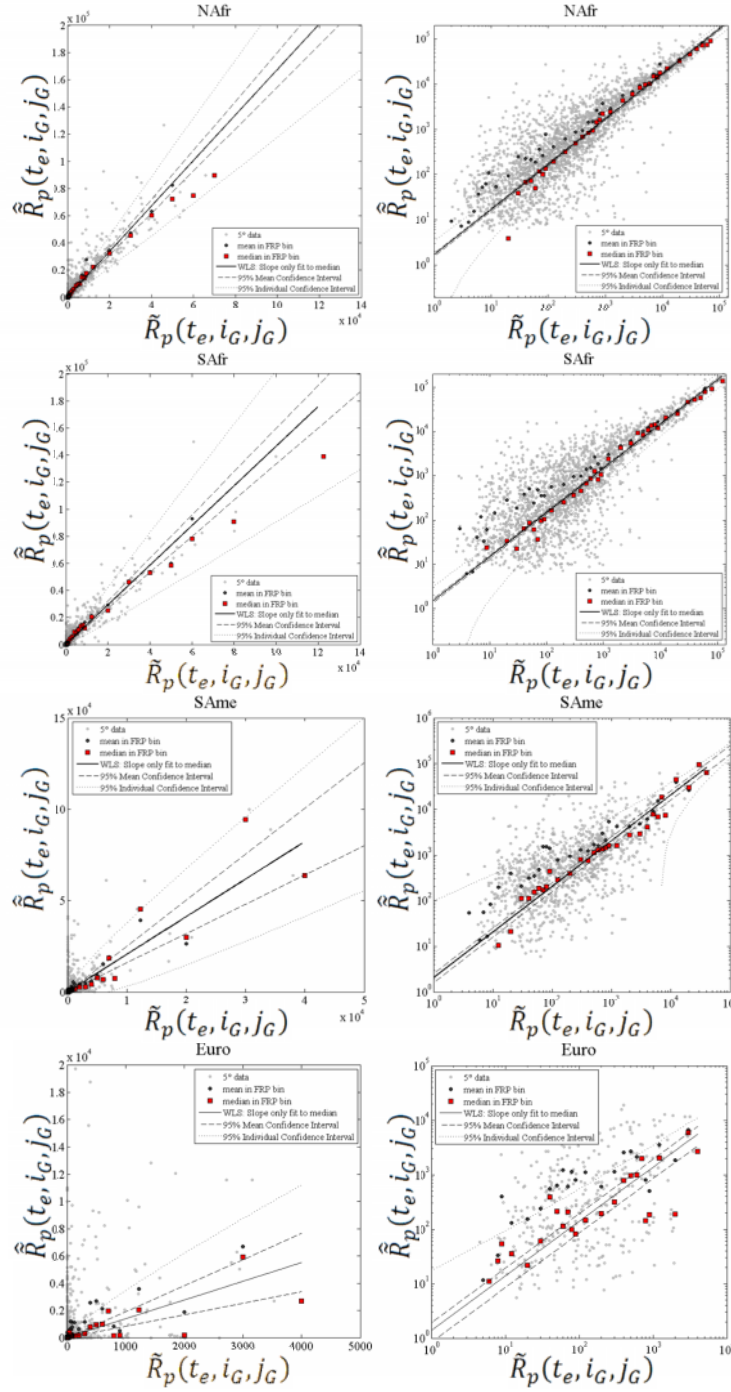


**Figure 5.19:** Training relationships between the FRP measured by SEVIRI and MODIS for all four LSA SAF regions. The pixel level FRP was summed in  $5.0^\circ$  grid cells and the average was calculated at hourly temporal resolution according to Equation 9. The hourly comparisons (gray circles) were then binned and compared to the median (red squares) and mean (black circles) values of the MODIS observations. Also shown is the best-fit WLS estimate (solid line) and the 95% mean (dashed line) and individual (dotted line) confidence intervals. A summary of the parameters for the WLS models can be found in Table 5.1.

**Table 5.1:** Results of the WLS routine and validation procedure.

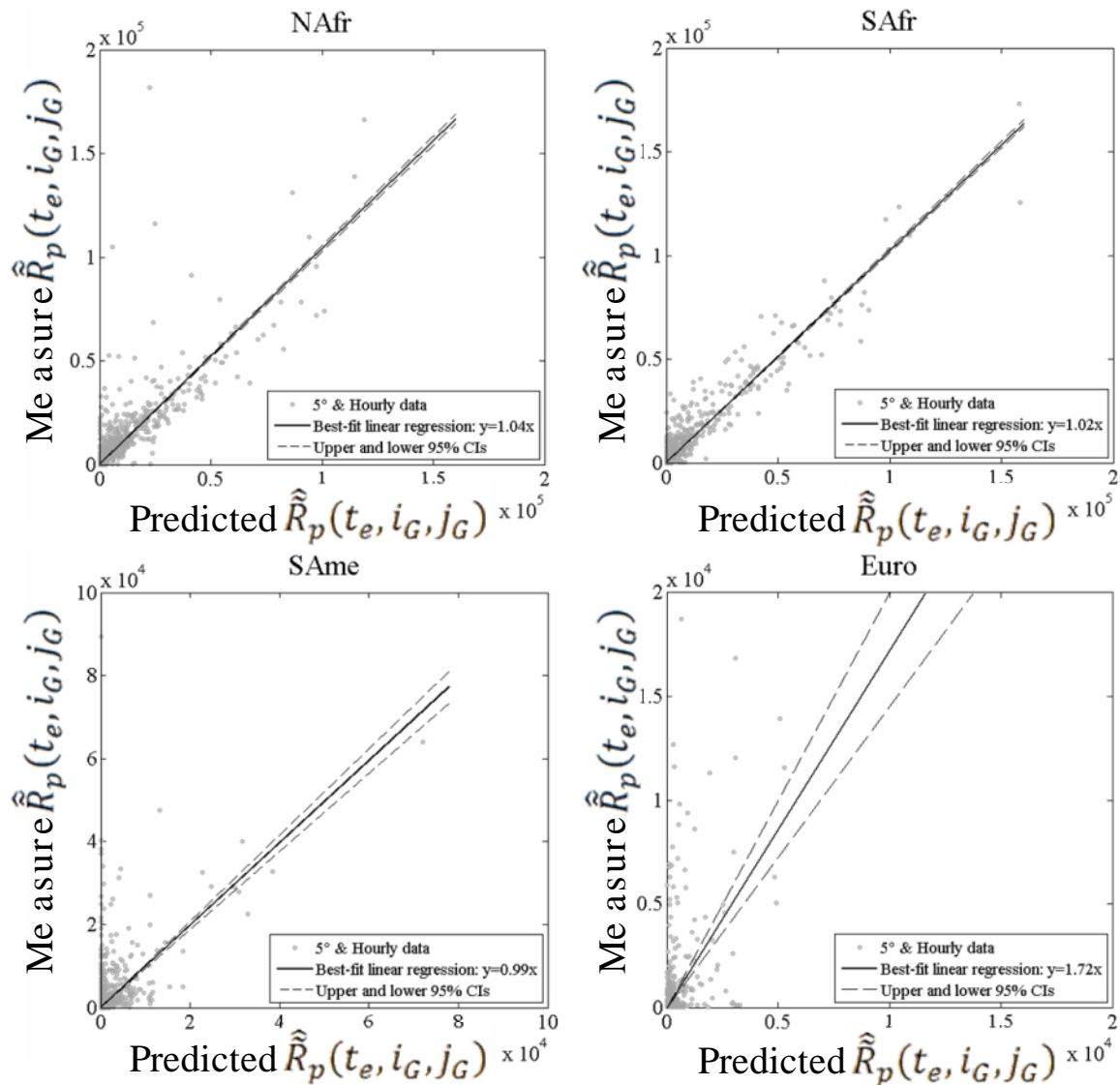
LSA SAF Region	Abbreviation	WLS parameter estimates (standard error)		Validation Results at 5° and hourly resolution	Validation Results at region and weekly resolution
		$\alpha$	$\beta$	Bias ( $R^2$ )	Bias ( $R^2$ )
northern Africa	nAfr	1.674 ( $\pm 0.062$ )	1.0 (0.0)	1.04 (0.76)	1.15 (0.96)
southern Africa	sAfr	1.464 ( $\pm 0.065$ )	1.0 (0.0)	1.02 (0.91)	1.24 (0.97)
South America	SAme	2.057 ( $\pm 0.224$ )	1.0 (0.0)	0.97 (0.34)	1.89 (0.83)
Europe	Euro	1.377 ( $\pm 0.173$ )	1.0 (0.0)	1.72 (.185)	4.94 (.84)

Similar WLS models were developed for the LSA SAF regions encompassing South America (SAme) and Europe (Euro). In both regions the raw relationships between the FRP observed by SEVIRI and MODIS were considerably weaker than those previously found for the continent of Africa. This is primarily attributed to (i) the lack of observations of high fire activity, (ii) the fewer number of overall fire pixel detections, and (iii) the lower absolute magnitude of the aggregated FRP measured in each 5.0° grid cell. Additionally, in both regions, MODIS frequently detected a substantial amount of FRP when SEVIRI did not detect a single fire pixel. In contrast to similar scenarios that occurred over Africa, these inconsistencies were not isolated to observations of relatively low fire activity. Such artefacts are attributed to the following:

- (1) The often extreme view angles associated with the SEVIRI observation coupled with a near-nadir observation by MODIS.
- (2) Sensor-to-sensor differences in the performance of the fire detection algorithms in the presence of increased cloud fractions.
- (3) Differences in fire behaviour, canopy cover, and terrain between the regions



As with the regions in Africa, however, these artefacts were mitigated by binning the FRP data and forcing the linear regressions through the origin. As with the results of the WLS routine in Africa, as well, the parameter  $\alpha$  adequately captures the median response of MODIS.

The predictive capabilities of the WLS coefficients for each LSA SAF region were next evaluated by applying the training values of  $\alpha$  to the validation dataset. In both regions of Africa the predictions yielded unbiased estimates of the instantaneous FRP that would have been measured by MODIS at 5.0° spatial resolution (Figure 5.20). A summary of the validation results is also presented in Table 5.1. As expected, however, the coefficients of  $\alpha$  for SAme and Euro did not perform as well. Although  $\alpha$  provides an unbiased estimate of the FRP that MODIS would have measured in South America, the correlation coefficient ( $R^2$ ) was considerably less than those for the regions in Africa, thus limiting the predictive capability of the model at this spatio-temporal resolution. The correlation can be improved by only considering observations of moderate fire activity. For example in SAme, by removing 5.0° grid cells in which only one sensor detected fire pixels (i.e., thereby forcing a comparison between observations in which SEVIRI and MODIS viewed a fire) the  $R^2$  improved to 0.43. Furthermore, by removing a lone outlier improved the correlation coefficient slightly further to 0.55. Likewise for Euro, only including observations in which SEVIRI and MODIS simultaneously detected a fire pixel yielded in  $R^2$  of 0.31.



**Figure 5.20:** Performance of the WLS estimates during the validation exercise. The FRP measured by SEVIRI was adjusted using the WLS coefficients for each region to provide the predicted FRP potentially measured by MODIS. The nearly 1:1 relationships between the predicted and measured values of FRP demonstrate the unbiased nature of the WLS models at 5.0 ° grid cell resolution and hourly temporal resolution for northern Africa, southern Africa, and South America. Results of the validation exercise are summarized in Table 5.1.

The linear relationships between SEVIRI and MODIS found here at 5.0° spatial resolution complement the linear models developed by Roberts and Wooster (2008) at 2.5° grid cell resolution. The regression coefficients derived here, however, take into account the effect of atmospheric transmittance, and also more appropriately represent the near-nadir response of MODIS. Nevertheless, the WLS models assume that SEVIRI-derived estimates of FRP were directly proportional to MODIS-derived estimates. Such a simple linear regression only captures the macroscopic features of the sensor-to-sensor relationships and does not account for any temporal variability

 	Land SAF VR-FRP	Doc: SAF/LAND/IM/VR_FRP/V_09 Issue: Version V/2009 Date: 18/10/2009
---	-----------------	---

that is induced by diurnal or seasonal fluctuations of fire activity (c.f., Figure 5.15). By deriving different regression coefficients for each of the four LSA SAF regions, however, the FRP Gridded algorithm does incorporate broad spatial differences in the sensor-to-sensor relationships that potentially arise from (i) differences in fire regimes, and (ii) differences in SEVIRI view angles.

To assess the predictive capability of the adjustment factors at a broader spatio-temporal scale, the 5.0° grid cells in the training and validation datasets were aggregated into weekly intervals. The FRP measured by SEVIRI was adjusted using the WLS coefficients for each region, and the adjusted FRP was summed within this time period to provide a prediction of the FRP that MODIS would have measured. Temporally aggregating fire pixels in this manner also imposes a spatial aggregation due to the ground track of MODIS. Thus the comparisons between the predicted FRP and the FRP actually measured by MODIS are representative of regional relationships.

Figure 5.21 illustrates that the FRP measured by SEVIRI at the weekly/regional scale is strongly related to the FRP measured by MODIS at the same spatio-temporal resolution. For each region, however, the predicted FRP consistently underestimated the true FRP that was actually measured by MODIS. This systematic underestimation is attributed to the following: (i) the overwhelming number of observations of low FRP fire pixels, (ii) the inherent underprediction of the mean FRP at observations of low fire activity, and (iii) the inherent inability to adjust an observation in which SEVIRI does not detect a fire pixel. These weekly/regional biases can in turn be applied in concert with the 5.0°/hourly WLS parameters to adjust the SEVIRI measurements of FRP and provide unbiased estimates of the FRP potential measured by MODIS at the regional and weekly scale.



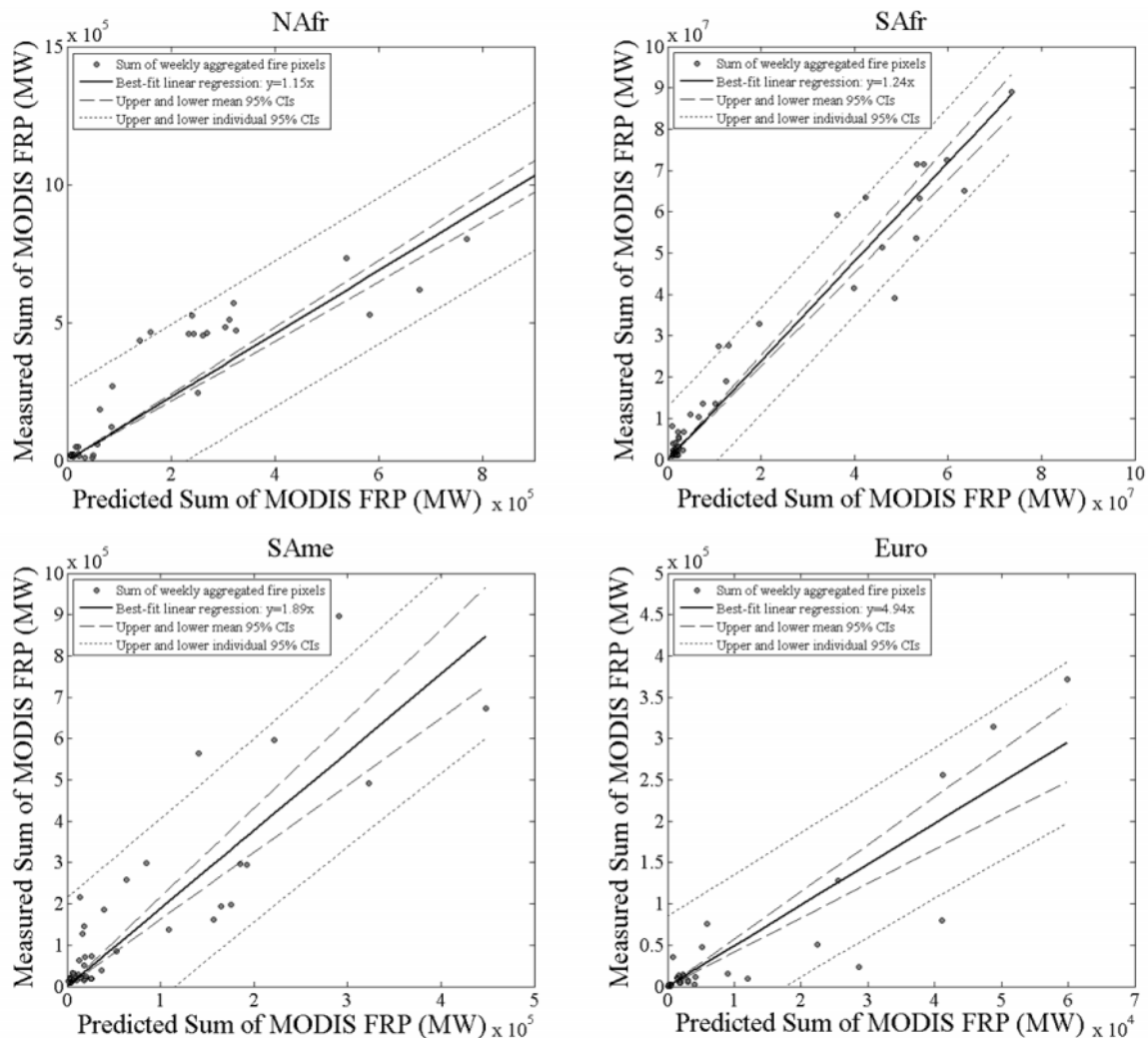


**Figure 5.21:** Performance of the WLS models at the weekly/regional scale. In all four LSA SAF regions the predicted sum of FRP underestimates the measured sum of FRP. The bias values shown in the legend (also shown in Table 5.1) can be used in conjunction with the WLS parameters to adjust the SEVIRI measurements of FRP and provide unbiased estimates of the FRP potential measured by MODIS at the regional and weekly scale.

### 5.2.3 Analysis of Ecosystem-Specific Biases

Figure 5.22 shows the land cover classification from the GLC 2000 data set and the fractions of fires detected in each land cover type for the MODIS MOD14 and SEVIRI data sets. There is generally good agreement between the two data sets with maximum differences of 4% attribution (maximum relative error of 25%). SEVIRI has a tendency to detect relatively more fires in mosaic forests and deciduous woodlands compared to MODIS, while MODIS detects more fires in scrublands and croplands. For the most part this can be explained by the different detection thresholds of the two instruments (a lower limit of 20-40 MW FRP for SEVIRI and 7-10 MW FRP for MODIS) and the sorts of fires dominating each particular landcover class. In



particular, cropland fires tend to be very small (i.e. have low FRP) and are thus more likely to be missed by SEVIRI data set than by MODIS.

With the present analysis it remains unclear to what extent the (small but significant) differences in the vegetation-type specific fire detection efficiency are related to the viewing geometry of the two instruments. This could in future be tested by analyzing fires in similar vegetation classes which occur in different regions on the African continent (for example cropland fires in the Sahel zone versus those in Northern Africa or South Africa).

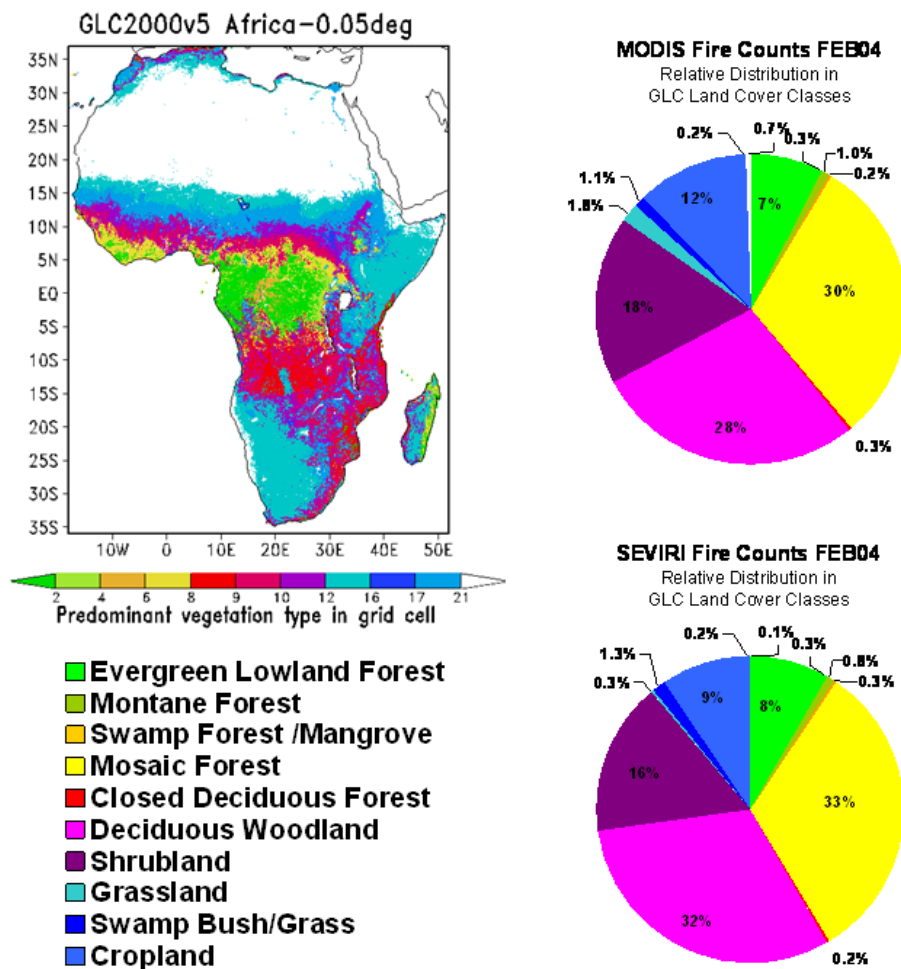


Figure 5.22: GLC 2000 land cover classification and relative frequency of fire detection in each land cover type for MODIS and SEVIRI data.

#### 5.2.4 Effects of Viewing Geometry

No specific analysis was performed to investigate the effects of the viewing geometry. However, various results reported in the other sub sections point to a decreasing detection efficiency and reduced FRP accuracy for pixels far away from the sub-satellite point.

### 5.2.5 Effects of Saturation

To quantify the extent of MIR channel sensor saturation, the KCL FRP product data of February, May and August 2004 were used. It was found that SEVIRI detected 1.3 million fire pixels in February 2004 across Africa, of which only 0.1% were saturated in the level 1.5 data. In May and August the numbers were 0.9 million (0.5% saturated) and 1.7 million (0.6% saturated) respectively, and thus saturation when taken over the entire dataset, is seen to be a relatively minor occurrence. However, on a per-fire basis saturation levels can be more than an order of magnitude greater, even potentially affecting 25% of the fire pixels recorded over very intense/large fires, and on a per-slot basis at the time of peak fire activity saturation typically affects a few percent of the detected fire pixels.

Figure 5.23 shows the results of the SEVIRI ‘special operations mode’ experiment with regard to instrument saturation. In this case the Meteosat-8 SEVIRI instrument was operated with an extended dynamic range and with a rapid 5-minute scan over southern Africa during September 2007, at the peak of the fire season in this region. The plots shows a comparison of total sub-scene FRP when the instrument is operated in low gain mode (essentially without any saturation of the MIR spectral channel) as compared to the same data with the saturation effect artificially induced. Results are not currently available for data collected around the midday period, but the plot indicates that saturation is a more prevalent phenomenon at the location of peak burning than is suggested by the continent-wide data above. Towards the diurnal peak, approaching 5% of detected fire pixels are saturated, resulting in an FRP underestimation of around 10%. At night this increases up to 8% and 40% respectively, though the total sub-scene FRP at night is low so the overall effect on the cumulative time-integrated FRP (i.e. the FRE) would be minimal and the lower levels of FRP percentage underestimation present during the day cause a far greater total effect. Analysis of the individual pixel brightness temperatures confirms that under this extended dynamic range operation (max MIR channel BT = 375 K) less than 0.002% of the total fire pixels detected over the day are saturated, and thus operating SEVIRI in such a mode would effectively negate any impact of pixel saturation on the FRP results.

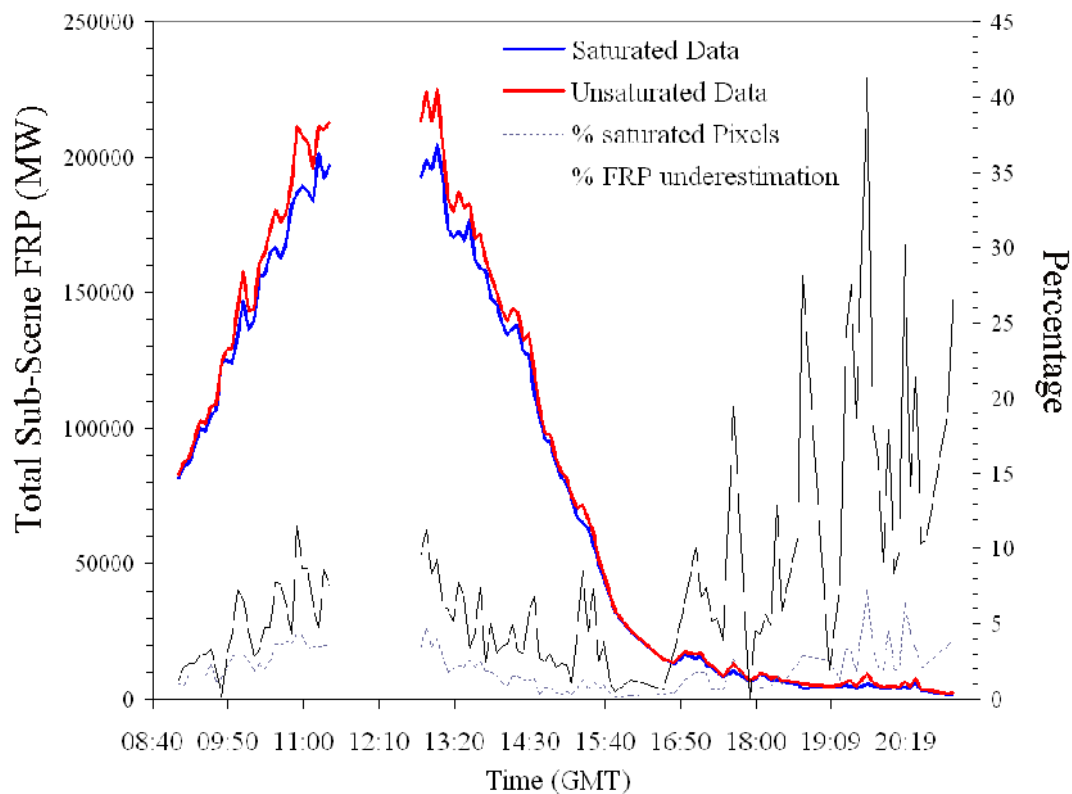


Figure 5.23. Data from the SEVIRI ‘special operations mode’ experiment conducted on 4 September 2007, when the Meteosat 8 SEVIRI instrument was put into low-gain mode. The figure compares the sub-scene cumulative FRP recorded in this ‘unsaturated’ mode to that which would have been recorded under normal conditions (i.e. with saturation present for pixels with a MIR BT of 335 K or greater), and the figure also show the % of pixels that would have been saturated, and the degree of FRP underestimation caused by this saturation, also expressed as a percentage.

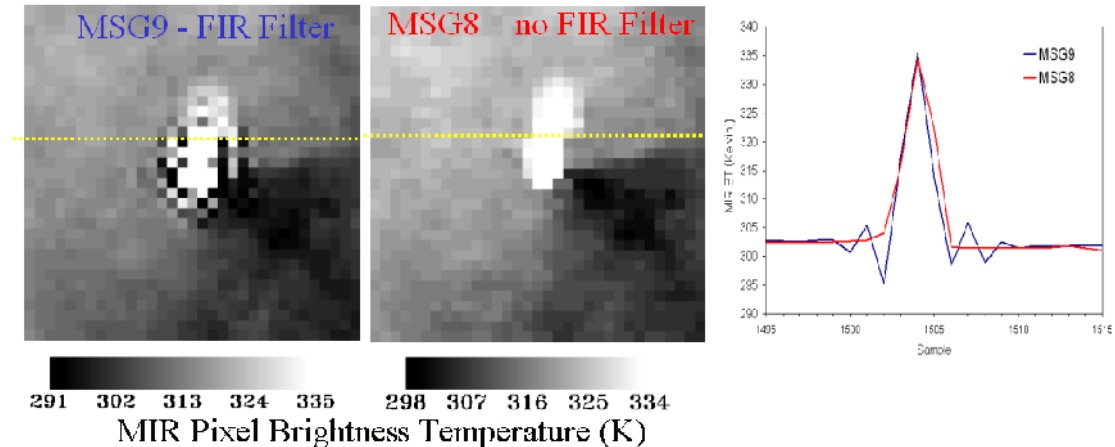
### 5.2.6 Effect of SEVIRI Image Processing Chain

Table 5.2 shows the impact of the level 1.0 to level 1.5 conversions on the number of saturated SEVIRI pixels. It is very clear that the smoothing employed in the spatial regridding of the level 1.0 data results in a much lower number of saturated pixels in the output level 1.5 data. As a consequence, under normal observation conditions there is likely to be more FRP underestimation present than is suggested by the number of saturated pixels present in the level 1.5 product.

Date and time	Level 1.0 3.9 BT saturation range (DN)	Level 1.5 Max 3.9 BT (Kelvin)	Level 1.0 Number of Saturated Pixels	Level 1.5 Number of Saturated Pixels
20040712081503	334.22 - 334.49 (1023)	335.56	8	4
20040712083003	334.21 - 334.49 (1023)	332.20	64	27
20040712084504	334.49 (1023)	335.56	1	1
20040712090004	334.21 - 334.49 (1023)	335.56	9	1

**Table 5.2:** Pixel saturation statistics for level 1.0 and level 1.5 versions of SEVIRI fire scenes.

Data from the SEVIRI ‘special operations mode’ experiment is shown in Figure 5.24 with regard to the on-board application of the FIR filter. In this case the FIR filter was not applied to the Meteosat-8 data, and the improved fidelity of the observations of this fire can be clearly seen when compared to the contemporaneously recorded Meteosat-9 data upon which the FIR filter was used.



**Figure 5.24.** Data from the SEVIRI ‘special operations mode’ experiment conducted on 4 September 2007, when the FIR filter was removed from the Meteosat 8 SEVIRI instrument but kept on the Meteosat 9 SEVIRI instrument that observed the same area almost simultaneously. The figure shows the MIR brightness temperatures recorded over the same fire by both systems, and the transect illustrates the effect of the FIR filter negative side lobes.

The impact of this FIR filter on the retrieved FRP observations was assessed primarily through simulations, calculated using the steps shown in Figure 5.25. An example output from the simulation of the SEVIRI observation process, which included representations of both the SEVIRI point spread function (PSF) and finite impulse

response (FIR) filter and a set fire size and temperature, is shown in Figure 5.26. A real SEVIRI active fire observation with the FIR filter employed is shown for comparison. The similarity of these two representations is apparent, particularly in terms of the increased radiance at the fire pixels themselves and the depressed radiances at the surrounding pixels due to convolution with the FIR response filter and its negative side lobes. The primary difference in the two representations is that in the model a spatially ‘flat’ background (i.e. constant brightness temperatures) are used, whereas the background in the true SEVIRI data has some variability due to ambient surface temperature variations. These depressed radiances can induce a higher brightness temperature variability in the ambient background window around fire pixels, and thus can impact the likelihood of the fire pixels actually being detected (since the algorithm scales certain of the detection criteria by a measure of the variability of signals found with the surrounding background window).

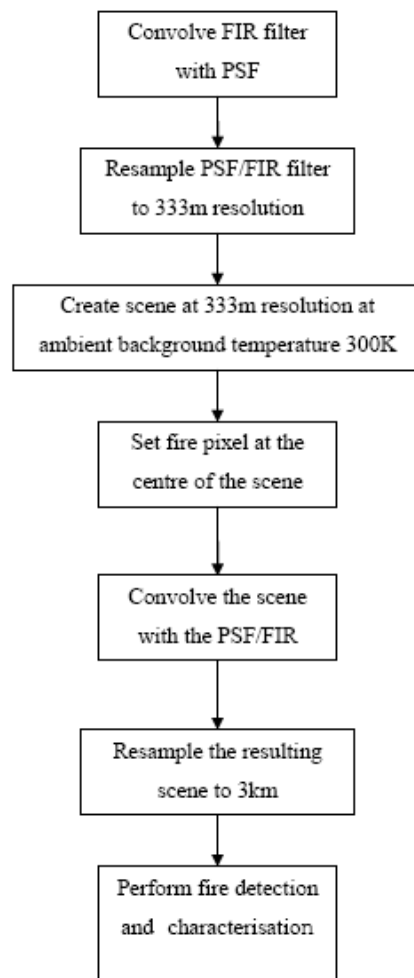
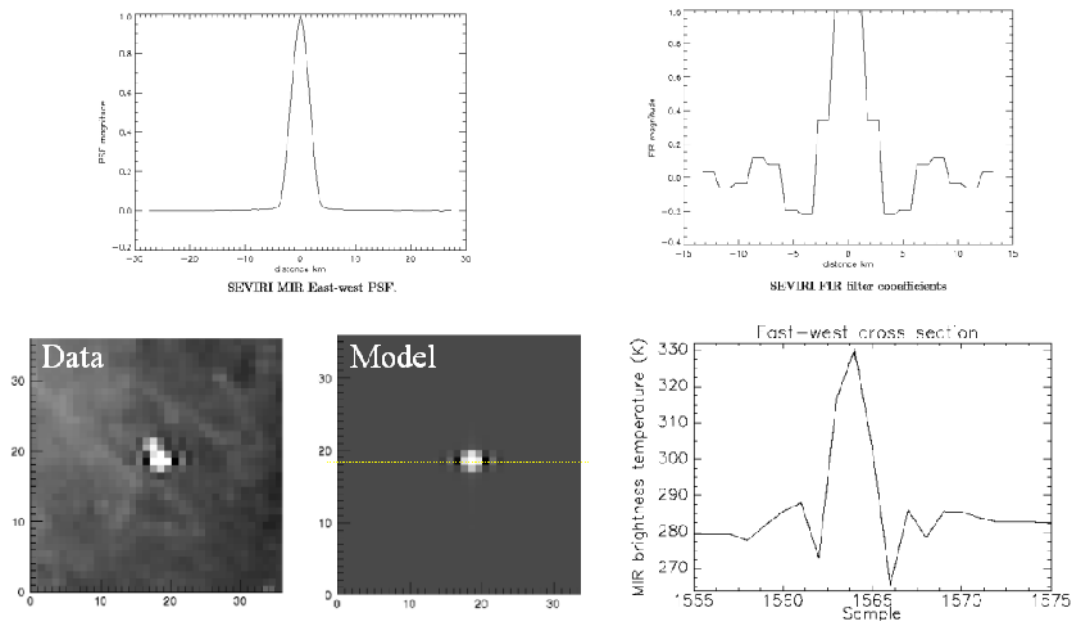


Figure 5.25. The major steps involved in simulating SEVIRI active fire observations using a spatially invariant background temperature of 300 K.



**Figure 5.26:** The SEVIRI point spread function (E-W) and the finite impulse response filter, together with a SEVIRI observation of an active fire modelled with these as compared to a real SEVIRI active fire observation. The effect of the negative side lobes (resulting in depressed radiances either side of the fire) induced by the FIR filter can be seen in both, and their impact is shown quantitatively by the east-west transect.

The effect of the SEVIRI observation process on the quantification of FRP was assessed using simulated SEVIRI active fire data of the sort shown Figure 5.26, calculated for differing fire size and temperature distributions (and so different FRP values). The SEVIRI PSF acts to smooth the fire radiance out over neighbouring pixels and can result in fire pixels at the edges of the fire actually contain some of the fire energy output, but with signals that do not allow them to be detected as fire pixels. This will cause underestimation of FRP compared to the raw FRP error (induced by the Planck function approximation), and the magnitude of this is shown in the “FRP without FIR” error value in Figure 5.27. In some cases its magnitude actually cancels out the effect of the Planck function approximation. The additional application of the FIR filter, expressed by the “FRP level 1 error” makes the most significant difference to the degree of error in the case where the fire forms the largest proportion of the pixel (1%), but in fact all such fires would have in reality resulted in a saturated SEVIRI pixel in any case, so the effect would have been outweighed in magnitude by the saturation impact. For non-saturated fires covering 0.1% and 0.01% of the SEVIRI pixel field of view (FOV), application of the FIR filter has less of an effect. It acts in two ways, with the positive side lobes directly giving rise to additional fire pixels and the negative side lobes having an adverse affect on the background characterisation involved in the fire detection algorithm (and thus potential leading to FRP overestimation via depression of the background temperature

estimate). The lowest FRP fires shown here are those where the fire size is 0.01% of the SEVIRI FOV (rightmost plot), and for fires of this size only those with a fire-effective temperature of  $\sim 800$  K or higher would in fact be detectable under real conditions (i.e. with a varying ambient background temperature). Nevertheless, the Figure indicates that such low FRP but still potentially detectable fires may in theory have their FRP underestimated by up to 60% under the conditions examined here, due primarily to the effect of the sensor PSF smoothing the fire radiance out over a number of pixels, and to some of these pixels failing to be detected as fire pixels. At such low signals, the effect of the FIR filter is negligible, and thus the FRP underestimate is equal with and without the FIR filter.

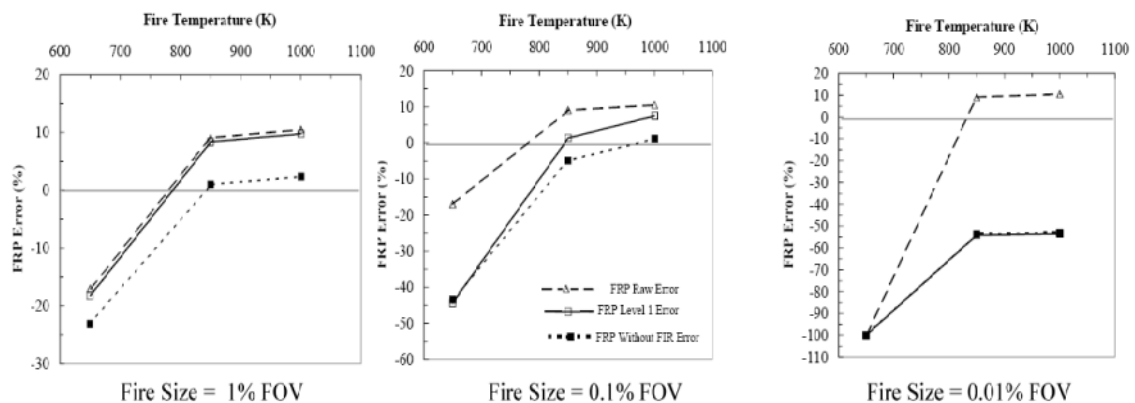


**Figure 5.27:** The effect of the SEVIRI observation process on the retrieval of FRP for fires of different effective temperatures and pixel proportions. The errors in FRP is shown due to the fourth order approximation to the Planck function only, to the complete modelled level 1 observations process (PSF and FIR filter) and to the observations without the FIR filter.

In order to determine the effect when the ambient background temperature is allowed to vary in a realistic way, BIRD data were used to provide the MIR background radiances for the simulations, upon which the modelled fire spectral signals were superimposed. The resulting array subject to the same SEVIRI observation process as described above. Figure 5.28 shows the resulting simulated SEVIRI MIR and TIR channel data, whilst Figure 5.29 shows the degree of error for the range of fire FRP's that are detectable from SEVIRI. The use of the varying background temperature has increased the background variability measure, thus increasing certain of the fire pixel detection algorithm thresholds that are scaled by this parameter, consequently making any low signal fire pixels less likely to be detected. This has resulted in a decreased total FRP measure, since more of the true fire pixels caused by spreading out of the fires radiance into surrounding pixels due to the PSF and FIR filter convolutions remain undetected. For low FRP fires, this results in a greater level of FRP underestimation when the varying background is used, as compared to the flat (spatially invariant) background.



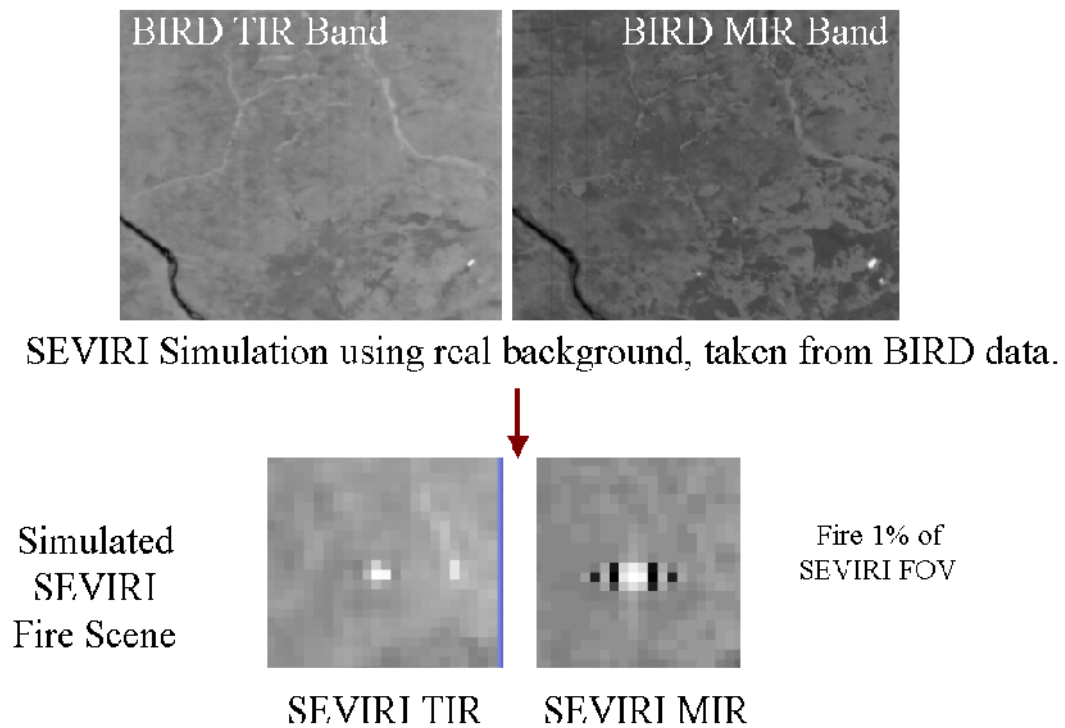


**Figure 5.28:** Simulated SEVIRI active fire TIR and MIR channel data, derived from higher spatial BIRD imagery to provide the ambient background measurements, and with a modelled fire spectral radiance signal superimposed.

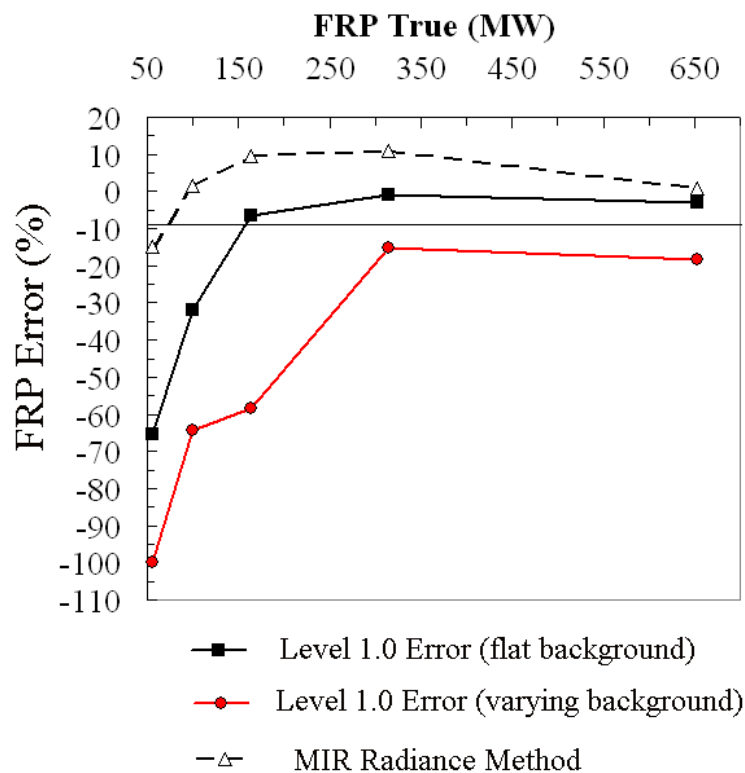


**Figure 5.29:** Degree of underestimation induced by the SEVIRI observation process on simulated fires of the sort depicted in Figure 5.28 and which have been modelled with a varying ambient background temperature (taken from BIRD imagery) and a spatially invariant ‘flat’ background temperature. The error due only to the MIR radiance method alone is also shown.

Finally, Figure 5.30 shows the results of the SEVIRI ‘special operations mode’ experiment with regard to data collected simultaneously by Meteosat-8 and Meteosat-9, firstly when the former system had the FIR filter present and then when it was removed. Under standard operations, Meteosat-8 measures per-scene FRPs on average around 10% lower than those recorded by Meteosat-9. On removal of the FIR filter, this difference is increased to around 22%, due to a combination of the removal of the influence of the –ve side lobes, the fact that some fire pixels remain undetected in the non-FIR filtered data since they have lower MIR radiances (see Figure 5.26) and to the effect of the removal of the FIR filter on the extent on signal saturation.

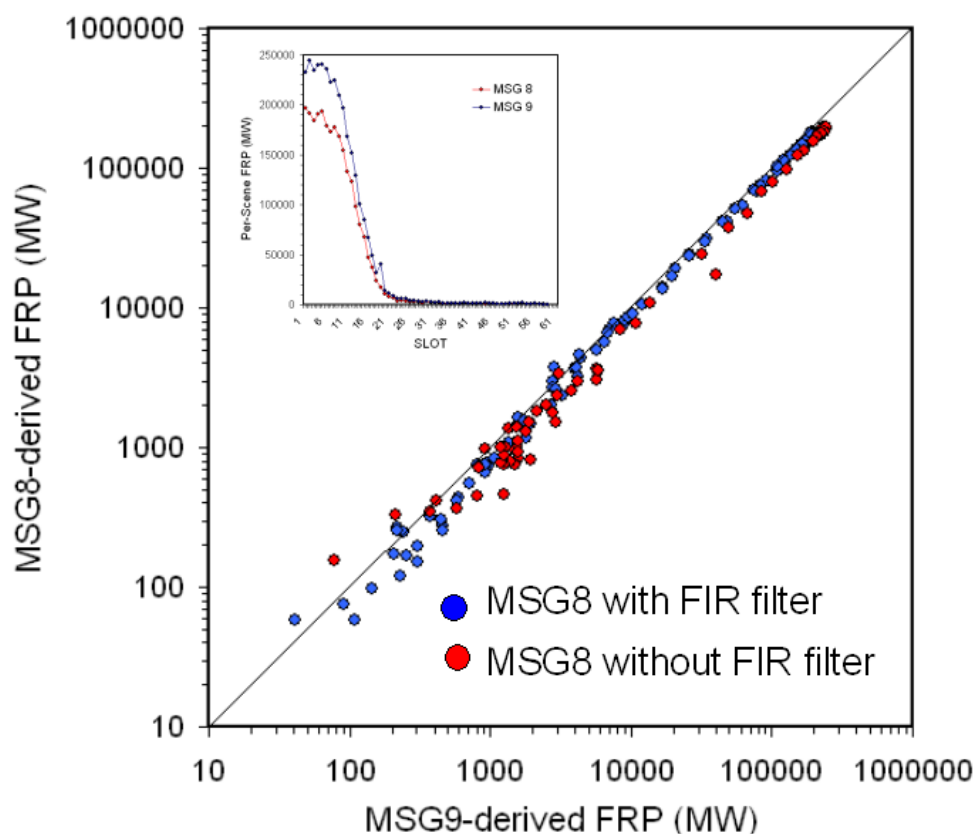


**Figure 5.30.** Comparison of Meteosat-8 and Meteosat-9 per-scene FRP data recorded simultaneously over southern Africa during the Meteosat-8 ‘special operations mode’ experiment. Greater discrepancies are seen when the FIR filter is removed from the Meteosat-8 SEVIRI (Meteosat-9 had the filter always applied).

## 5.3 Results of Land SAF Product Validations

### 5.3.1 Comparison to KCL Product

In terms of active fire pixel detection for each slot of data in August 2007, on average 12.7% of the fire pixels detected by the KCL FRP product in a slot did not have a corresponding Land SAF product fire pixel, whilst in 22.7% the reverse occurs. Whilst these figures may seem high, these averages are hugely influenced by night-time observations when there are very few fire pixels. During daytime conditions, where fire pixel counts and total FRP are typically orders of magnitude greater than at night and where the non-detection or false-detection of individual fire pixels is thus far less significant, the KCL and Land SAF products agree within 0.2% and 0.3%. Therefore in general the products show very similar performance characteristics in terms of fire pixel detections at the times when there are significant numbers of fires.

Figure 5.31 shows that when both the Land SAF and KCL products detect the same fire pixels, their FRP is retrieved almost identically, with a very slight positive bias in the Land SAF product most likely due to the specific calibration methods used in each

data processing chain. The level of difference is found to be similar when summing all FRP observed in each product over the complete Land SAF southern African region (the OLS line of best fit is  $y = 1.006x + 1336$ ,  $r^2 = 0.99$ ), and thus the Land SAF products for this region are essentially expected to have the same bulk error characteristics and accuracies as the original KCL product.

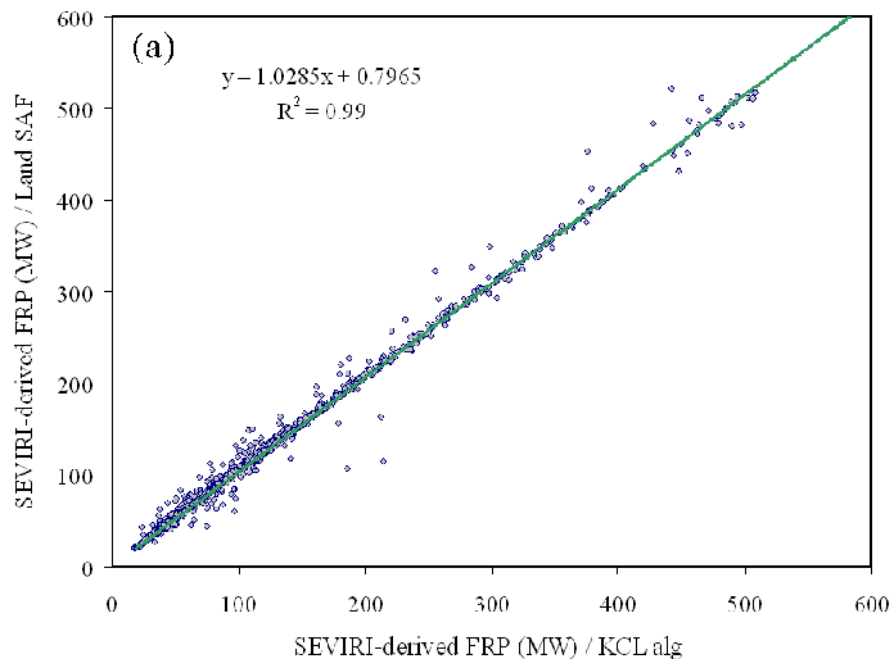


**Figure 5.31:** FRP comparison between the Land SAF FRP product and that generated at KCL from EUMETCAST-received SEVIRI data of the same imaging slots. The figure shows the per-pixel comparison for the Land SAF southern African region, where only data from fire pixels identified in both products are included in the match up dataset.

### 5.3.2 Comparison to MODIS

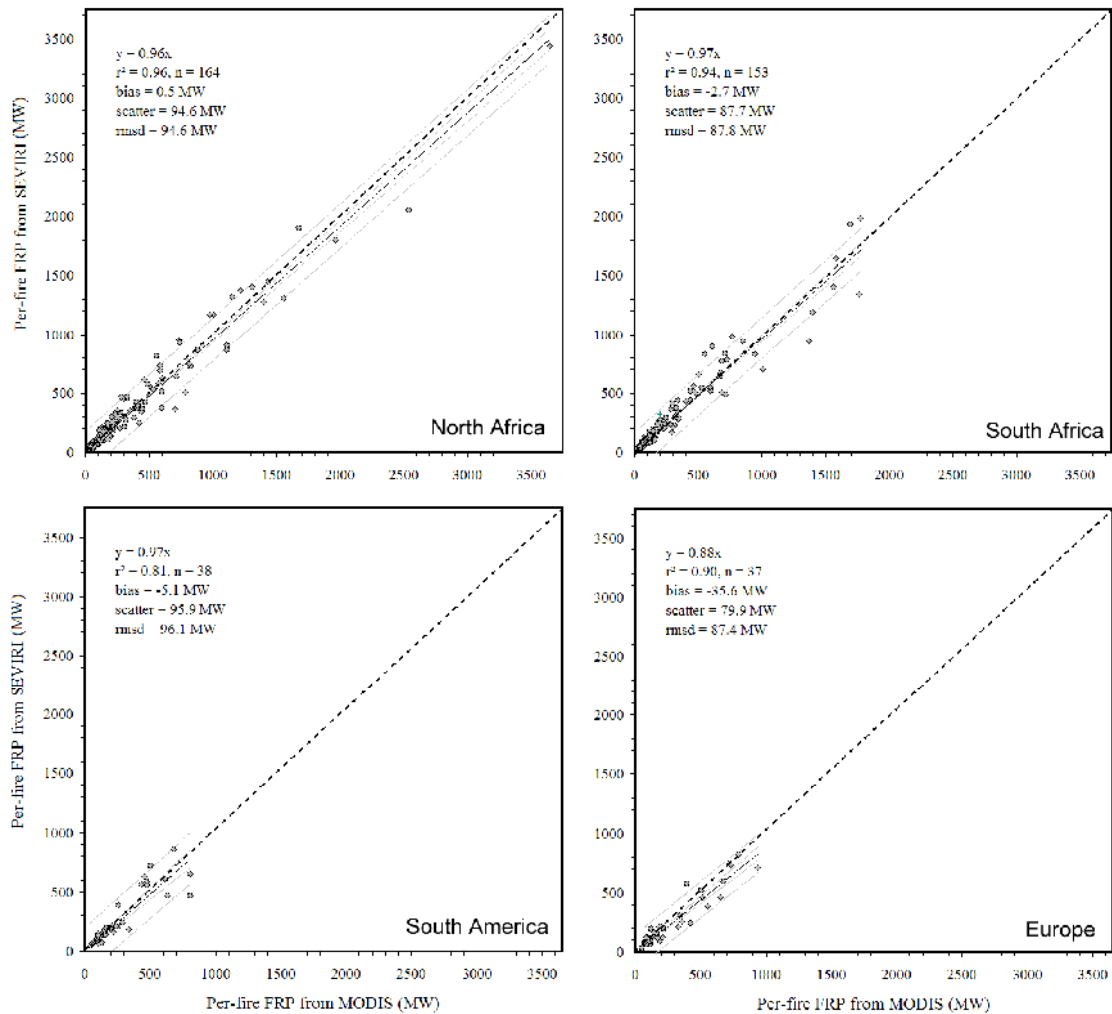
The comparison to MODIS was made using the most recent version of the FRP algorithm and data from the currently operational Meteosat-9 satellite. Both datasets had atmospheric corrections applied. In 1-7 December 2008 over North Africa, errors of omission in terms fire detection were 62%, i.e. 62% of MODIS-detected fire pixels had no corresponding SEVIRI fire pixel within the Land SAF product (compared to 54% in the KCL product for August 2004, see Section 0). Again it should be remembered that a large number of these MODIS pixels would have been in clusters, such that many ‘missing’ MODIS fire pixels might have corresponded to only one ‘extra’ SEVIRI pixel. Errors of commission analysis showed that 8% of the Land SAF products fire pixels had no matching MODIS pixel (compared to 6-8% in the KCL product). Errors of omission and commission for the other LSA SAF areas are shown in Table 5.2 (Columns 1 and 2).

On a per-fire basis, there is a strong correlation between the FRP measures made by SEVIRI in this region and by MODIS (Figure 5.32; top left), and over half (53%) of the SEVIRI-to-MODIS matchups have a difference of less than 20%. This is good performance, and in agreement with the results of the SEVIRI to MODIS per-fire FRP comparison made with the original KCL product (Figure 5.13). Results for this and other regions are shown in Table 1(column 4) and Figure 5.31.

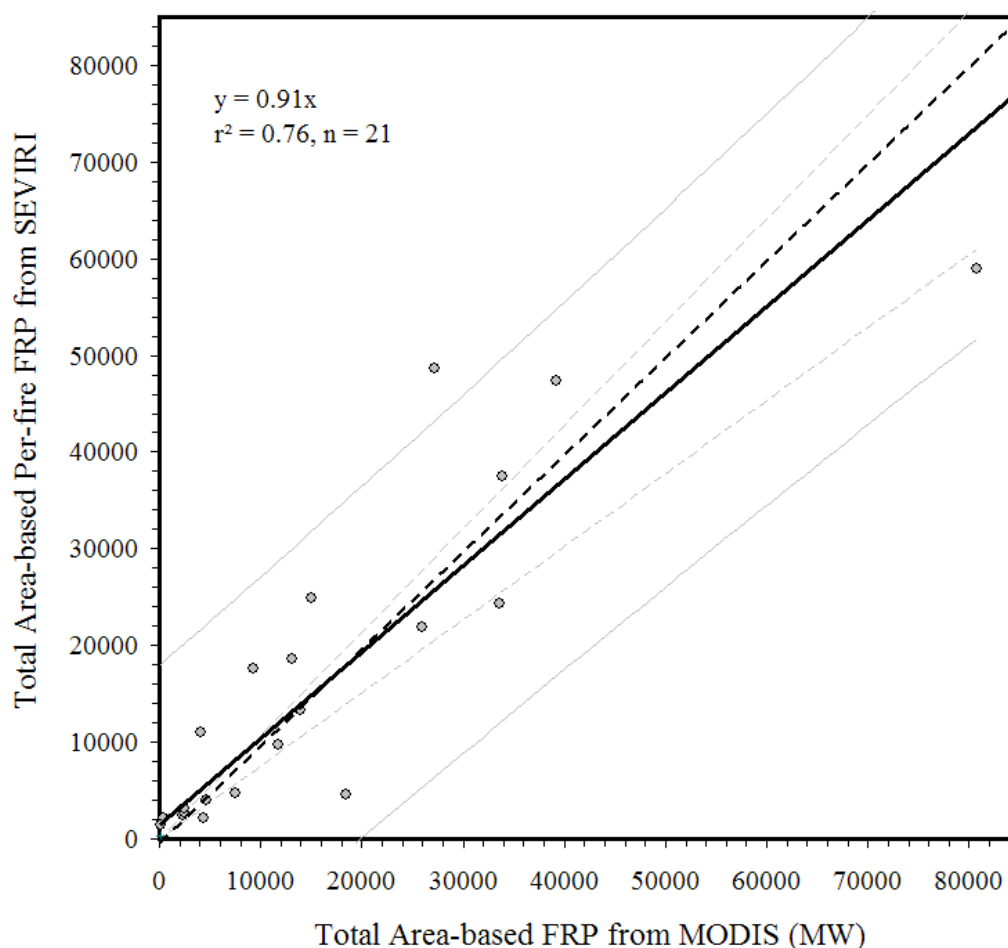
On a per-area basis the LSA SAF algorithm for SEVIRI typically detects a lower total FRP than MODIS detects when observing the same area almost simultaneously, this underestimate being a result of the aforementioned inability of SEVIRI to detect the lowest FRP fire pixels. Figure 5.33 shows the relationship between SEVIRI- and MODIS-detected cumulative FRP on a per-MODIS scene basis for North Africa, and the strong linear correlation found here attests to the similarity of the Land SAF product and the KCL FRP product whose swath-based relationship to MODIS was shown previously in this report. Results for this and other regions are shown in Table 5.3 (column 5).

	Image Dates (2008)	Fire Detection Error of Omission (%)	Fire Detection Error of Commission (%)	Slope of linear best fit relationship between SEVIRI-to-MODIS per-fire-based FRP measures	Slope of linear best fit relationship between SEVIRI-to-MODIS Area-based FRP measures
North Africa	1-8 Dec	62%	8%	0.96	0.91
South Africa	19-24 Aug	71%	6%	0.97	0.80
South America	14-24 Aug	85%	9%	0.97	0.30
Europe	9-17 Aug	95%	1%	0.88	0.13

**Table 5.3.** Performance characteristics of the LSA SAF FRP Product in the four geographical regions, compared to the MODIS Fire Product.



**Figure 5.32:** A comparison of per-fire FRP derived from SEVIRI and MODIS observations of fires observed near-simultaneously by each sensor for a one week duration in each LSA SAF region. Fires are designated as contiguous clusters of active fire pixels and SEVIRI FRP measured were taken from the Land SAF FRP per-pixel product in each case. MODIS fire locations were taken from the MOD14 product. The most radiant fires were detected in north Africa (top left), and all areas are displayed on the same x- and y-axis scales for ease of comparison.



**Figure 5.33:** Relationship between regional-scale inter-scene FRP derived from all spatially matched, contemporaneous SEVIRI and MODIS observations for the North African region 1-7 December 2009, where the MODIS swath is taken as the observation area and the Land SAF per-pixel FRP product was used as the SEVIRI record. The OLS linear best-fit passing through the origin is shown (bold line), along with the 95% confidence intervals on the mean (lite dotted line) and on the prediction of y from x (outermost lines). The 1:1 line is also shown (dashed). This LSA SAF region is closest to the sub-satellite point, and this the spatial resolution of the SEVIRI observations is highest. SEVIRI tends to generally somewhat underestimate regional-scale FRP, primarily due to the non-detection of the lowest FRP fire pixels, many of which MODIS can detect, though the degree of underestimation is relatively small as described by the slope of the linear best fit to the data. Some instances of overestimation also occur.

Whilst the slope of the area-based SEVIRI and MODIS FRP totals is 0.91 in North Africa (Figure 5.33), this slope lowers as you progressively move away from the sub-satellite point in the other LSA SAF regions (Table 5.3, Column 5). Results for Europe appear worse in comparison to the other regions, both on a per-fire basis but also in particular on a per-area basis – and this is largely explained by the fact that the majority of the fires during the study period were located in Eastern Europe, above a view zenith angle of 60 ° N (Figure 5.34) where the performance from geostationary orbit is somewhat compromised. The limited number of fires occurring in the Mediterranean since the operational use of Meteosat-9 limits our ability to compare only fires occurring further south in Europe. The



useful performance of the product in the Mediterranean region is, however, indicated by the impact study of the August 2007 Greek fires (Section 5.4).

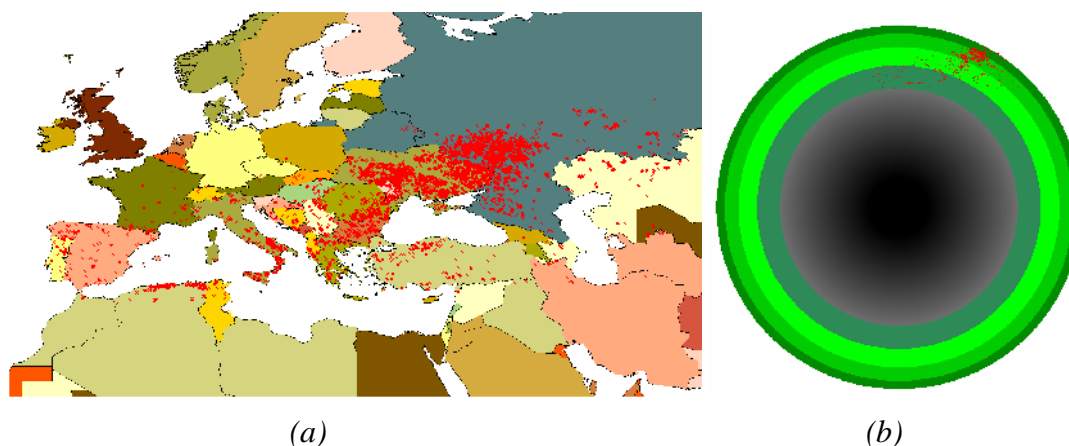




**Figure 5.34:** Location of all SEVIRI fire detections in Europe between 9 and 17 August 2008 – coloured red in this rendition and derived from the LSA SAF FRP Product. (a) shows the fire locations, whilst are mostly in Eastern Europe, whilst (b) indicates that such fires are mostly located at a view angle  $> 60^\circ\text{N}$  (outermost two concentric circles). This extreme view angle explains the relatively worse performance of the SEVIRI fire detection scheme in the LSA SAF region (Table 5.3).

## 5.4 Results of Validation Based on the Impact Studies

Global atmospheric monitoring systems like the one developed in the GEMS project (Hollingsworth *et al.* 2008) for the forthcoming GMES Atmospheric Service (GAS) envisaged by the European Commission and ESA require information on the wildfire emissions of several species as input. Because of the high temporal variability of fire activity the emission input has to be generated from fire observations. None of the currently available fire emission products satisfies all requirements of the monitoring system, in terms of accuracy, spatial and temporal coverage and resolution, timeliness, and operational availability (Kaiser *et al.*, 2006). The SEVIRI FRP product promises to improve the available fire emission input in several aspects:

1. improved temporal resolution, compared to products based on low Earth-orbit (LEO) observations;
2. improved accuracy, compared to hot spot products;
3. operational availability with sufficient timeliness for real-time forecasting.

The impact of the first aspect has been studied using the GEMS CO<sub>2</sub> monitoring system (see section 0) and it was a key aspect of a high-resolution study of impacts from Greek forest fires in the summer of 2007. The impact of the, theoretically, improved accuracy of the emission estimates is tested in a study by FMI, which compares the impact of using the MODIS thermal anomaly (TA) or FRP product in

 	Land SAF VR-FRP	Doc: SAF/LAND/IM/VR_FRP/V_09 Issue: Version V/2009 Date: 18/10/2009
---	-----------------	---

the FMI Fire Assimilation System and the HIRLAM regional air quality forecasts. The overall quality of the SEVIRI FRP product is also tested by comparison to the community-standard monthly fire emission inventory GFEDv2. An end-to-end case study of aerosol plumes emanating from forest fires in Greece in August 2007 demonstrates the capabilities of the real-time monitoring based on the GEMS system and SEVIRI FRP.

#### 5.4.1. Impacts of Temporal Resolution-Study of Sensitivity to Temporal Resolution of Emissions: Global Carbon Dioxide Modelling of 2004

Examples of the simulated CO<sub>2</sub> fields on 6 February 2004 are shown in Figure 5.35. They are expressed in total column (TC) CO<sub>2</sub>, defined as the pressure-weighted vertical average mixing ratio [ppm]. The top plot shows the CO<sub>2</sub> field for the simulation without fire emissions and the bottom one shows the field resulting from 1-hourly emissions. Both fields exhibit the typical inter-hemispheric gradient observed in winter. The contribution of the fire emissions is evident as an enhancement over central Africa.

The contribution of the fire CO<sub>2</sub> emissions to the CO<sub>2</sub> field is shown directly in Figure 5.36. It is computed as the difference between modelled TC CO<sub>2</sub> with fire emissions at 1-hour (top) and 8-day (bottom) time resolution and a simulation without any fire emissions over Africa. Note, that the total emission within each 8-day period is the same. Since the 8-day time resolution is the current GEMS baseline input (from the GFEDv2 inventory), the differences between the 8-day and 1-hour fire simulations describe the error that the current system suffers due to the limited temporal resolution of the fire emission input. Conversely, it can be interpreted as the positive impact that usage of the SEVIRI FRP product will have on the CO<sub>2</sub> fields modelled with the GEMS system.

Neglecting the temporal variation of the fires during each 8-day period results in a visibly smoother fire contribution to the CO<sub>2</sub> field. Furthermore, the CO<sub>2</sub> “plume” is shifted southwards in the simulations using the 8-day fire product. This is consistent with relatively less fire activity during the first few days of the 8-day period starting on 2 February and more fire activity later on, combined with a general transport southwards, which is evident upon closer inspection of the simulations, but not explicitly shown in this report.

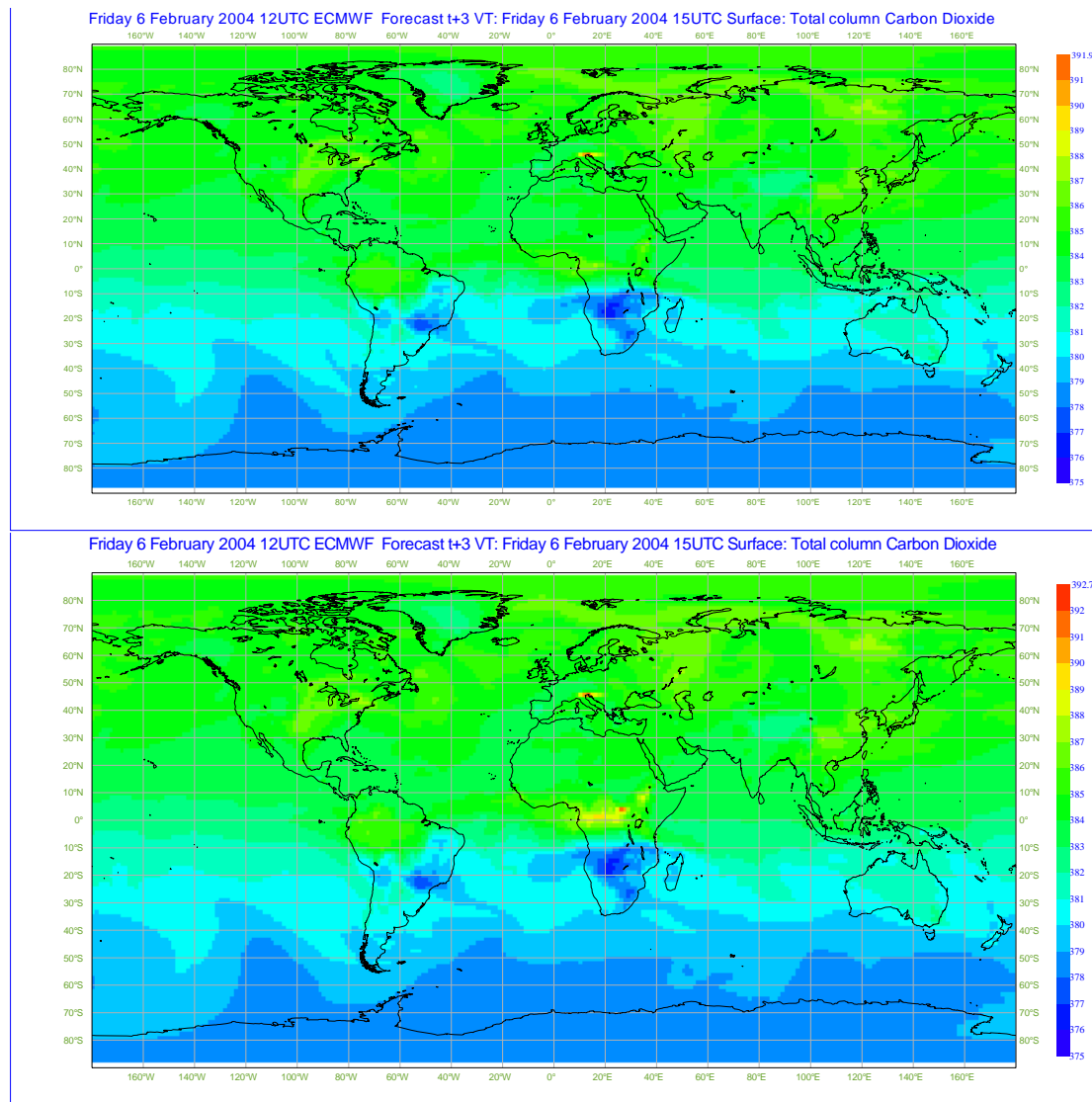


**Figure 5.35:** Total column CO<sub>2</sub> for simulation without (top) and with (bottom) fire emissions.

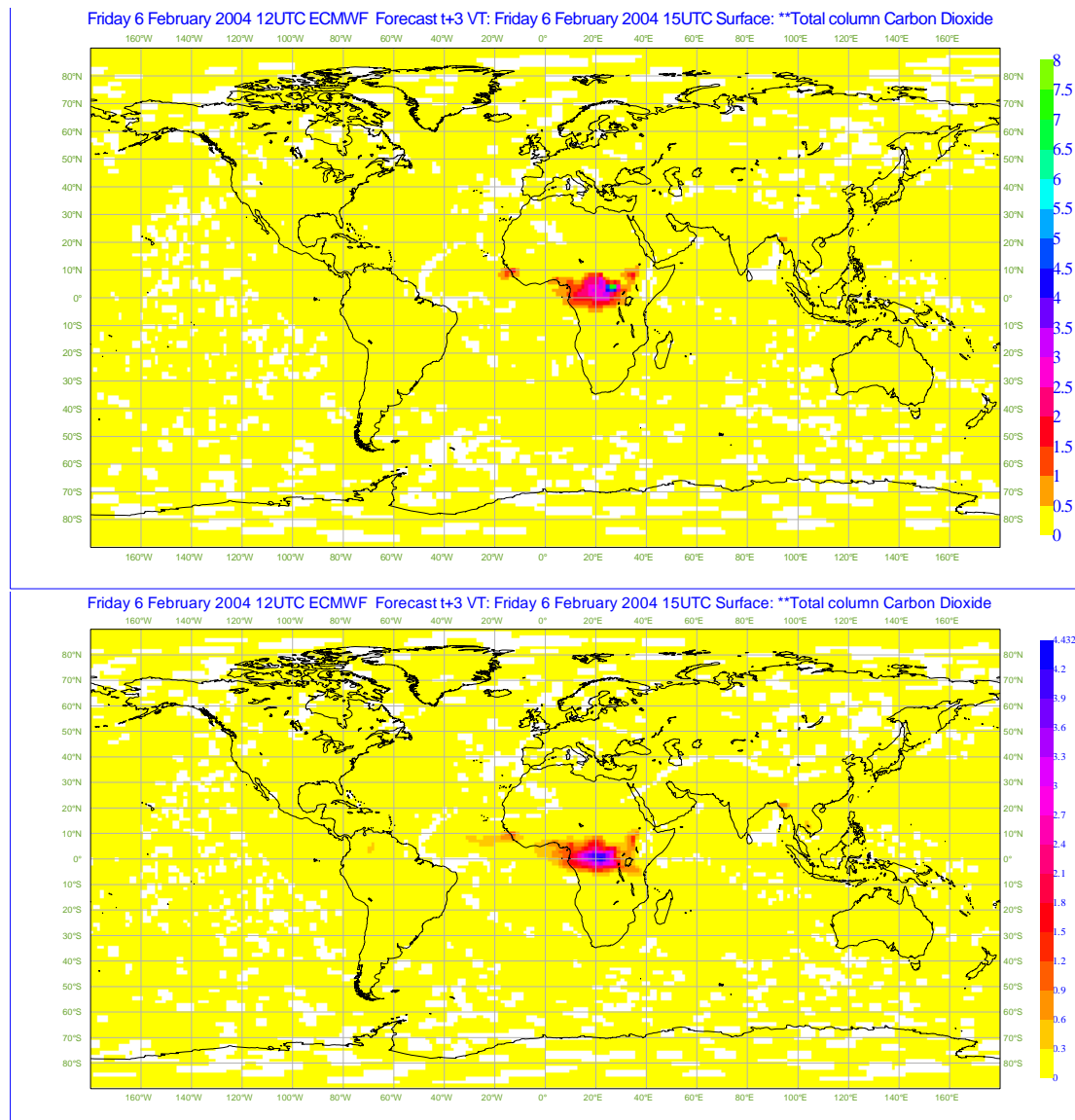


**Figure 5.36:** Fire emission contribution to total column  $CO_2$  for emission with 1-hour (top) and 8-days (bottom) emission time resolution.

The impact of providing  $CO_2$  fire emission input with the various time resolutions is shown in Figure 5.37. It is computed as difference between the fire emission contributions to the TC  $CO_2$  field in the three simulations with fire emissions. For example, the top plot shows the difference between the contributions in the simulation using 1-hourly emissions versus the one with 8-daily emissions. The top plot can be interpreted as the error in the  $CO_2$  field that is induced by neglecting the temporal evolution of the fire emissions during 8 day periods.

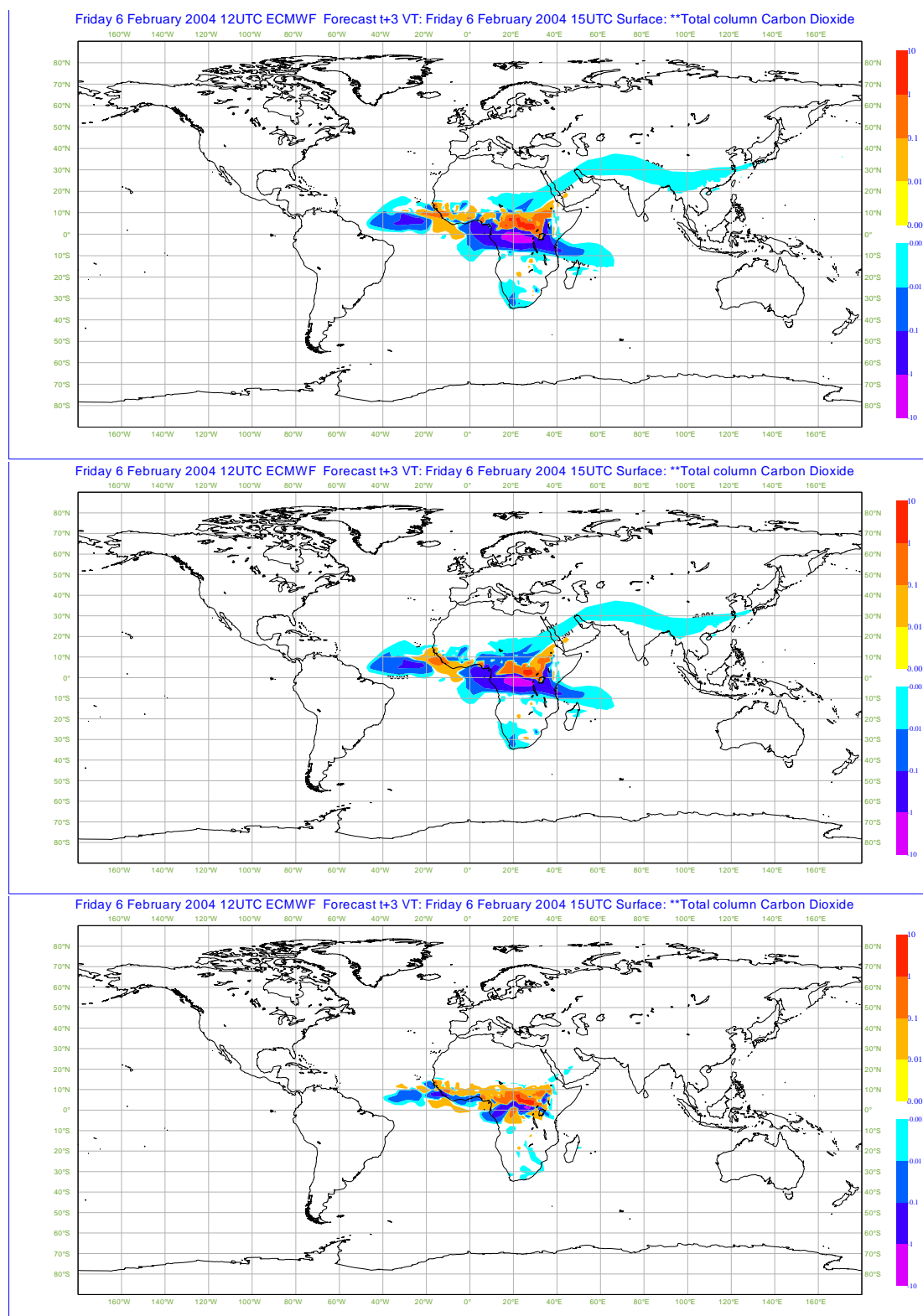


**Figure 5.37:** Differences in fire contribution to total column  $\text{CO}_2$  for emissions with different time resolutions: 1h - 8d (top), 1d - 8d (middle), 1h - 1d (bottom).

The middle and bottom plots of Figure 5.37 show the contributions of day-to-day variations and diurnal variations, respectively. They add up to the impact shown in the top plot. The strong North-South dipole over central Africa is caused by the shift in “plume” position mentioned above. It is evidently caused by the day-to-day variability of the fire activity. This also causes small effects that are propagated inter-continently within a few days (the response of less than 0.01 ppm TC CO<sub>2</sub> is however negligible in current CO<sub>2</sub> monitoring applications).

The diurnal variability of fire activity adds finer, more localised structure, as expected. The fine structure has almost the same amplitude as the broader structure induced by the day-to-day variability.

An example vertical cross section of the difference in the CO<sub>2</sub> mixing ratio due to neglecting all fire variability during 8-day windows is shown in Figure 5.38. The difference pattern has a complex structure that stretches across the whole troposphere, which is testament to the intimate link between emission and atmospheric transport variability. The impact is strongest in the boundary layer with values of up to more than  $\pm 4$  ppm.

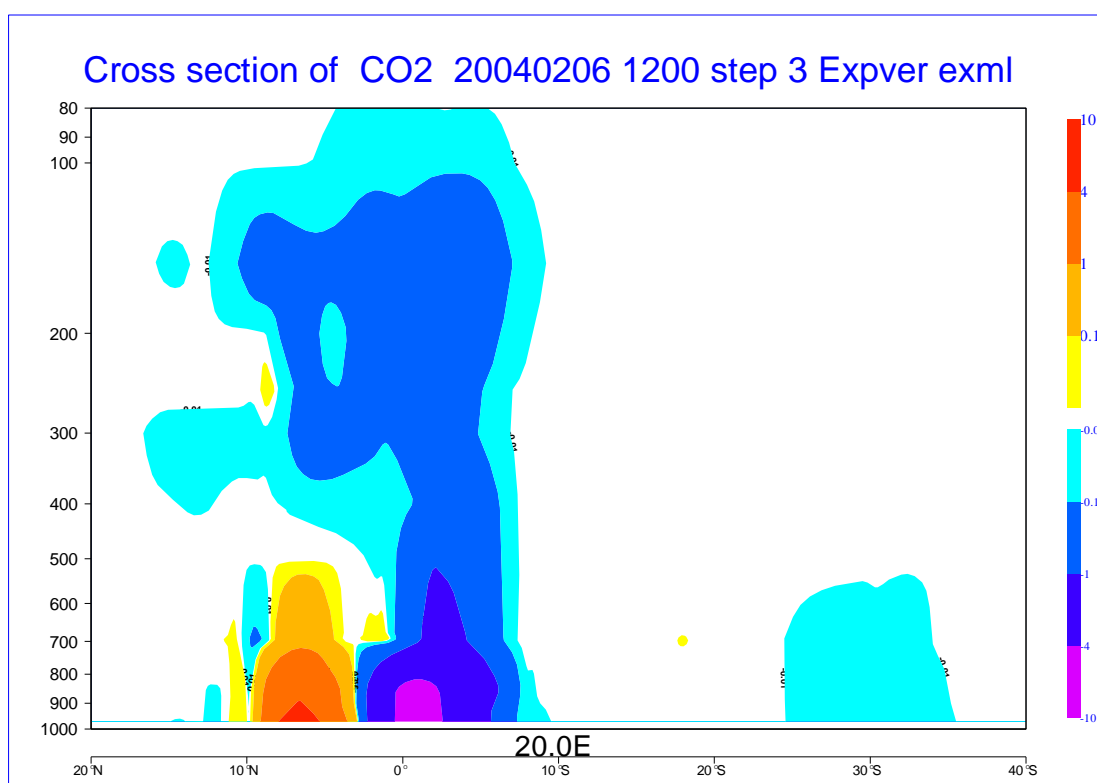


**Figure 5.38:** Vertical distribution of difference in fire contribution to the CO<sub>2</sub> mixing ratio for emissions with different time resolutions of 1-hour and 8-days.

The relative impact of 1-hour temporal resolution emissions as compared to 8-day ones is computed by normalising the observed differences by the contribution of (8-day) fire emissions to the CO<sub>2</sub> field. The result is shown in Figure 5.39. By neglecting

the temporal variability, errors between -90% and +70% can be incurred. The difference in the CO<sub>2</sub> fields is also propagated onto the Atlantic, far away from the burning regions. On a hemispheric scale the impact is diluted to about 1% of its typical regional value. Due to the tracer-like properties of CO<sub>2</sub>, these results are expected to be valid for all long-lived pollutants in the fire plumes (such as carbon monoxide, organic carbon, etc.).

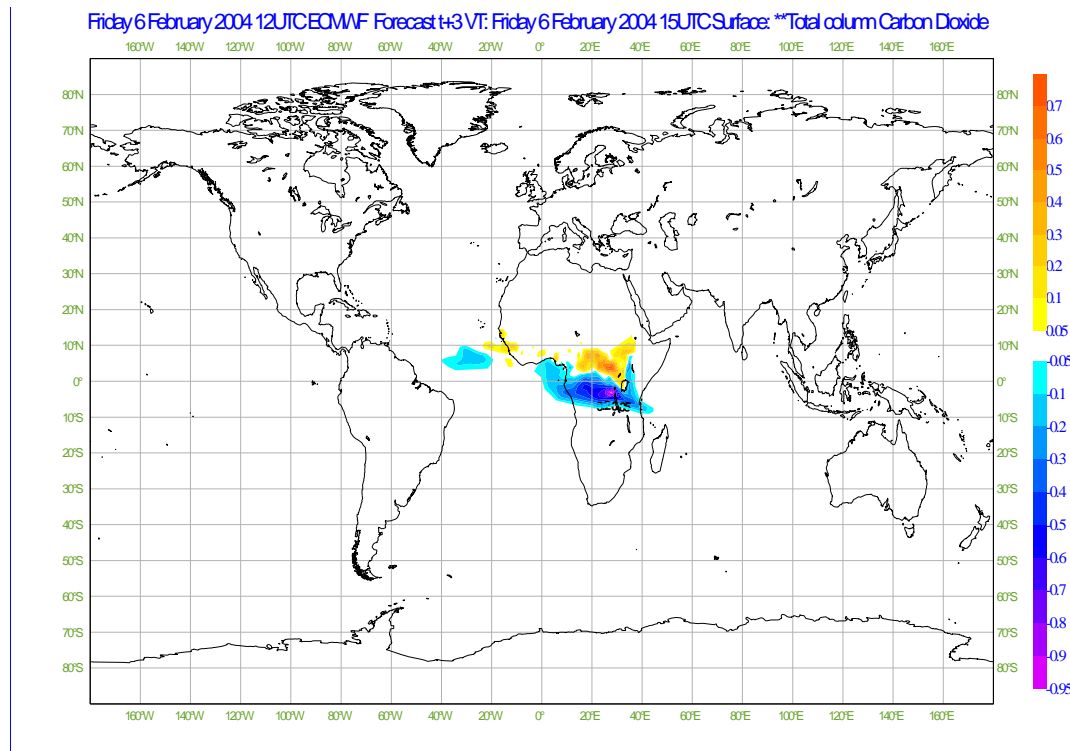


**Figure 5.39:** Relative difference of total column CO<sub>2</sub> for different time resolutions.  $(1\text{-hourly} - 8\text{-daily fires [ppm]}) / (1\text{-hourly} - \text{no fires} + 1 \text{ ppm})$ .

Analyses of simulated aerosol fields on 6 February 2004 and of the simulated CO<sub>2</sub> fields near the end of the simulation period have confirmed the general findings described above (not shown).

### 5.4.2 Impact on Estimating Fire Emissions

In this section, we show a) results of the comparison of SEVIRI-based monthly carbon emission estimates with data from the Global Fire Emissions Database (GFED version 2) and b) a qualitative comparison of the seasonal pattern of SEVIRI FRP with MOPITT CO profiles.

SEVIRI and GFED give similar results for Africa north and south of the equator, but SEVIRI tends to show slightly lower values overall (Figure 5.40). It is important to note that uncertainties are large in the GFED approach, so no quantitative assessment



can be made on the SEVIRI-based emissions performance. The most relevant difference seen between SEVIRI and GFED version 2 is the timing of the emissions peak in both hemispheres, which is diagnosed about one month later in GFED than in SEVIRI. The later timing of the peak appears more consistent with observations of atmospheric trace compounds (see next section), but until now the factors causing the difference between the peak fire occurrence and maximum loading of the atmosphere have not been determined satisfactorily. Preliminary data from GFED3 indicates that GFED2 emissions may have been too high in northern hemispheric Africa, leading to a closer match between SEVIRI and GFED estimates. In southern Africa, however, GFED3 estimates will be higher than GFED2 estimates, which were already higher than SEVIRI-based estimates. The difference is mostly resulting from emission estimates in woodland areas. In principle, the SEVIRI FRP product should be independent of vegetation type (see also section 5.2.3) so that differences in one particular ecosystem might hint to errors in the GFED system. This requires further proof, however. It is noteworthy, that due to large uncertainties in GFED based emissions, discrepancies between FRP and GFED do not necessarily point at shortcomings of the FRP method.

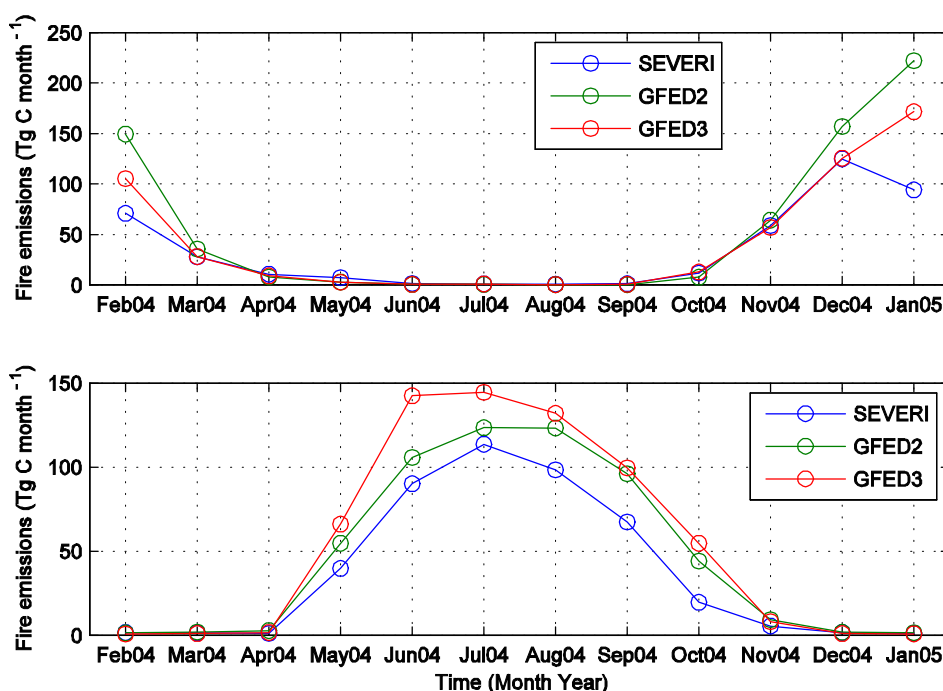


**Figure 5.40:** Comparison of monthly SEVIRI based carbon emissions with Global Fire Emissions Database (GFED) versions 2 and preliminary version 3 for Africa north of the equator (top panel) and Africa south of the equator (bottom panel).

Figure 5.41 shows the comparison of interannual variations in SEVIRI FRP with MOPITT CO profiles in the southern hemisphere. The peak CO loading derived from the MOPITT sensor occurs in September for retrievals between 700-1000 mb.

Retrievals higher in the atmosphere (250 and 350 mb) indicate that the peak atmospheric CO concentration occurs later (October), though this discrepancy may lie with sensitivity of the averaging kernels at different heights to other factors (e.g. surface temperature). The temporal trajectories of the MOPITT CO concentration and total cumulative monthly FRP (proportional to total fuel burned) in the southern hemisphere are offset from one another, with peak FRP-derived biomass burning total in July and peak CO concentrations in September/October. The shapes of the distribution are, however, extremely similar.

The temporal lag is removed when examining the mean per-pixel FRP, which should be approximately proportional to the mean rate of combustion per grid cell. This suggests that there may be additional information in this parameter, which, with further refinement, might enable better parameterisation of temporal evolution of emissions factors used to convert fuel consumption measures into emission of trace gases.

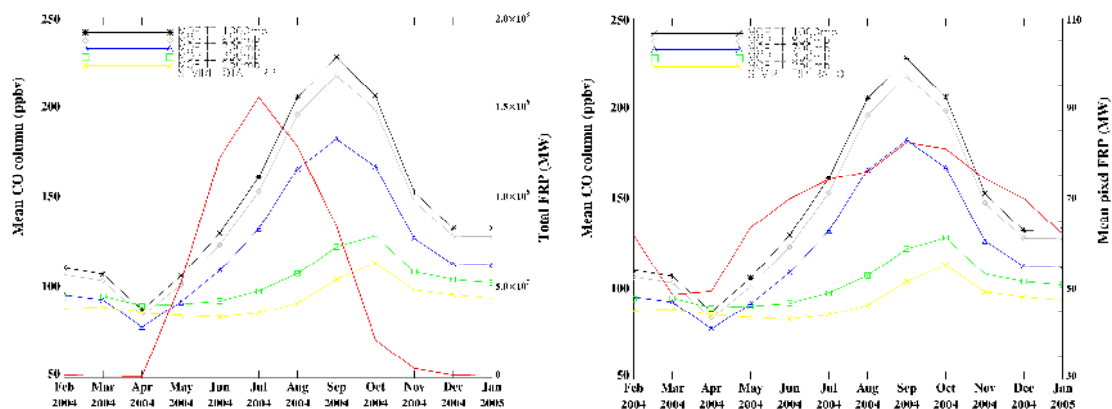


**Figure 5.41:** Annual variation of mean monthly MOPITT CO mixing ratios retrieved for five pressure levels over land between February 2004 and January 2005 in comparison to total FRP (left) and mean per-pixel FRP (right) for southern hemisphere Africa.

### 5.4.3 End-to-end Use Case Study: Modelling the Greece Fire Plumes of August 2007

This section shows the results of a case study initiated in the FREEVAL project on modelling the smoke plumes from fires occurring in the Mediterranean region in August 2007 using SEVIRI FRP derived fire aerosol emission estimates. It allows for some independent validation of the SEVIRI product and also served to identify the necessary technical processing steps and required product characteristics of the pixel and gridded SEVIRI FRP products. The study set-up is described in section 0.

Figure 5.42 shows the number of active fires detected over the Mediterranean region by MODIS and by SEVIRI on August 25, 2007, when fire activity was at a peak level.

Most fires occurred on the western half of the Greece Peloponnese island. While the MODIS and the SEVIRI products match very well in terms of spatial pattern of fire activity, the SEVIRI product detects much more active fires than the MODIS product. As a result, MODIS distinctively under-represents the spatial expansion of the main clusters of fire activity on Peloponnese island compared to SEVIRI.

MODIS Detected fires 25 Aug 2007    SEVIRI Detected fires 25 Aug 2007

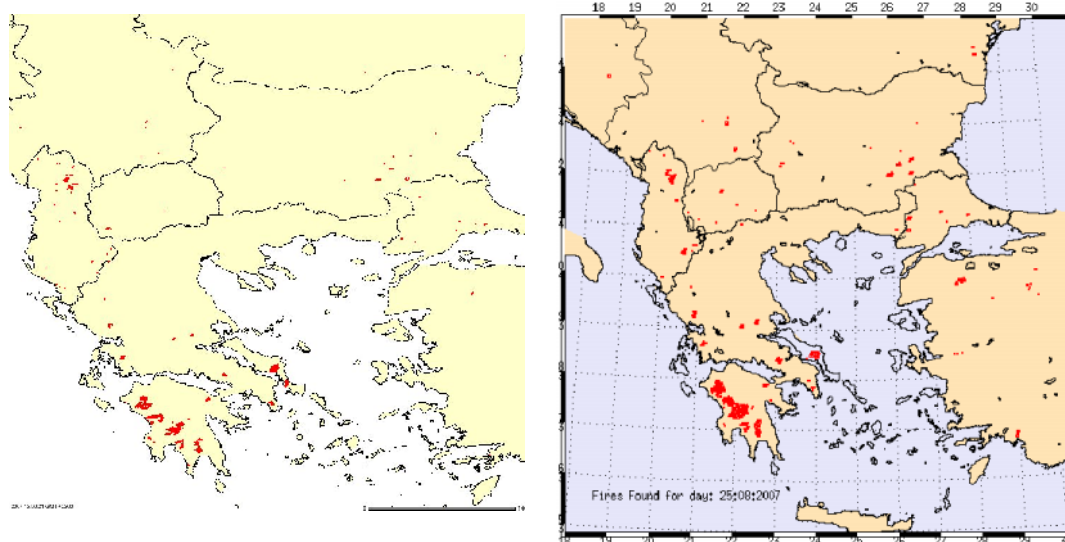


**Figure 5.42:** Number of active fires (hotspots) detected by MODIS (left) and by SEVIRI (right) on August 25, 2007 over the Mediterranean region.

Two snapshots of simulated optical depth of organic matter and black carbon aerosols, which dominate the smoke optical depth from fire plumes and have comparably smaller other emission sources, are plotted and compared to concurrent MODIS visual images in Figure 5.43. The plots also show the fire activity observed by SEVIRI and MODIS. The simulations qualitatively reproduce the key features of the observations, in particular the fact that the smoke plumes are separated into series of individual “puffs”, which originate from the high fire activity during daytime and are separated by the low activity at night. An animation of the modelled plumes shows that the ones near the Libyan coast have been emitted on the previous day and the one in Algeria is two days old. Furthermore, on August 25, the following observations can be made:

- a very strong plume just off the Peloponnese, associated with very high FRP values (exceeding 70,000 MW)
- a westward broadening of the plume over the Mediterranean
- smaller plumes off the coasts of Albania, Southern Italy, and Sicily
- a strong plume falling on land in Libya

And for the following day:

- a very strong plume falling on land in Libya on 26 Aug, associated with the very high FRP values observed on 25 Aug

- a distinct “mirrored S” shape of the plume
- a thin, weak plume originating in Albania

Despite the striking similarities, the locations of the plume features are often slightly shifted in the simulations with respect to the MODIS images. This may be related to the parameterisation of the smoke plume injection height (currently at the lowest model level) but needs further investigation.

The simulated optical depth of all the model aerosol species that are emitted by fire, i.e. organic matter, black carbon, and sulphate, are compared to the aerosol optical depths derived from concurrent MODIS observations on 25, 26, and 27 August in Figure 5.44 to Figure 5.46. The figures also show the corresponding scatter plots for the entire maps and specific rectangles defined covering just the Greek fire plumes. On 25 and 26 August, the simulations and observations of the Greek fire plumes display very similar shapes, as discussed above. On 25 August, the simulated plume is much broader. This could indicate that even the operational resolution of the ECMWF model is insufficient to accurately capture the plume dispersion on such scales. Furthermore, a tendency of the model to overestimate the AOD is apparent. We estimate that this is a consequence of applying the Ichoku and Kaufman (2005) emission factors, which are reportedly too high.

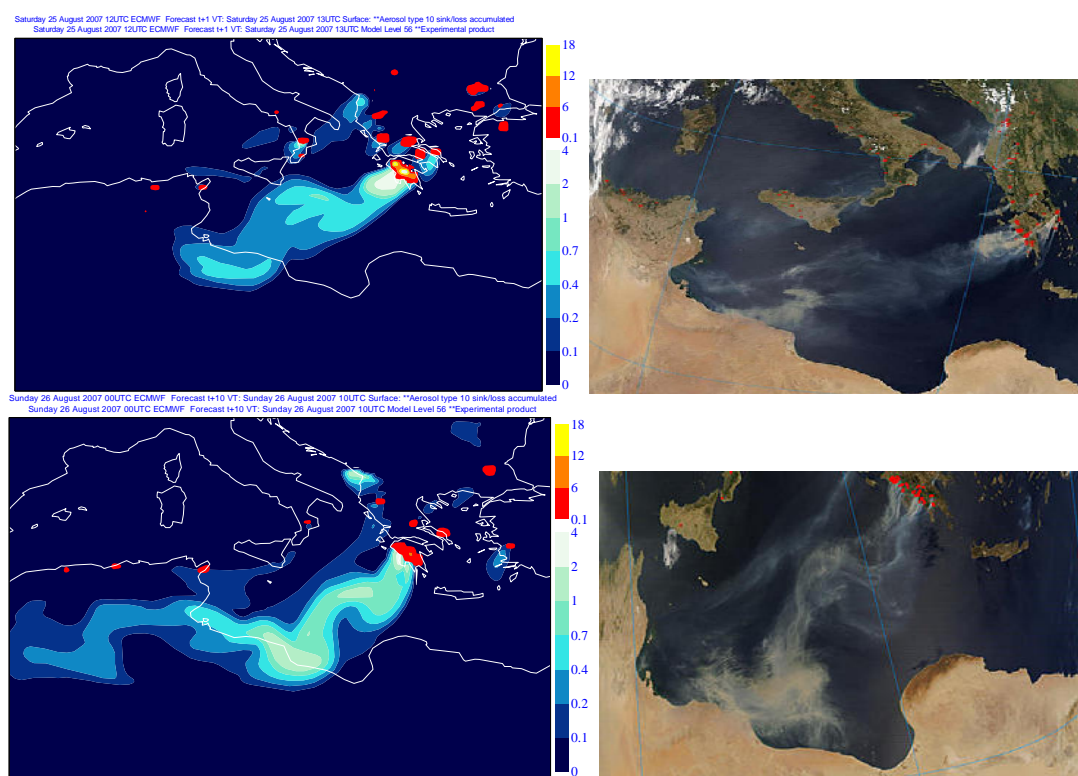


**Figure 5.43:** Modelled organic matter plus black carbon AOD [-] (left, blue) and MODIS visual images (right) for an Aqua overpass on 25 August, 1205UTC, (top) and a Terra overpass on 26 August, 0935UTC (bottom). Overlaid with SEVIRI FRP [W/m<sup>2</sup>] interpolated to model resolution (left, orange) and MODIS hot spots in (right, red).

The AOD comparison of 26 August confirms these findings: The plume shapes are reproduced well, but the plume AOD values are mostly overestimated. Additionally, the background, which originates from different sources, is underestimated. This might be due to cloud cover effects, which are not simulated.

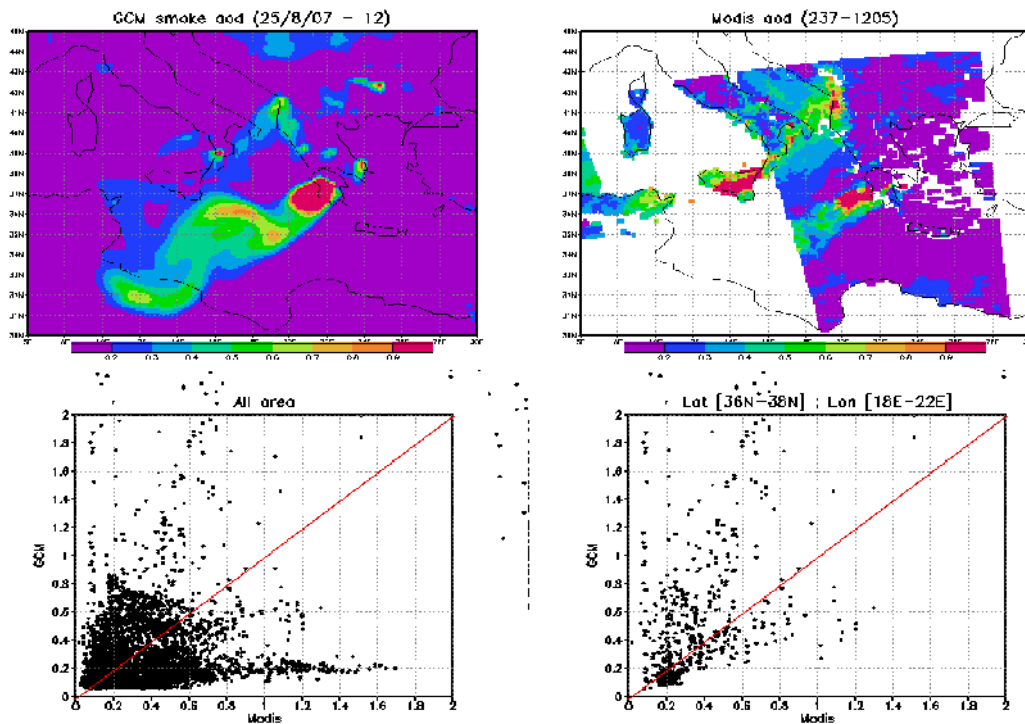


**Figure 5.44:** Modelled smoke AOD [-] (left) and observed MODIS AOD [-] product (right) for Aqua overpasses on 25 August, 1205UTC (top). AOD scatter plots for the entire area and a box on the fire Greek plume (bottom).

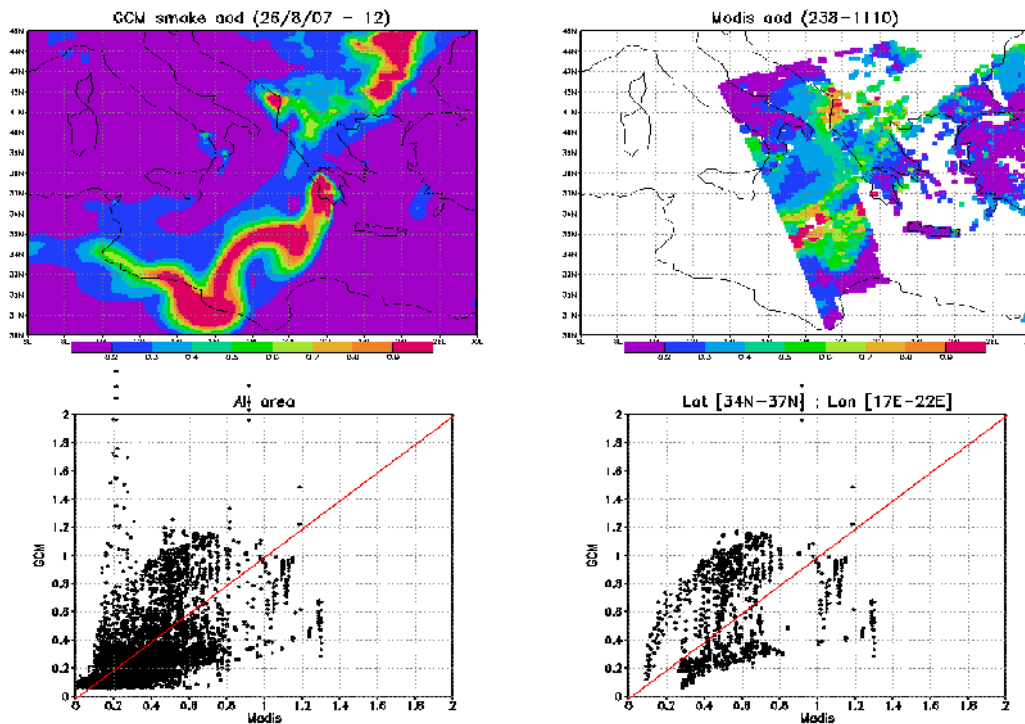


**Figure 5.45:** Modelled smoke AOD [-] (left) and observed MODIS AOD [-] product (right) for Aqua overpasses on 26 August, 1110UTC (top). AOD scatter plots for the entire area and a box on the fire Greek plume (bottom).

On 27 August, the Peloponnese was partly covered by clouds, the effects of which have been neglected in the tested SEVIRI FRP product generation. Obviously, the shortcoming translates into a marked degeneration of the quality of the simulated aerosol field: The westward outflow from the Peloponnese is overestimated and the southward outflow in the simulation has not been detected by the observations at all.



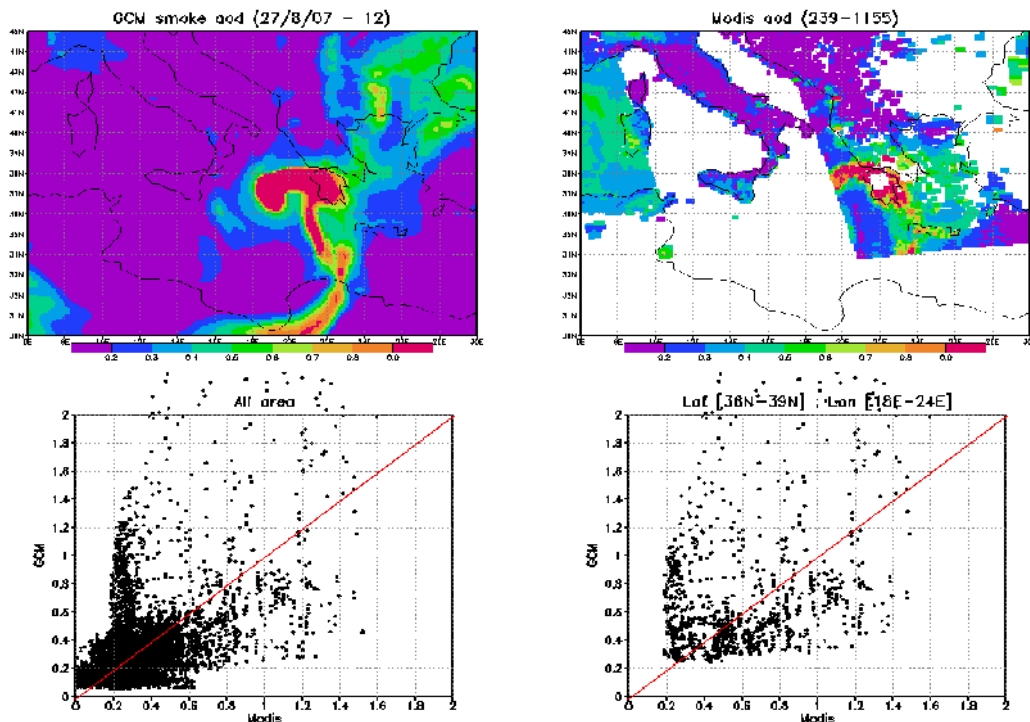


**Figure 5.46:** Modelled smoke AOD [-] (left) and observed MODIS AOD [-] product (right) for Aqua overpasses on 27 August, 1155UTC (top). AOD scatter plots for the entire area and a box on the fire Greek plume (bottom).

Starting on 26 August, SEVIRI detected large fires along the Algerian coast. The resulting smoke plumes, travelling north-eastwards, are also evident in our simulation. Figure 5.47 shows an example of the fire activity and the developing smoke plume on 30 August. The AERONET station at Lecce University in Southern Italy observed an aerosol plume passing through on 30-31 August, see Figure 5.48. It is confirmed by MODIS observations. The fact that the steep rise is predominantly in the recorded fine mode AOD indicates that the aerosols may originate from fires. The simulation exhibits a mixed dust and smoke plume passing over Lecce on 30 August. The steepest rise in AOD is attributed to a rise of the smoke aerosol components, which originated from the Algerian fires. The dust component clearly has a smoother time evolution. This is another indication that the observed strong plume is dominated by smoke emitted in Algeria and transported across the Mediterranean.



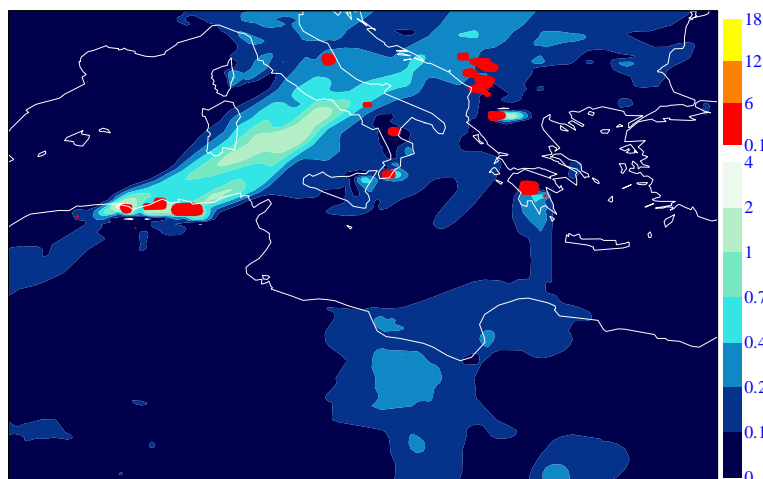



**Figure 5.47:** Modelled organic matter plus black carbon AOD [-] (bluish) on 30 August 2007, 1430UTC, overlaid with observed SEVIRI FRP [W/m2] interpolated to model resolution (reddish). The University of Lecce AERONET station is indicated by a white circle.

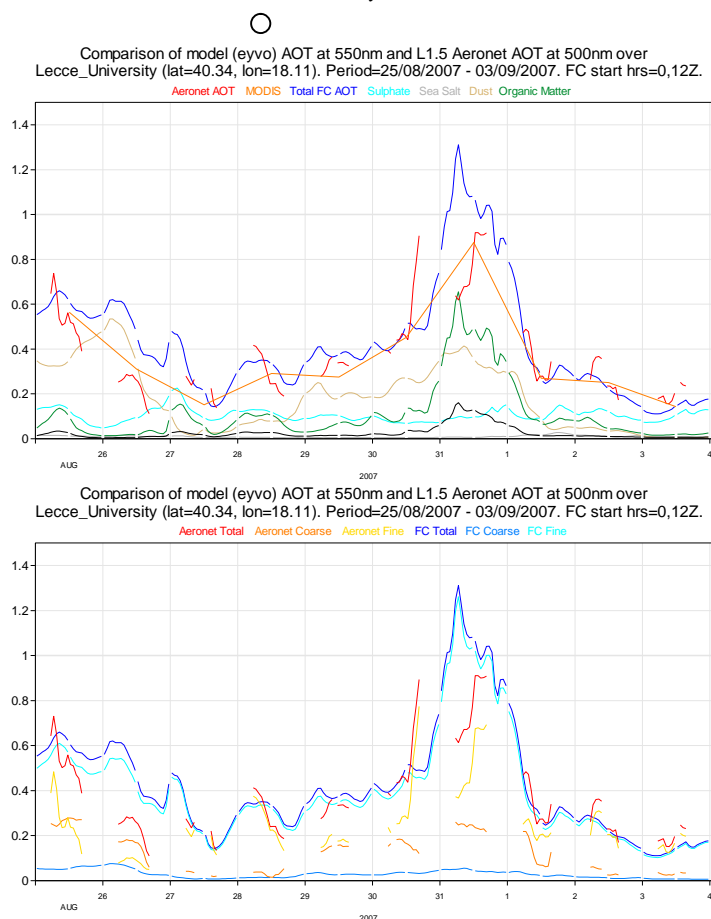


**Figure 5.48:** Observed and modelled AOD time series over Lecce, Southern Italy. Observations by MODIS (top orange: daily average AOD) and AERONET (red: AOD, bottom orange: coarse mode AOD, yellow: fine mode AOD). Modelled AOD (dark blue) and AOD contributions by the aerosol model species (top) and modes (bottom). The mode definition of AERONET and the model are, unfortunately not identical. [graphics by L. Jones, ECMWF. MODIS data from

	Land SAF VR-FRP	Doc: SAF/LAND/IM/VR_FRP/V_09 Issue: Version V/2009 Date: 18/10/2009
---	-----------------	---

[http://gcmd.nasa.gov/records/GES\\_DAAC\\_MOVAS.html](http://gcmd.nasa.gov/records/GES_DAAC_MOVAS.html), AERONET data from <http://aeronet.gsfc.nasa.gov/>

As a conclusion, this end-to-end study shows that retrospective aerosol fire plume modelling with the GEMS aerosol model driven by SEVIRI fire emission input works well. More comprehensive validation is needed, but

- High temporal resolution seems vital in order to reproduce the observed smoke plume structures.
- Model runs based on SEVIRI FRP data reproduce horizontal structures found in the observations.
- Emission factors found in the literature vary by a factor of five at least. An intermediate value would be most appropriate for the Greek fire case.
- Exact plume positions and absolute scaling may still be improved. This will require
  - the best possible correction for cloud cover
  - better modelling of injection heights
  - better knowledge of emission factors.

Several distinct Greek fire plumes have been simulated. They have travelled more than 1000 km in 1-2 days. Algerian fire plumes, mixed with Saharan dust, have also been simulated. They have travel to Italy, where they were apparently identified by ground-based observations.

In light of the potential use of the SEVIRI FRP data for smoke plume forecasts it can be concluded that forecasting of the transport and evolution of the fire plume is possible for 1-2 days into the future if the SEVIRI data are made available within a few hours after observation. Since the study was performed at a horizontal resolution typical for a regional air quality model, forecasts of smoke plumes in Southern Europe similar to the shown examples can be expected from the future regional air quality systems in GEMS when the SEVIRI FRP product becomes available. The global GEMS modelling system will be able to produce routine smoke and air pollution plume forecasts for Europe and Africa at a coarser resolution of ~125 km. This resolution will be further enhanced in the coming years.

## 5.5. Analysis of Error Budget in LSA SAF FRP Pixel Product

The LSA SAF pixel-level FRP product contains an estimate of the per-pixel uncertainty in FRP [Govaerts et al., 2008], which has four components [uncertainty derived from the FRP coefficient, uncertainty derived from the atmospheric transmissivity calculation, uncertainty derived from the radiance observation of the fire pixel, and uncertainty derived from the variability in the background window signal. These sources of uncertainty are described in the algorithm ATBD and combined in quadrature to provide the total uncertainty estimate at the per pixel level.

For the North African LSA SAF region 1 – 8 December 2008, Figure 5.49 provides the frequency distribution of the various uncertainty components, along with the total uncertainty estimate. In general, the smaller the fire pixel FRP the larger the fractional uncertainty, since for example a fixed radiance variation in the background window and a fixed uncertainty in the measure of the fire pixel radiance will have relatively more effect. Since there are typically many more low FRP fire pixels than high FRP fire pixels, the frequency distribution indicates that there are high numbers of fire pixels with uncertainties around  $\pm 50\%$  or more.

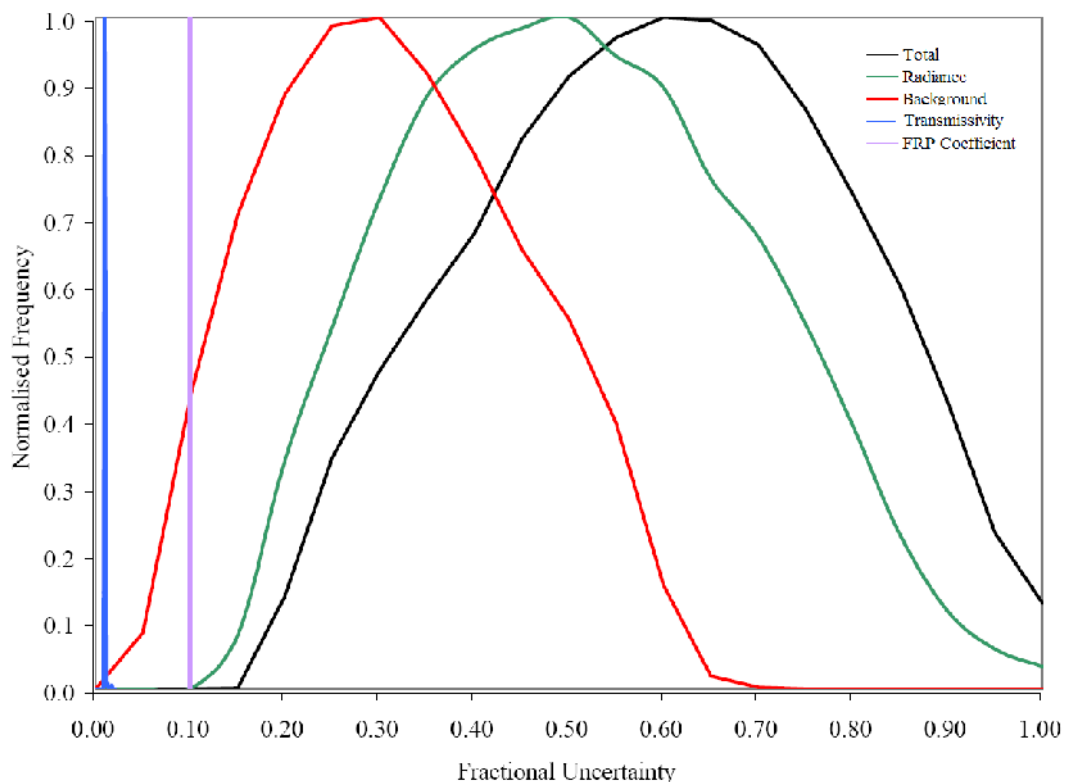


**Figure 5.49:** Frequency distribution of FRP uncertainty contributions for all fire pixels identified in the North African LSA SAF region, 1-8 December 2009.

Figure 5.50 shows how for the same region, the individual uncertainty contributions vary over the period of the fire diurnal cycle. In general the per-pixel uncertainties are somewhat lower at night due to the temporal variation in the radiance noise and background window uncertainty contributions. These variations for the North African LSA SAF region are indicative of these experienced over the other three LSA SAF areas.

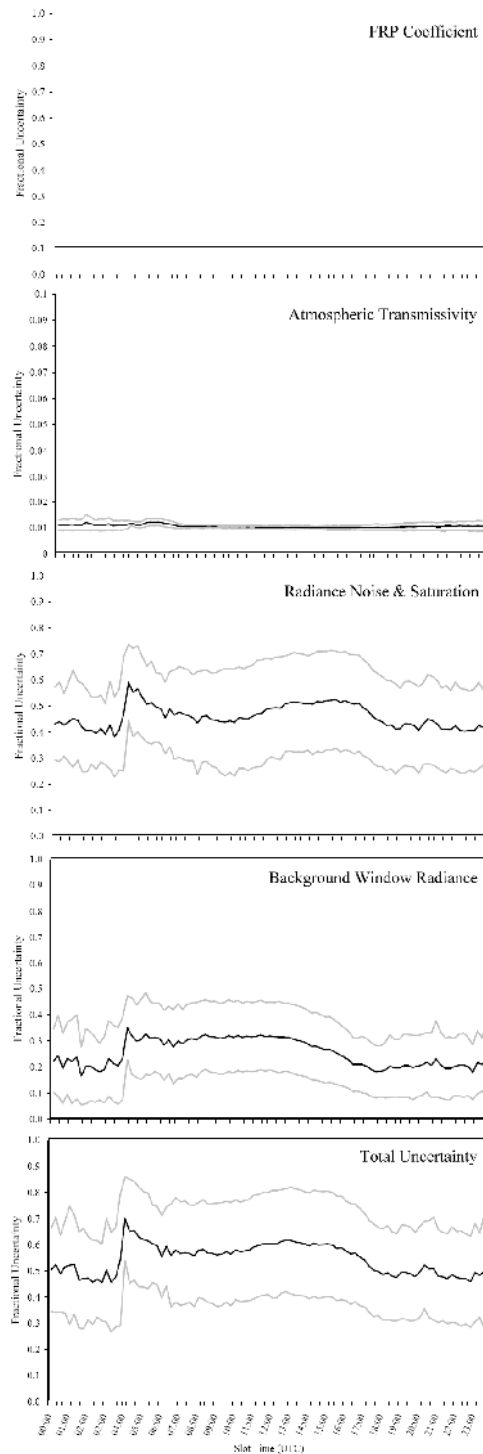


**Figure 5.50:** Temporal variation of the mean and mean  $\pm$  standard deviation of the four individual components of the error budget discussed in Section 3.7 of the product ATBD are shown, along with the total. Note the different y-axis scale of the error budget related to the atmospheric transmissivity component. These data were collected over the North African LSA SAF region 1-8 December 2008.

## 6. CONCLUSIONS


### 6.1 Product Validation Summary

Within the FREEVAL project, the SEVIRI FRP product has been evaluated with respect to

- the validity of assumptions made in the algorithm derivation;
- the capability of the SEVIRI instrument to reliably detect fires and quantify FRP;
- the influence of SEVIRI data processing on the FRP product;
- the impact of using it in potential operational applications.

The theoretical and radiative transfer modelling analysis of the algorithm performance has shown that the MIR radiance method algorithm used within the SEVIRI FRP products has an underlying accuracy of  $\pm 12\%$  over the temperature range expected for active fires, and that the assumptions made when implementing this algorithm on data of highly-sub pixel sized fires (as will be the case with coarse spatial resolution satellite data such as that from SEVIRI) in theory introduce negligible other errors. In this case, if the fire pixels that comprise an individual fire can be reliably detected, show a sufficiently large MIR radiance increase above the background, and if the MIR atmospheric transmission is reliably known then the FRP can be quantified to this level of uncertainty. Differences between the original KCL algorithm and the Land SAF implementation are negligible in this respect.

In practical terms, the most limiting factor for product accuracy appears to be the current coarse pixel size, of area  $\sim 23 \text{ km}^2$  at the sub-satellite point, increasing to  $\sim 90 \text{ km}^2$  near the disk edge (assuming full width at half maximum sensitivity values). Numerous fire pixels with FRP values less than 40 MW escape detection by SEVIRI, and the detection and quantification of slightly larger fires (40-100 MW) will be less reliable, because the enhancement of the MIR brightness temperature due to the fire with respect to the (somewhat variable) background temperature of surrounding pixels is rather small. To some extent the impacts of the coarse spatial resolution are balanced by the extremely high temporal resolution of the geostationary observations. As was shown for fires in the Central African Republic, over the course of a day SEVIRI will capture a signal from most fire events that the much higher spatial resolution MODIS instruments on EOS Aqua and Terra can detect during their four-times per day overpasses. We assume that this is related to the ability of SEVIRI to observe the complete fire life cycle and thus capture fires when they reach their peak intensity. However, for any particular SEVIRI observation, the cumulative FRP measured at the regional (e.g. grid cell or country-scale) is likely to be an underestimate of what would have been measured by MODIS had it observed the whole area at the same moment, by on average around 50%.

	Land SAF VR-FRP	Doc: SAF/LAND/IM/VR_FRP/V_09 Issue: Version V/2009 Date: 18/10/2009
---	-----------------	---


Due to the higher spatial resolution observations and wide usage of the MODIS active fire products these are taken to be the reference standard against which the SEVIRI FRP product is assessed. Comparisons were performed for the period February 2004 to January 2005 and included data from the most recent implementation of the LSA SAF FRP product based on radiances collected with Meteosat 9 in 2008. Tests were made on a per-fire basis, as well as on a regionally gridded basis. When MODIS and SEVIRI detect the same fire, in 76 % of the cases the FRP retrieved by SEVIRI is within 33 % of that reported by MODIS. Errors of omission and commission are estimated to 54% (68% for the one month of data of the Land SAF product) and 8% (2%), respectively, varying with season. Fire detection has been found to be largely independent of the dominant vegetation type in which the fire occurs, although SEVIRI shows a small tendency to detect fewest of the MODIS-detected fires in croplands (a landcover type dominated by smaller fires), and more of them in forested areas. Performance of the LSA SAF product was comparable to that of the KCL implementation – for example in the North African LSA SAF region per-fire FRP measures from the LSA SAF FRP product were within 20% of the values obtained from MODIS 53% of the time.

Since the MIR channel on SEVIRI was not designed for fire detection but rather for land surface monitoring, it saturates around 335 K, a temperature that is easily exceeded by larger fire events. The effect of this saturation is an underestimation of FRP for large fires, which can in fact contribute significantly to an underestimation of FRP in a given region. Limited experiments have indicated an FRP underestimation of ~ 10% by day due to pixel saturation and up to 40% at night, though at night there are many fewer fires and much lower regional FRP totals, so saturation of a few night-time pixels can induce large percentage errors. A change of the MIR SEVIRI band gain corresponding to a saturation temperature of 375K would remove this effect.

The spatial filtering and geometric interpolation performed on-board MSG as part of the level 1 to level 1.5 processing induces some additional noise in the MIR field, which further reduces the instrument's ability to detect all the fire pixels associated with an individual fire event, and to accurately quantify their FRP. The “blurring” of fire radiances related to this pre-processing can reduce level 1.5 fire pixel MIR temperatures, and as a consequence fewer pixels appear to be saturated in the level 1.5 data than were originally saturated at the instrument (level 1.0) stage. However, it is shown through theoretical modelling and targeted data analysis that the effects of the level 1 to level 1.5 processing are generally outweighed by the limitations given by the sensor resolution and the pixel saturation effects.

## **6.2. Demonstrated Usefulness of Product**

FREEVAL has undertaken two types of activity in order to assess the potential use of the SEVIRI FRP product in (predominantly) operational applications:

	Land SAF VR-FRP	Doc: SAF/LAND/IM/VR_FRP/V_09 Issue: Version V/2009 Date: 18/10/2009
---	-----------------	---

- Several potential users were contacted and queried about their requirements and willingness to use an FRP product from SEVIRI and
- a number of impact studies were performed in the context of pre-operational modelling systems for monitoring of atmospheric composition.

Several users provided a strong recommendation for operational generation of FRP from the SEVIRI sensor. Although SEVIRI performs less well than for example MODIS with respect to the detection and quantification of fires on a per-observational basis, its high temporal sampling frequency and the expected availability of near real-time data products offers great potential to improve the prediction of smoke plumes from fire events in Southern Europe and Africa, and this has been demonstrated in the case studies described in this report. These case studies also underline the readiness of the community to make use of the product very soon after its release. Furthermore, the 15-minute sampling frequency will also be of interest for operational warning services, such as that operated by the South African power company ESCOM (see section 1.2).

### 6.3 Definition of Accuracy Requirements



The user requirements for FRP products in general were collected in Table 6.1 in section 0 of this report. Here, we assess the accuracy requirements specifically for the SEVIRI FRP product and in light of the theoretical performance that is achievable with this sensor under its standard operating conditions.

The three accuracy values tabulated below are defined as follows:

- *Threshold accuracy*: this is the accuracy limit which is needed so that the product fulfils its purpose.
- *Target accuracy*: this is the average product accuracy under the present operating conditions and with the instrument characteristics of SEVIRI. With this product quality the product will be valuable for most of the users identified above.
- *Optimal accuracy*: this is the accuracy that can be reached under optimum conditions (sub-satellite point, cloud-free scene, homogeneous background, medium sized fire).

As was demonstrated in the product validation activities, the accuracy of the SEVIRI FRP product will depend on various factors related to pixel resolution, saturation, viewing geometry and on-board and ground-based pre-processing of raw signals. Furthermore, the required level of accuracy will depend on the application, and different aspects of accuracy might be emphasized in different applications. For example, a fire warning system will be less concerned about the absolute quantitative value of FRP as long as the fire can be reliably detected rapidly (with few commission errors in particular) and there is some indication about fire severity. Chemical forecasts, and even more so reanalysis simulations, on the other hand, depend on the reliability of area-averaged fire emissions (and thus FRP) and have less concern about the ability of the instrument to capture each and every fire.





 	Land SAF VR-FRP	Doc: SAF/LAND/IM/VR_FRP/V_09 Issue: Version V/2009 Date: 18/10/2009
---	-----------------	---

**Table 6.1:** *Summary of accuracy requirements for the SEVIRI FRP pixel and gridded products*

	Pixel product	Gridded product
Threshold accuracy	N.A. <sup>1</sup>	Factor 3 over continental area
Target accuracy	70% of retrieved FRP within 50% of “true” values as defined by MODIS on a per-fire basis	Factor 2 at the scale of ecozones
Optimal accuracy	70% of retrieved FRP within 20% of “true” values as defined by MODIS on a per-fire basis	25% on a 5° grid

<sup>1</sup> successful detection of a significant fraction of fires reproducing the spatial and temporal distribution can be considered the threshold target

In summary it can be said that the SEVIRI FRP product fulfils the accuracy requirements given in the table above. It will greatly improve the ability of operational atmospheric models to monitor emissions from highly variable vegetation fires and the smoke plumes emanating from them.

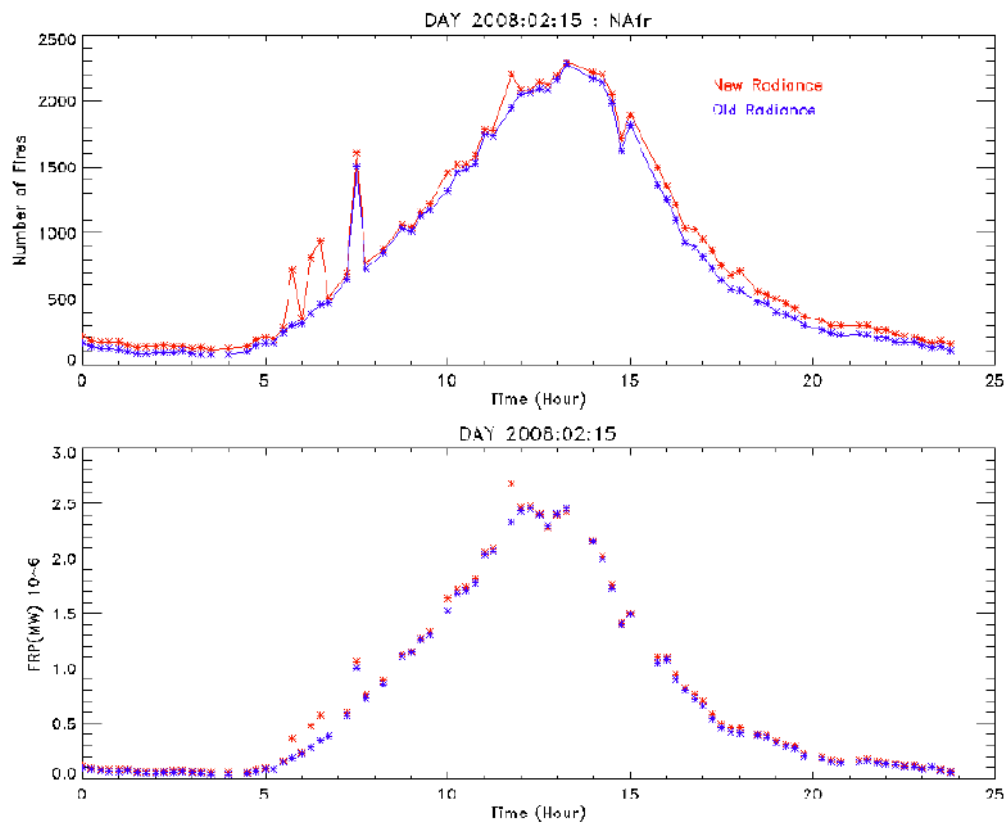
 	Land SAF VR-FRP	Doc: SAF/LAND/IM/VR_FRP/V_09 Issue: Version V/2009 Date: 18/10/2009
---	-----------------	---

## Appendix 1 – Impact of EUMETSAT Radiance Definition Change



This Appendix presents the results of the comparison of one day of Fire Radiative Power products generated in the re-processing facility of the LSA SAF (IM, Lisbon) using as input Level 1.5 radiances estimated in the old scheme defined in terms of spectral blackbody radiance (i.e. at a defined wavelength) and new one defined in terms of effective blackbody radiance (i.e. representing the integral over the spectral band). This change in the Image Processing Facility (IMPF) is described in EUM/STG-OPSWG/21/07/07/DOC/04. This exercise has been performed to estimate the impact of this change in the generation of FRPs from SEVIRI (radiometer on board Meteosat Second Generation satellites) Level 1.5 images. The data used were from the North African LSA SAF region, 15 Feb 2008.

The pre-operational version of the FRP\_PIXEL algorithm has been integrated in the re-processing facility at the LSA SAF and has been fed with both input radiances in order to generate two datasets for comparison.

Results are shown in Figure A, and because of missing inputs both datasets are affected by gaps and corruptions in the generated FRPs. A manual post-processing was necessary to screen out all the not correct FRPs. The number of fires detected with the new scheme is always higher. This is not surprising as the formulation of the thresholds used in the algorithm has been done thinking to be in the new scheme. The daily cycle for both Number of detected fires and FRP is plotted in the Figure A. The plot includes some values retrieved from corrupted data, and in particular the “bumps” are due to incomplete input data, in particular to not complete Cloud Mask files. Away from these times, the difference induced by the radiance definition scheme change can be seen to be rather low, and during the day where most fires are present is limited to a few percent.



**Figure A:** Daily Cycle for Number of fires (top) and FRP (bottom). Old radiance output in blue, new one in red for the North African LSA SAF region, 15<sup>th</sup> February 2008.

 	Land SAF VR-FRP	Doc: SAF/LAND/IM/VR_FRP/V_09 Issue: Version V/2009 Date: 18/10/2009
---	-----------------	---

## Acknowledgments

This validation report is based on the final report of the study on “Evaluation of a Fire Radiative Power Product derived from Meteosat 8/9 and Identification of Operational User Needs” which has been performed by the FREEVAL consortium under EUMETSAT contract EUM/CO/06/4600000277/YG. The FREEVAL consortium was composed of:

### Project team:

Martin G. Schultz, FZ Jülich, Germany (coordinator)  
Martin Wooster, King’s College, London, UK (co-coordinator)


Olivier Boucher, Met. Office, Exeter, UK  
Marie Doutriaux-Boucher, Met Office, Exeter, UK  
Claire Granier, University Paris, France  
Angelika Heil, FZ Jülich, Germany  
Anthony Hollingsworth<sup>†</sup>, ECMWF, Reading, UK  
Johannes W. Kaiser, ECMWF, Reading, UK  
Thomas Kasikowski, Met Office, Exeter, UK  
Jean-Jacques Morcrette, ECMWF, Reading, UK  
Gareth Roberts, King’s College, London, UK  
Adrian Simmons, ECMWF, Reading, UK  
Guido van der Werf, Vrije Universiteit, Amsterdam, The Netherlands

External contributions from Mikhail Sofiev, FMI are highly appreciated.

A special thank goes to EUMETSAT/OPS team for their contribution in the SEVIRI special acquisition mode.



---

<sup>†</sup> Dr. Anthony Hollingsworth sadly passed away on 29 July 2007.



	Land SAF VR-FRP	Doc: SAF/LAND/IM/VR_FRP/V_09 Issue: Version V/2009 Date: 18/10/2009
---	-----------------	---

## References

- Arino, O., J.-M. Rosaz, and P. Goloub (1999) The ATSR World Fire Atlas. A synergy with 'Polder' aerosol products. *Earth Observation Quarterly*, 1-6.
- Dennison, P.E., K. Charoensiri, D.A. Roberts, S.H. Peterson, and R.O. Green (2006) Wildfire temperature and land cover modeling using hyperspectral data. *Remote Sensing of Environment*, 100, 212-222
- Dozier, J. (1981) A method for satellite identification of surface temperature fields of sub-pixel resolution, *Remote Sens. Environ.*, 11, 221-229.
- EUMETSAT (2003) Image Processing Facility Detailed Design Specification – Vol Q Algorithms, EUMETSAT EUM/MSG/SPE/198-Q, 307pp.
- Flasse, S. (2004). Study on SEVIRI Operational Fire Products, Final report to EUMETSAT contract EUM/CO/03/1181/YG.
- Giglio, L., and J. D. Kendall (2001) Application of the Dozier retrieval to wildfire characterisation: A sensitivity analysis, *Remote Sens. Environ.*, 77, 34- 49.
- Giglio, L., G. R. van der Werf, J. T. Randerson, G. J. Collatz, and P. Kasibhatla (2006), Global estimation of burned area using MODIS active fire observations, *Atmospheric Chemistry and Physics*, 6, 957-974.
- Giglio, L., J. Descloitres, C.O. Justice, and Y. Kaufman (2003a) An enhanced contextual fire detection algorithm for MODIS. *Remote Sensing of Environment*, 87, 273-282.
- Giglio, L., Kendall, J. D., and Mack, R. (2003b) A multi-year active fire dataset for the tropics derived from TRMM VIRS. *International Journal of Remote Sensing*. 24. 22. 4505-4525.
- Govaerts, Y., Wooster, M.J., Lattanzio, A. and Roberts. G. (2007), Fire Radiative Power (FRP) characterisation Algorithm Theoretical Basis Document, EUMETSAT, EUM/MET/SPE/06/0398
- Hollingsworth, a., R.J. Engelen, C. Textor, A. Benedetti, O. Boucher, F. Chevallier, A. Dethof, H. Elbern, H. Eskes, J. Flemming, C. Granier, J.W. Kaiser, J.J. Morcrette, P. Rayner, V.-H. Peuch, L. Rouil, M.G. Schultz, A.J. Simmons (2008) The Global Earth-system Monitoring using Satellite and in-situ (GEMS) Projects: Towards a monitoring and forecasting system for atmospheric composition, *BAMS*, in press
- Ichoku C. & Y.J. Kaufman (2005) A method to derive smoke emission rates from MODIS fire radiative energy measurements, *IEEE Transactions on Geoscience and Remote Sensing*, 43(11), 2636 - 2649
- Justice, C. O., L. Giglio, S. Korontzi, J. Owens, J. Morisette, D. Roy, D., J. Descloitres, S. Alleaume, F. Petitcolin, and Y. Kaufman (2002) The MODIS fire products, *Remote Sensing of Environment*, 83, 244-262.
- Kaiser, J.W., M.G. Schultz, J.-M. Gregoire, C. Textor, M. Sofiev, E. Bartholome, M. Leroy, R.J. Engelen, A. Hollingsworth (2006) Observation Requirements for Global Biomass Burning Emission Monitoring, *Proc. 2006 EUMETSAT Met. Sat. Conf.*
- Kaufman, Y. J., C. Justice, L. Flynn, J. Kandall, E. Prins, D. E. Ward, P. Menzel, and A. Setzer (1998) Monitoring global fires from EOSMODIS, *J. Geophys. Res.*, 103, 32,215-32,239.
- Lattanzio, A. (2006) Evaluation Report on the Prototyping of the Fire Thermal Anomalies Algorithm. Report EUM/MET/REP/07/0006, EUMETSAT.

 	Land SAF VR-FRP	Doc: SAF/LAND/IM/VR_FRP/V_09 Issue: Version V/2009 Date: 18/10/2009
---	-----------------	---

- Lattanzio, A. and Govaerts, Y. (2006) Report on the comparison of the fire thermal anomaly products generated with Meteosat-8 and Meteosat-9 data, EUMETSAT EUM/MET/REP/06/0483, 11pp.
- Langaas, S. (1995) A critical review of sub-resolution fire detection techniques and principles using thermal satellite data. PhD thesis, Department of Geography, University of Oslo, Norway.
- Lutz, H-J., Gustafsson, J. B. and Valenzuela-Leyenda, R. (2003) Scenes and cloud analysis from Meteosat Second Generation (MSG). Proceedings of the 2003 EUMETSAT Meteorological Satellite Conference. Weimar. Germany. EUMETSAT. EUM P39. 311-318.
- Moran, P.A.P. (1950), Notes on continuous stochastic phenomena. *Biometrika* 37:17-23.
- Morcrette, J.-J., L. Jones, J.W. Kaiser, A. Benedetti, O. Boucher, Toward a forecast of aerosols wit the ECMWF Integrated Forecast System (2008) ECMWF Newsletter No. 114, ECMWF, Reading, UK.
- Morisette, J. Giglio, L., Csiszar, I. and Justice, C. (2005) Validation of the MODIS active fire product over Southern Africa with ASTER data, *International Journal of Remote Sensing*, 26, 4239-4264.
- Ohlemiller, T.J. (1995) Smoldering combustion. In: Quincy, MA, DiNenno, P. J.; Beyler, C. L.; Custer, R. L. P.; Walton, W. D. (Eds.), *SFPE Handbook of Fire Protection Engineering*, 2nd edition, vol. 2, Building and Fire Research Laboratory (NIST), Gaithersburg, MD, pp.171-179.
- Pereira J. and Y.M. Govaerts, (2001), EUMETSAT PDD Technical Memorandum No. 7
- Riggan, P., Tissell, R., Lockwood, R., Brass, J., Pereira, J., Miranda, H., Campos, T., Higgins, R. (2004) Remote measurement of energy and carbon flux from wildfires in Brazil. *Ecological Applications*, 14, 855-872.
- Roberts, G.J. and Wooster, M.J (2008) Fire Detection and Fire Characterization Over Africa Using Meteosat SEVIRI, *IEEE Trans on Geosci. and Remote Sens.*, 46, doi: 10.1109/TGRS.2008.915751
- Roberts, G., M. J. Wooster, G. L. W. Perry, N. Drake, L.-M. Rebelo, and F. Dipotso (2005) Retrieval of biomass combustion rates and totals from fire radiative power observations: Application to southern Africa using geostationary SEVIRI imagery, *J. Geophys. Res.*, 110, D21111, doi:10.1029/2005JD006018.
- Robinson, J. (1991) Fire from space: Global fire evaluation using infrared remote sensing, *Int. J. Remote Sens.*, 12, 3 –24.
- Shephard, M. and Kennelly, E. (2003) Effect of Band-to-Band Coregistration on Fire Property Retrievals, *IEEE Trans on Geosci. and Remote Sens.*, 41, 2648-2661.
- Schultz M.G., *et al.* (2008) Evaluation of a Fire Radiative Power product derived from Meteosat-8/9 and identification of operational user needs, Final report to EUMETSAT contract EUM/CO/06/4600000277/YG
- Van der Werf, G. R., J. T. Randerson, G. J. Collatz, L. Giglio, P. S. Kasibhatla, A. Avelino, S. C. Olsen, and E.S. Kasischke (2004) Continental-scale partitioning of fire emissions during the 1997-2001 El Nino / La Nina period. *Science*, 303: 73-76.
- van der Werf, G. R., J. T. Randerson, L. Giglio, G. J. Collatz, P. S. Kasibhatla, and A. F. Arellano (2006) Interannual variability in global biomass burning emissions from 1997 to 2004, *Atmospheric Chemistry and Physics*, 6, 3423-3441.
- Wolfe, R. E., M. Nishihama, A. J. Fleig, J. A. Kuyper, D. P. Roy, J. C. Storey, and F. S. Patt (2002) Achieving sub-pixel geolocation accuracy in support of MODIS land science, *Remote Sens. Environ.*, 83, 31–49.

 	Land SAF VR-FRP	Doc: SAF/LAND/IM/VR_FRP/V_09 Issue: Version V/2009 Date: 18/10/2009
---	-----------------	---

- Wooster, M. J., B. Zhukov, and D. Oertel (2003) Fire radiative energy for quantitative study of biomass burning from the BIRD experimental satellite and comparison to MODIS fire products, *Remote Sens. Environ.*, 86, 83– 107.
- Wooster, M. J., G. Roberts, G. L. W. Perry, and Y. J. Kaufman (2005) Retrieval of biomass combustion rates and totals from fire radiative power observations: FRP derivation and calibration relationships between biomass consumption and fire radiative energy release, *J. Geophys. Res.*, 110, D24311, doi:10.1029/2005JD006318.
- Zhukov, B., Lorenz, E., Oertel, D., Wooster, M. J., and Roberts, G. (2005) Spaceborne detection and characterization of fires during the Bi-spectral Infrared Detection (BIRD) experimental small satellite mission 2001-2004. *Remote Sens. of Environ.*, 100: 29-51.